Lab on a Chip

CRITICAL REVIEW

View Article Online
View Journal | View Issue

Cite this: *Lab Chip*, 2026, **26**, 1739

Engineering organs-on-a-chip *via* multi-channel microfluidics

Ji Qiu,†[a] Jia Yang,†[bc] Lihao Liu,[bc] Jiameng Wen,[bc] Jiachen Yang,[bc] Wenwan Shi,[bc] Xiaoxiang Gao,[bc] Jing Sun,[d] Ling Bai, *[a] Xiaojiang Liu *[bc] and Zhongze Gu *[bc]

Conventional *in vitro* physiological models, relying on animal studies and 2D/3D cell cultures, are fundamentally limited by interspecies biological discrepancies, ethical constraints, or inadequate replication of human physiology. Organ-on-a-chip (OoC) technology overcomes these challenges through emulating organ-specific microphysiological systems. The transformative power of this innovation lies in multi-channel microfluidic chips. These chips facilitate the formation of 3D cellular organizations and tissue interfaces *via* integrated porous membranes, micropillar arrays, or perfusable vascular microchannels, simultaneously allowing for precise and dynamic modulation of chemical, biological, and physical factors. Rapid technological evolution has yielded functional models of lung alveoli, the blood–brain barrier, cardiac tissues, *etc.*, thereby advancing drug testing and disease modeling accuracy. This review systematically examines the development of OoC technology through the lens of multi-channel microfluidics by focusing on four pivotal domains: (1) the biomimetic design overview for OoCs, (2) fabrication methods including soft lithography and 3D printing, (3) applications in pathophysiological investigations, preclinical drug evaluation, and toxicological assessment, and (4) current challenges and perspectives in structural design, materials and fabrication, biological applications, and other development directions. This review is intended to provide a reference for the technological iteration and interdisciplinary application of multi-channel microfluidic chip systems.

Received 17th June 2025,
Accepted 12th December 2025

DOI: 10.1039/d5lc00598a

rsc.li/loc

1. Introduction

In the quest to achieve efficient drug screening, precise diagnosis and treatment, and elucidation of disease mechanisms, the biomedical field has continuously sought the ideal *in vitro* physiological model. Early models relied on animals, which can partially simulate complex physiological environments and disease progression.[1–4] Later, 2D cell cultures emerged as candidates because they are simple, cost-effective, and highly reproducible, and follow standardized protocols. In the 2020s, organoids were developed, offering a closer resemblance to physiological cell composition and behavior and being simpler to manipulate than animal models. However, these models often face challenges in simulating the physiological functions of human organs.[5] For example, animal models are limited by interspecies biological discrepancies, ethical controversies, prolonged experimental timelines, and poor reproducibility, and cannot fully replicate human disease complexity or ensure clinical translatability.[6–9] Conventional 2D cell culture systems are fundamentally limited in their capacity to mimic the 3D extracellular matrix (ECM) architecture and spatiotemporal heterogeneity of native tissues. This structural simplification disrupts cell–ECM interactions and gradient-dependent signaling, thereby failing to recapitulate critical aspects of *in vivo* physiological contexts, such as mechanotransduction and cell–cell communication dynamics.[10] Organoids face critical limitations, including substantial batch-to-batch heterogeneity, incomplete terminal differentiation, and compromised biomimetic fidelity, which collectively constrain their translational scalability.[11]

To overcome these limitations, organ-on-a-chip (OoC) technology was developed (Fig. 1). OoC devices integrate bioengineering and microfluidic technology, and utilize 3D tissue constructs, cell-type-specific co-culture systems, and optimized cell culture protocols to replicate the native tissue cytoarchitecture accurately.[12] Single-channel OoCs or static OoC models, which employ static or simplified flow

[a] *School of Materials Science and Engineering, Jiangsu University, Zhenjiang, 212013, China. E-mail: lingmubai@ujs.edu.cn*
[b] *State Key Laboratory of Digital Medical Engineering, School of Biological Science and Medical Engineering, Southeast University, Nanjing, 211189, China. E-mail: xjliu@seu.edu.cn, gu@seu.edu.cn*
[c] *Institute of Microphysiological Systems, Southeast University, Nanjing, 211189, China*
[d] *Department of Oncology, The First Affiliated Hospital of Nanjing Medical University, Nanjing, 210029, China*
† These authors contributed equally to this work.

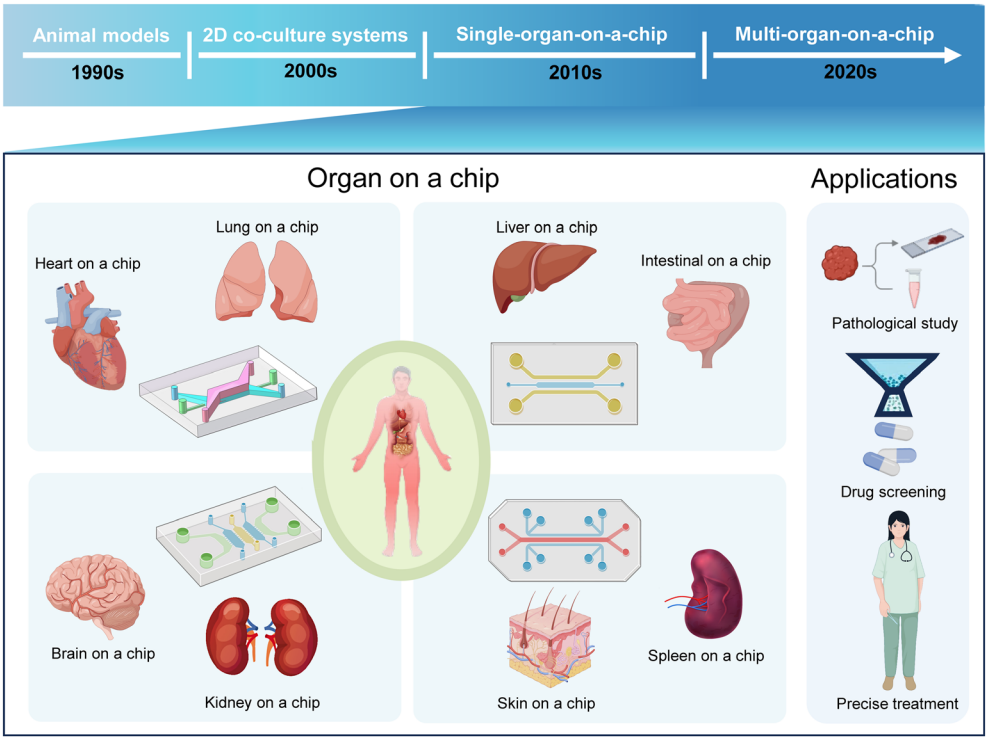

Fig. 1 A scheme showing the evolution of *in vitro* models from animal experiments to OoCs as well as the main types of OoCs, and their applications (created using https://www.biorender.com).

configurations to reproduce organ-level interactions, often fail to recapitulate inter-tissue communication,[13] dynamic concentration gradients,[14] and physiological shear stress-factors[15] essential for maintaining *in vivo*-like functions. These limitations underscore the growing need for multi-channel microfluidic architectures, which enable dynamic fluid exchange and compartmentalized organization, thereby enhancing both physiological fidelity and experimental throughput.[16] Multi-channel microfluidic systems[17] refer to microfluidic architectures that incorporate two or more spatially organized and functionally coupled flow pathways within a single device, enabling controlled inter-compartmental communication, directional transport, and physiological microenvironmental regulation, which have emerged as the core component for fabricating OoCs[18,19] (Table 1). Depending on the design topology, such systems can be partitioned by porous membranes to model epithelial or endothelial barriers,[20] arranged in parallel to allow co-culture or dual-medium perfusion,[21] connected in series to simulate inter-organ circulation,[22] configured as gradient-based channels to generate concentration or shear gradients,[14] or constructed as open or half-open configurations for gas exchange and sampling.[23] These designs provide dynamic control over physical, chemical, and biological parameters, thereby reproducing organ-specific micro-environments and enabling multi-scale physiological interactions.[24] Compared with traditional single-channel or static configurations,[25,26] multi-channel microfluidic architectures provide several unique advantages that significantly enhance both physiological fidelity and experimental throughput.[19,27] By allowing simultaneous yet independently regulated perfusion across interconnected compartments, multi-channel systems can better replicate inter-organ biochemical communication, spatial concentration gradients, and mechanical micro-environments.[22,28] This spatially distributed but dynamically linked flow design enables the recreation of systemic responses such as drug absorption–metabolism coupling[29] and immune-inflammatory crosstalk.[30] Furthermore, multi-channel setups support parallelization and multiplexed assays, facilitating high-throughput drug screening and reproducible modeling of disease progression under physiologically relevant conditions.[31,32]

In 2010, the classic lung-on-a-chip with multi-channel microfluidic systems was developed by Harvard University's Ingber team.[20] Later, various multi-channel single-OoCs were developed, including liver-on-a-chip,[33–35] heart-on-a-chip,[36–38] kidney-on-a-chip,[39,40] and intestinal-on-a-chip.[41,42] Building on the success of single-OoCs, multi-OoCs began to be applied in 2020 to study drug metabolism and pharmacokinetics behavior, as well as complex inter-organ interactions.[28,31,43] Typical multi-OoCs integrate micro-vascular networks, facilitate immune cell trafficking, and enable real-time gas exchange monitoring, thereby enhancing physiological fidelity.[44] For example, the integrated gut–liver-on-a-chip[45] has uncovered a dual immune-metabolic regulatory mechanism through its circulatory channel design; the integrated pancreas–liver-on-a-chip[46] restores hepatic functionality through insulin secretion from pancreatic islets

Table 1 Comparison of single-channel & multi-channel microfluidic designs

Aspect	Single-channel design	Multi-channel design	Potential solutions	Ref.
Physiological fidelity	**Limitation**: lacks shear stress, uniform microenvironment, limited tissue–tissue interactions	**Advantage**: enables controlled shear, dynamic transport, and multicompartment signaling **Limitation**: shear overshoot, unstable gradients	Implement tunable micro-pump/valve systems, microvortex stabilizers, and gradient generators to maintain physiological shear and stable solute profiles	59
Structural complexity	**Advantage**: simple geometry, high reproducibility **Limitation**: cannot reproduce multilayer or barrier interfaces	**Advantage**: multilayer assembly enables barriers, co-culture interfaces **Limitation**: requires precise alignment and bonding	Develop self-aligned interlocking layers, click-fit modules, or magnetic docking systems to simplify multilayer registration	49
Experimental throughput	**Limitation**: typically single-conditions, low parallelization	**Advantage**: enables parallel channels and multiplexed assays **Limitation**: fluidic crosstalk and device-to-device variability	Incorporate on-chip flow resistors, distributed manifolds, and automated high-throughput perfusion controllers	60
Fabrication difficulty	**Advantage**: single-layer fabrication, compatible with soft lithography **Limitation**: limited 3D features	**Advantage**: high-precision 3D architecture **Limitation**: multilayer fabrication is time- and labor-intensive	Apply hybrid lithography–3D printing, laser microfabrication, and rapid thermoplastic molding to reduce fabrication steps while maintaining precision	61
Material compatibility	**Limitation**: PDMS-dominant; prone to adsorption	**Advantage**: flexible material selection (PMMA, COC, PC, hydrogels) **Limitation**: heterogeneous interfaces cause bonding and swelling issues	Use nanocoatings, ALD thin films, parylene deposition, or composite PDMS–glass/COC laminates to improve chemical inertness and interfacial robustness	26, 62
Biological application	**Limitation**: static or monoculture models	**Advantage**: supports co-culture, mechanical stimulation, and dynamic exposure **Limitation**: complex monitoring and unstable long-term perfusion	Integrate optical/electrochemical sensors, real-time TEER modules, and closed-loop flow control for continuous monitoring of multicellular systems	63

under hyperglycemic conditions; the integrated adipose–liver-on-a-chip[47] simulates nonalcoholic fatty liver disease (NAFLD) progression through adipocyte-mediated insulin resistance and cytokine signaling *via* a gravity-driven recirculating medium.

In OoC technology, the multi-channel microfluidics has witnessed remarkable progress in various aspects, including cell culture, manufacturing, characterization, and applications. First, advancements in cell culture technology have enabled the cultivation of diverse cell types, including primary cells, cell lines, stem cells, and organoids, facilitating the modeling of tissue and organ functions in a controlled microfluidic environment.[15] Second, a range of fabrication technologies have been utilized for the development of OoCs, including soft lithography and 3D printing.[48] Third, multi-channel microfluidics has revolutionized microenvironment simulation by dynamically replicating chemical, biological, and physical factors.[49] Among them, different microstructures in the flow channel have been studied to modulate the microenvironment, including porous membranes, micropillar arrays, and perfusable vascular microchannels. Porous membranes[20] separate cell layers and regulate molecular diffusion; micropillar arrays[21,50] tune spacing to guide cell alignment *via* shear stress; perfusable vascular microchannels[51] enhance tissue barrier formation, nutrient/waste exchange, and cell–cell interactions. Despite significant advancements in OoC technology, systematic analyses of multichannel microfluidic chips and their implementation in OoC platforms remain underexplored in current research. This review is intended to provide a reference for the technological iteration and interdisciplinary application of multi-channel microfluidic chips. First, we conduct a critical analysis of their design paradigms, emphasizing dynamic control mechanisms and functional coupling strategies. Second, we evaluate the adaptability of advanced fabrication technologies in microfluidic channels and scaffolds. Third, we list different OoCs (*e.g.*, lung-on-chips, liver-on-chips, kidney-on-chips, and intestine-on-chips) based on multi-channel microfluidics by focusing on their applications in pathophysiological investigations,[12,52] preclinical drug evaluation,[47,53–55] and toxicological assessment.[56–58] Fourth, we discuss the bottlenecks of OoCs in structural design, materials and fabrication, biological applications, and other development directions (Table 1).

2. Overview of OoCs

2.1 Cell sources

In the realm of OoCs, cells serve as the cornerstone, playing a pivotal role in recapitulating physiological functions, constructing tissue-like architectures, and responding to diverse stimuli. Different cell types, including primary cells,

cell lines, stem cells, and organoids, contribute distinctively to the overall functionality of OoCs (Fig. 2a).

Primary cells, directly isolated from biological tissues without immortalization, retain natural cellular phenotypes, tissue-specific gene expression, and limited *in vitro* proliferation capacity. In OoC systems, these cells are primarily employed for high-fidelity modeling of organ physiology. Compared with immortalized cell lines, they exhibit higher predictive power for drug efficacy and toxicity and better replicate patient-specific variability. Recent studies have demonstrated that primary endothelial and astrocytic cells cultured in multi-channel blood–brain barrier (BBB)-on-chips reproduce endothelial–glial crosstalk and tight-junction formation,[64] while co-cultures of primary hepatocytes and hepatic stellate cells in liver-on-chips recapitulate fibrogenic activation and cytokine signaling under pathological stress. In addition, the use of biopsy- or iPSC-derived primary-like cells[65,66] enables personalized disease modeling and precision-drug testing. Their advantages include enhanced clinical predictability with reduced drug testing errors compared to cell lines, integration of complex functional interactions such as endothelial–glial cell crosstalk in BBB-on-chips, and potential for pathological mechanism analysis in fibrotic hepatic cell models, as well as personalized disease modeling using patient-derived samples.[65,66] The utilization of primary cell models remains constrained by biopsy-derived cell scarcity and technical challenges in dynamic microfluidic system integration, while operational expenditures are 5–10-fold higher than those of immortalized cell line experiments due to requirements for specialized infrastructure (*e.g.*, hypoxia chambers and ECM-coated microfluidic chips) and labor-intensive maintenance protocols necessitating daily medium replenishment and phenotype monitoring.[67,68] Thus, primary cells are the recommended choice for developing disease models associated with specific individuals or populations, emphasizing individual heterogeneity.

Cell lines, derived from primary cells or tissues and immortalized, are characterized by indefinite proliferation capacity and stable genetic traits.[68,69] They offer advantages such as ease of acquisition, culture, amplification, transfection, and stability, and their well-defined culture protocols and predictable cell behavior contribute to reproducibility in OoC construction. However, the high homogeneity and consistency of cell lines limit their application in personalized precision medicine. For studies requiring rapid model validation with simple workflows and lower costs, cell lines are optimal.

Stem cells are undifferentiated biological cells characterized by self-renewal capacity and the potential to differentiate into specialized cell types, thus playing critical roles in tissue regeneration, developmental biology, and regenerative medicine. Three major stem cell populations—embryonic stem cells (ESCs),[70] induced pluripotent stem cells (iPSCs),[71,72] and adult stem cells (ASCs)[73,74]—are widely utilized in OoC platforms, each contributing distinct functional advantages. ESCs, derived from blastocysts, exhibit pluripotent differentiation capacity into all three germ layers, making them essential for simulating early embryonic development and congenital diseases in microfluidic environments. iPSCs, reprogrammed from somatic cells, offer patient-specific pluripotency without ethical constraints, enabling applications such as neurodegenerative disease modeling and personalized drug screening. ASCs, residing in

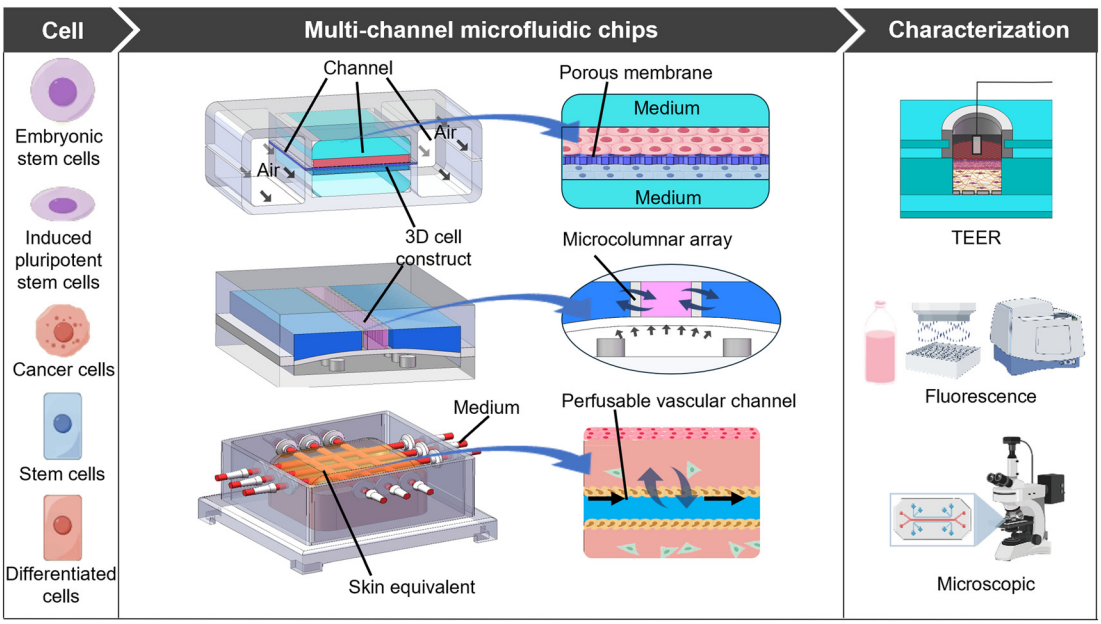

Fig. 2 Overview for the OoCs, including the cell sources, the representative structures of the multi-channel microfluidic chip platforms, and the characterization methods.

postnatal tissues, maintain multipotent regenerative potential, allowing OoC systems to recapitulate tissue homeostasis, age-related disorders, and stem cell niche interactions. ESCs provide broad differentiation potential, iPSCs address ethical limitations through somatic cell reprogramming, and ASCs enable native tissue repair mechanisms.

Spheroids, three-dimensional aggregates of one or multiple cell types, have recently emerged as an intermediate model bridging 2D monolayers and complex organoids.[75] They preserve native cell–cell and cell–ECM interactions and generate intrinsic oxygen, nutrient, and signaling gradients. When integrated into microfluidic OoC devices, spheroids improve tissue organization and functionality,[11,76–78] such as albumin secretion and cytochrome P450 activity in liver-on-chips,[79] or synchronous contraction in cardiac-on-chips.[80] Tumor spheroids combined with gradient-based microchannels further enable investigations of angiogenesis, invasion, and chemoresistance. Organoids represent a higher level of structural and functional organization.[81,82] They are principally categorized into two classes: tissue-derived organoids[83,84] and pluripotent-stem-cell-derived organoids.[85] Tissue-derived organoids, particularly patient-derived organoids, currently represent the most established platform for constructing tumor-disease models in precision oncology research.[86,87] Pluripotent-stem-cell-derived organoids are generated through differentiation protocols utilizing ASCs, ESCs, or iPSCs, enabling recapitulation of developmental processes and tissue morphogenesis. In addition, organoids offer distinct advantages, including developmental fidelity, genetic and cellular diversity, and personalized therapeutic potential through standardized models for toxicity testing and regenerative-cell replacement therapies.[11] However, existing organoid models only exhibit partial recapitulation of native tissue biology, with functional deficiencies in cellular composition, spatial organization, and microenvironmental interactions. Most organoids lack multicellular components (*e.g.*, immune cells, innervation, and vasculature) or inter-organoid communication, and organoid culture often requires labor-intensive manual operations and long experimental periods.[76,81]

2.2 Construction of OoCs with multi-channel microfluidics

Multi-channel microfluidics technology stands out with its flexible design, superior sealing properties, and precise control over microenvironmental parameters (Fig. 2b). This allows for the creation of complex, dynamic biomimetic environments in cell and tissue culture, accurately mimicking *in vivo* responses. Key factors involved in multi-channel microfluidics include physical factors, chemical factors, and biological factors. These factors play a crucial role in maintaining the physiological balance of cells within OoCs and mimicking more biomimetic cell–tissue interfaces.

Physical factors refer to mechanical and hydrodynamic stimuli that directly influence cell morphology and function.[19,24,88,89] These include fluid shear stress, laminar flow regimes, and pressure gradients, as well as geometric confinement, surface interfacial properties, mechanical stretching/compression, and electrical, optical, and thermal cues. Hydrodynamic parameters such as flow rate and pressure distribution are determined by channel geometries (shape, cross-section, and branching), which dictate nutrient delivery and waste removal.[15] Cyclic mechanical loading mimics organ-level deformation in cardiac and pulmonary chips,[22] while shear forces guide endothelial alignment and permeability regulation.[20] Electrical and optical stimuli enable precise control of electrophysiological activity and gene expression,[36] whereas temperature and gas permeability maintain metabolic stability and enzyme function.[23] Together, these cues replicate the dynamic mechanical and physicochemical landscape of living tissues.

Chemical factors encompass non-biological physicochemical parameters that define the composition and gradient distribution within the microfluidic environment.[19,24,88,90] These include oxygen and carbon dioxide concentrations, pH, ionic strength, nutrients, metabolites, and exogenous compounds (such as drugs or toxicants).[90] Oxygen gradients modulate hypoxia-inducible signaling and metabolic activity,[91,92] while carbon dioxide regulates acid–base homeostasis *via* bicarbonate buffering.[19,24] Controlled nutrient and metabolite gradients (*e.g.*, glucose, lactate, and amino acids) allow modeling of metabolic zonation and tissue-specific energy balance.[14,17,93] Small-molecule drugs and toxicants serve as precise modulators for assessing pharmacodynamics and cytotoxicity under perfusion conditions.[18,20,21,43] Additionally, ionic gradients (Ca^{2+}, K^{+}, and Na^{+}) govern electrophysiological functions in excitable tissues and influence intracellular signaling cascades.[22]

Biological factors refer to biomolecular and cellular components derived from living systems, mediating intercellular communication and structural organization.[19,24,88] These include cytokines, growth factors, ECM molecules, and biomaterial biocompatibility.[88] Cytokines and growth factors regulate cell proliferation, differentiation, and immune responses;[11,66] for example, vascular endothelial growth factor (VEGF) gradients drive angiogenic sprouting,[76,94] while inflammatory cytokines such as TNF-α and IL-6 modulate barrier permeability.[23] The ECM provides both mechanical support and biochemical signaling cues that guide cell adhesion, migration, and tissue morphogenesis.[88] Additionally, the biocompatibility of materials used in chip fabrication ensures minimal immune activation and sustained cellular viability.[95] Collectively, these biological signals orchestrate multi-layered tissue organization and enable dynamic, feedback-regulated modeling of physiological and pathological processes.

Multi-channel microfluidic systems provide a highly controllable framework to integrate these three domains—physical, chemical, and biological factors—for the reconstruction of physiologically relevant microenvironments.

By leveraging precise flow control and structural modularity, OoC devices can simultaneously recreate mechanical stimulation, metabolic gradients, and biochemical signaling, advancing the fidelity of *in vitro* disease modeling and drug testing.[28] In OoC research, the primary engineering objective lies in constructing tissue interfaces that maintain selective barrier functions or develop functional parenchymal tissues. Barrier tissues such as alveoli, oral and nasal mucosa, intestinal epithelium, and skin are continuously exposed to complex physiological interfaces, including air–liquid, host–microbe, and host–environment interfaces.[23,25,96] These interfaces are not only structurally compartmentalized but also dynamically regulated by biochemical and mechanical cues that maintain epithelial homeostasis and barrier integrity. Conventional single-channel systems often fail to recapitulate the coordinated physiological processes that occur across these interconnected interfaces. Multi-channel OoCs offer an effective solution to these challenges. By integrating spatially separated microenvironments with precisely controlled fluidic networks, multi-channel designs enable the simultaneous reconstruction of multiple physiological interfaces within a single device. This architecture allows orderly intercompartmental communication and dynamic simulation of key physiological processes—such as epithelial barrier permeability regulation, immune cell trafficking, microbial colonization, and responses to environmental or chemical stimuli—under near-physiological conditions.[12,27,49,97]

Three main approaches are employed to create tissue interfaces in OoCs. The first utilizes porous membranes and micropillar arrays, which allow co-culture of different cell types on opposite surfaces while regulating convective–diffusive mass transport and maintaining liquid–liquid or air–liquid interfaces. Porous membranes enable the culture of different types of cells on their upper and lower surfaces. Micro-sized pores not only allow cell migration but also maintain the stability of the gas–liquid interface or liquid–liquid interface on both sides of porous membranes.[98,99] An air–liquid interface between lung epithelial and endothelial cells was successfully constructed by culturing these cell types on opposing sides of a porous membrane integrated within a multi-channel microfluidic chip. Building upon this concept, similar vertically aligned dual-channel architectures have been employed in oral epithelial chip models, where a porous membrane separates the upper air-exposed channel from the lower medium-perfused channel.[2,20,23] This air–liquid interface configuration facilitates epithelial polarization and the formation of tight junctions, both critical for preserving physiological barrier selectivity and permeability. In addition, host–microbe interface models extend this design to parallel or layered microchannel configurations, enabling the spatial co-culture of host cells and microorganisms under controlled shear flow conditions.[96,100] Such systems maintain microbial viability while allowing real-time visualization of host–pathogen interactions and inflammatory signaling. Moreover, host–environment interface models often incorporate lateral perfusion channels or exposure chambers to deliver aerosols, nanoparticles, or chemical agents in a precisely controlled manner, thus enabling dynamic assessment of epithelial and immune responses to external stimuli.[20,101,102]

Parallel micropillar arrays serve as another important structure for constructing tissue interfaces because they demonstrate precise regulation of fluid shear stress through interpillar spacing, thereby guiding directional cell alignment and enabling controlled cultivation of oriented cells.[21,50,103,104] In addition, by leveraging the geometrically coupled membrane–micropillar composite architecture, multi-channel microfluidic chips enable multiplexed reconstruction of physiologically critical tissue–tissue interfaces.[103] This integrated design simultaneously ensures mechanical stabilization through micropillar arrays and facilitates spatially controlled convective–diffusive transport across interconnected microchannels, thereby recapitulating *in vivo* mass transfer dynamics. An alternative approach involves template removal from the ECM. Using templating techniques, hollow channels can be fabricated within ECM hydrogels.[31,88] This configuration allows a separate culture of different cell types along the channel lumen and hydrogel periphery, establishing defined tissue interfaces. The hydrogel matrix simultaneously supports cell seeding, enhances barrier formation, preserves nutrient/waste exchange, and mediates tissue–tissue interactions. Perfusable vascular microchannels, fabricated through sacrificial templating techniques—utilizing dissolvable gelatin fibers[51] or microtubules[94]— generate biomimetic branched microchannels that recapitulate capillary network topology while enabling organ-specific spatial patterning *via* the micro-pump and micro-valve confinement.[17] Modular perfusable vascular microchannels enhance functional integration by enabling multi-tissue metabolic crosstalk modeling through programmable fluidic interconnections.[31,76,105]

While these enclosed architectures ensure precise perfusion control and microenvironmental stability, certain physiological interfaces, such as air–liquid,[23] host–microbe,[100] or host–environment interactions,[106] require open or half-open channel configurations. These designs enable direct gas exchange, sampling access, and optical interrogation, but they also introduce several engineering and operational challenges that require careful control. Evaporation is a major concern due to exposed liquid interfaces; it can rapidly alter medium osmolarity and concentration gradients within hours. This issue is typically mitigated by employing humidity-controlled incubators (>95% RH), overlaying sterile mineral oil films, or using microreservoir sealing films that minimize water loss to <5% over 24 h.[107] Contamination risk increases with open geometries, thus sterile fabrication, on-chip filtration, and periodic medium replacement under laminar-flow hoods are essential for maintaining aseptic conditions over long-term culture.[108] Meniscus and edge-pinning effects at open

interfaces may generate non-uniform shear stress and uneven nutrient distribution; these can be reduced by hydrophilic surface coatings, rounded channel edges, or capillary barrier designs that stabilize the contact line.[107,109] In terms of biological compatibility, open or half-open channels are best suited for cell types requiring direct air or environmental exposure, such as epithelial cells (alveolar, intestinal, or skin keratinocytes) and microbial co-culture systems, as well as organoids requiring oxygen-rich interfaces. Typical culture durations range from 3–7 days for short-term epithelial barrier modeling to 2–3 weeks for stratified tissue formation or chronic exposure studies.[110] When properly maintained, these architectures provide unique physiological advantages —realistic air–liquid or host–environment interfaces—while maintaining acceptable operational stability and reproducibility for experimental use.

These integrated designs collectively ensure mechanical stability, spatially resolved nutrient exchange, and physiologically accurate tissue–tissue communication, representing the foundation of next-generation multi-channel OoC platforms (Fig. 2b). Together, these design variations expand the versatility and biomimetic potential of OoC platforms, allowing precise modulation of chemical, biological, and physical parameters to emulate *in vivo* complexity. A comprehensive characterization framework is therefore essential to quantitatively link these structural features to functional performance, as discussed in the following section.

2.3 Characterization

A fundamental principle in OoC engineering is that microstructural design dictates functional performance, and appropriate characterization metrics must quantitatively capture these structure–function relationships.[63,90,111] Each microarchitectural element within multi-channel microfluidic systems serves a distinct physiological purpose and therefore requires specific readouts and threshold indicators to validate functional fidelity. For instance, micropillar arrays are primarily used to guide cell alignment, elongation, and mechanical responses, which can be quantitatively evaluated by image-based orientation analysis and traction force microscopy to assess contractile anisotropy.[50] Porous membranes, commonly used to construct barrier-type OoC models, are characterized by tight junction integrity staining and molecular permeability assays.[23] Perfusable vascular channels, which replicate blood flow and nutrient exchange, are evaluated by vascular barrier integrity (*e.g.*, FITC–dextran leakage) and metabolic exchange rates (*e.g.*, glucose or oxygen gradients).[13,112] Apart from establishing these quantitative readouts and performance thresholds for the evaluation of structure–function relationships, other main characterization frameworks encompass multidimensional parameters, including material properties (mechanical strength, biocompatibility, transparency, and hydrophobicity),[62,95] fluidic dynamics (wettability, shear stress, flow rate, and oxygen concentration gradients),[14,17] and biological characterization (tissue integrity, cell proliferation, cell morphologies, and gene expression).[113–115] Herein, we focus on the biological characterization (Fig. 2c).

Tissue integrity, a critical parameter for evaluating engineered tissue functionality and barrier properties, is commonly assessed *via* transepithelial electrical resistance (TEER) measurements.[116,117] This non-invasive, label-free method quantifies the electrical resistance of cell monolayers, directly reflecting the tightness of intercellular junctions and barrier integrity. Tight junctions restrict paracellular ion flow through selective pathways, elevating TEER values that correlate with enhanced cell adhesion and robust barrier function. Its high sensitivity, rapid implementation, and applicability across diverse tissue types (*e.g.*, epithelial and endothelial) make TEER an indispensable tool in OoC research and tissue engineering for real-time monitoring of *in vitro* tissue health and permeability dynamics.[106,114,118]

Cell proliferation, a key indicator in biomedical research, is crucial for understanding cell behavior, drug responses, and disease progression. Common methods for assessing cell proliferation include methylthiazolyldiphenyl-tetrazolium bromide (MTT)[119] and cell counting kit-8 (CCK-8) assays.[120,121] The MTT assay relies on mitochondrial succinate dehydrogenase in viable cells to reduce the yellow MTT into water-insoluble purple formazan crystals, with the formazan quantity being proportional to cellular metabolic activity. The CCK-8 assay uses a yellow WST-8 solution that turns orange when exposed to living cells. Active cells produce enzymes that chemically alter WST-8, creating a color change visible at 450 nm. The darker the orange color is (higher absorbance), the more live cells are present. Unlike MTT methods, this test requires no additional chemicals to dissolve cells.

Cellular morphologies directly reflect cell growth, physiological responses, and pathological changes of cells within biomimetic microenvironments, serving as a critical indicator for evaluating chips and the validity of experiments. Advanced optical imaging platforms,[63] notably laser scanning confocal microscopy and fluorescence microscopy, provide non-invasive longitudinal monitoring of spatiotemporal cellular dynamics through spectral unmixing algorithms. Confocal microscopy employs monochromatic laser excitation coupled with a point-scanning mechanism to achieve optical sectioning through pinhole-assisted background rejection, enabling high-resolution 3D reconstruction *via* *z*-axis stepping motors and deconvolution algorithms. Fluorescence microscopy visualizes cellular structures by inducing fluorescent molecules to emit longer wavelength light. Although facing challenges in sample preparation and potential phototoxicity, these techniques are indispensable in OoC research for monitoring cell growth, morphologies,

interactions, and drug responses.[2] Laser scanning confocal microscopy suffers from inherent phototoxicity and limited temporal resolution, and conventional fluorescence microscopy remains constrained by diffraction-limited spatial resolution and persistent out-of-focus artifacts. Future advancements are directed toward enhancing resolution, reducing phototoxicity, and integrating additional functionalities to address complex research needs.

Gene expression profiling captures dynamic cellular responses to engineered biomimetic environments, encompassing pathophysiological states, pharmacodynamic effects, and mechanotransduction signaling through transcriptomic signatures.[19,24] Typical techniques used to characterize gene expression include polymerase chain reaction,[122] reverse transcription quantitative polymerase chain reaction,[123] and high-throughput sequencing.[124] These methods enable real-time monitoring of cellular gene expression, offering high sensitivity and throughput while effectively minimizing interference from non-specific signals. However, gene-level characterization alone may not fully capture downstream phenotypic changes, as transcriptional and translational regulation can diverge under dynamic microfluidic conditions. Comprehensive transcriptomic sequencing therefore provides a systems-level view of how fluidic shear, mechanical strain, and intercellular signaling remodel cellular states within OoC platforms. RNA-seq or single-cell RNA-seq analyses enable the identification of pathway enrichment (*e.g.*, ECM remodeling, oxidative stress, metabolic adaptation) and uncover cell-type-specific responses that are otherwise masked in bulk assays.[125–127] Protein expression characterization provides a more direct functional readout of the cellular status within OoC systems.[19,24,128] Protein-level assays, including western blotting,[129] enzyme-linked immunosorbent assay (ELISA),[130] immunofluorescence staining,[131] and mass-spectrometry-based proteomics,[132,133] enable quantitative and qualitative evaluation of structural and functional proteins. Western blotting and ELISA facilitate targeted detection of tight-junction proteins (*e.g.*, ZO-1 and occludin), transporters, and signaling molecules to assess barrier integrity, metabolism, and stress responses.[59] Immunofluorescence microscopy allows spatial visualization of protein localization and intercellular junction continuity within microchannels.[20] In parallel, proteomic profiling using liquid chromatography-mass spectrometry (LC-MS/MS) uncovers global protein expression patterns and post-translational modifications, providing system-level insights into organ-specific functions, inflammatory pathways, and drug responses. Integrating gene and protein expression analyses yields a holistic understanding of cellular behavior in multi-channel OoC platforms.[132,133] While transcriptomic data reveal upstream regulatory dynamics, proteomic characterization reflects actual enzymatic activity and secretory function, jointly strengthening model validation and translational relevance. It is anticipated that this integrated multi-omics approach will assume an increasingly pivotal role in future OoC technology, enabling deeper insights into mechanistic pathways and therapeutic efficacy evaluation.

2.4 Regulatory, standardization, and reproducibility considerations

Although OoC technologies have rapidly evolved toward physiologically relevant microphysiological systems, regulatory acceptance and translational reproducibility still face major challenges due to the lack of standardization across materials, fabrication protocols, and reporting formats. The field urgently requires harmonized validation and reporting frameworks to ensure inter-study comparability and facilitate integration into drug development pipelines and regulatory evaluations by agencies such as the U.S. FDA and European EMA.

A key technical barrier arises from material adsorption and drug recovery in polymeric chip substrates, particularly PDMS, which can absorb over 60% of lipophilic drugs and volatile molecules, significantly skewing pharmacokinetic and dose–response measurements.[134,135] To mitigate these effects, the use of low-adsorption polymers (*e.g.*, COC, PMMA, and PTFE) or surface coatings such as parylene-C, PEGylation, or plasma polymerization has been demonstrated to improve molecular recovery and bioassay reproducibility.[95] Equally critical is batch-to-batch consistency in both device fabrication and biological inputs. Variations in microchannel dimensions, ECM composition, and the cell differentiation state (particularly when using iPSC-derived cardiomyocytes or hepatocytes) can lead to inconsistent tissue morphogenesis and functional output.[19] Implementing defined media, standardized cell banks, and automated flow control systems with traceable calibration protocols has been proposed as a prerequisite for quality assurance.[19] Furthermore, cross-laboratory reproducibility remains limited; the same microphysiological design can yield divergent results due to subtle differences in the chip geometry, pump pulsatility, or imaging endpoints.[19]

To promote transparency and facilitate regulatory translation, a minimum reporting checklist is recommended: 1) device metadata: material composition, dimensions, membrane characteristics, and surface modification; 2) cell metadata: origin (primary/iPSCs), passage, seeding density, differentiation protocol, and co-culture details; 3) operational parameters: flow rate, shear stress, residence time, temperature, and medium formulation; 4) analytical controls: drug recovery %, adsorption testing, calibration of biosensors, and internal standards; 5) functional validation: physiological benchmarks (*e.g.*, TEER, OCR, beating rate, CYP activity, and hormone secretion); 6) reproducibility metrics: replicate number, coefficient of variation (CV%), and inter-laboratory comparison results. Such standardized metadata

and performance documentation would substantially enhance the reproducibility, transparency, and regulatory readiness of OoC systems, supporting their use as validated preclinical tools for drug efficacy, safety, and toxicology testing.[136,137]

3. Fabrication of multi-channel microfluidics for OoCs

Multi-channel microfluidic systems directly dictate the structural fidelity, inter-compartmental connectivity, and functional controllability of OoC platforms. In fabricating such systems, key parameters including minimum feature size, surface roughness, layer adhesion, alignment accuracy, and production throughput must be carefully balanced with material-dependent factors such as solvent and temperature compatibility, bonding strength, scalability, and cost.[19,24,26,28] A summary of representative performance ranges for different fabrication technologies (*e.g.*, soft lithography,[48] digital light processing (DLP),[138] stereolithography (SLA),[139] fused filament deposition (FDM),[140] two-photon polymerization (TPP),[141] laser

Table 2 Comparative summary of commonly used fabrication methods and corresponding materials used for multi-channel microfluidic OoCs systems

Fabrication method	Compatible materials	Fabrication process	Multi-channel strategy	Resolution & throughput	Advantages	Limitations	Ref.
Soft lithography	PDMS, SU-8, glass	Photolithography to pattern the SU-8 mold → PDMS casting → plasma bonding to the substrate	Multi-layer stacking with alignment marks; vertical channel interconnection *via* punched vias; integrated partition walls for parallel channels	~5–10 μm resolution; moderate throughput (10–20 chips per day)	Excellent optical transparency, gas permeability, and elasticity; biocompatible; low-cost prototyping	Limited scalability; hydrophobic recovery; high small-molecule absorption; poor solvent compatibility	48, 144
Sacrificial templating	PDMS, PEG, PVA, glass	Embed dissolvable templates (*e.g.*, sugar and PVA fibers) in elastomer → cure → dissolve templates to form hollow channels	Enables complex 3D branching or vascular-like multi-channel networks; ideal for perfusable interconnections	10–100 μm feature size; low-to-moderate throughput	True 3D architectures; compatible with soft biomaterials and hydrogels; flexible channel geometry	Template removal may deform soft matrices; limited precision; poor reproducibility	88, 145, 146
3D printing (DLP/SLA)	Photocurable resins, PEGDA, GelMA, COC	Layer-by-layer UV-curing of photopolymer; CAD-controlled geometry	Multi-compartment printing; embedded microvalves; fluid routing *via* printed manifolds or hollow interconnections	25–100 μm *XY*, 25 μm *Z*; moderate throughput	High design flexibility; rapid prototyping; precise 3D alignment; good surface finish	Material biocompatibility and gas permeability depend on resin; post-curing and leaching needed	138, 139, 147
3D printing (FDM/TPP)	Thermoplastics (PLA, ABS, COC, PMMA), photoresists	Fused filament deposition (FDM) or femtosecond two-photon polymerization (TPP)	FDM: modular channel assembly; TPP: nanoscale compartment coupling; suitable for integrated valves	FDM: 100–200 μm; TPP: <1 μm; FDM: high throughput, TPP: low	FDM: low-cost, scalable; TPP: ultra-high precision, ideal for nanofluidics	FDM: limited transparency and rough surfaces; TPP: costly, slow, and limited volume	140, 148
Injection molding	Thermoplastics (PMMA, COC, PC)	Fabricate the metal mold → polymer injection → demolding → thermal/ultrasonic bonding	Partition walls and routing defined in the mold; multi-layer alignment for complex routing; scalable batch production	~20 μm resolution; high throughput (>1000 chips per day)	Excellent reproducibility and scalability; good solvent resistance; industrial compatibility	High upfront mold cost; limited flexibility for rapid iteration; moderate optical clarity	149
Laser ablation	PMMA, COC, glass, metals	CO_2 or femtosecond laser engraving to ablate channel patterns; optional polishing or bonding	Sequential channel routing and interconnections *via* laser passes; flexible for 2.5D channel networks	25–100 μm precision; moderate throughput (minutes per chip)	Maskless and direct-write; rapid prototyping; compatible with thermoplastics	Rough surfaces; thermal stress cracks; poor elasticity; limited 3D capability	142, 150
CNC micro-milling	PMMA, COC, PC, metals	Mechanical removal using micro-end mills; channels sealed by thermal or adhesive bonding	Multi-level routing by layered milling; allows integration of sensors/electrodes and embedded connectors	~50–100 μm precision; moderate throughput	High dimensional accuracy; reusable molds for injection replication; robust material choices	Limited for soft materials; surface roughness; high equipment cost	151, 152

ablation,[142] and computer numerical control (CNC)[143] is provided in Table 2 for quick reference.

3.1 Template methods

Soft lithography (Fig. 3a) is the most typical and widely used template method. It demonstrates significant advantages in the field of OoC technology, which utilizes ultraviolet (UV) or electron beam lithography to create high-resolution (feature resolution: 1–50 μm) master molds (typically on silicon/glass substrates).[153] The process involves casting liquid polydimethylsiloxane (PDMS) prepolymer onto molds, followed by thermal curing (60–80 °C for 1–4 hours) and demolding to constitute microchannels.[154–156] PDMS has quickly become the most prevalent substrate for biological microfabricated devices because of its low cost, ease of processing, intrinsic elasticity, optical transparency, gas permeability, and biocompatibility.[157]

In the context of multi-channel OoC fabrication, soft lithography enables multilayer assembly through plasma bonding or adhesive lamination, allowing vertical and lateral channel stacking.[144] This facilitates the creation of parallel perfusion networks and porous-membrane-separated compartments that mimic vascular–epithelial interfaces. Furthermore, hybrid PDMS–glass bonding supports cross-layer channel interconnection, enabling precise fluid routing and bidirectional molecular exchange across compartments. However, PDMS inherently tends to adsorb small molecules, and its long-term hydrophobicity compromises cell viability in biological applications. Furthermore, scaling up production with soft lithography faces technical limitations, including structural shrinkage during PDMS curing.[48] Future advancements may involve developing novel biomaterials to replace PDMS or integrating complementary techniques such as 3D bioprinting and electrospinning to construct microchannels.

Nylon microfilaments,[94] microneedles,[158] and sacrificial hydrogels[145] are also employed as templates to fabricate hollow channels, especially vascular hydrogel networks.[159] The technology involves filling a pre-designed mold with curable or sacrificial materials. Once the ECM hydrogel is set, the template is removed, creating hollow channels

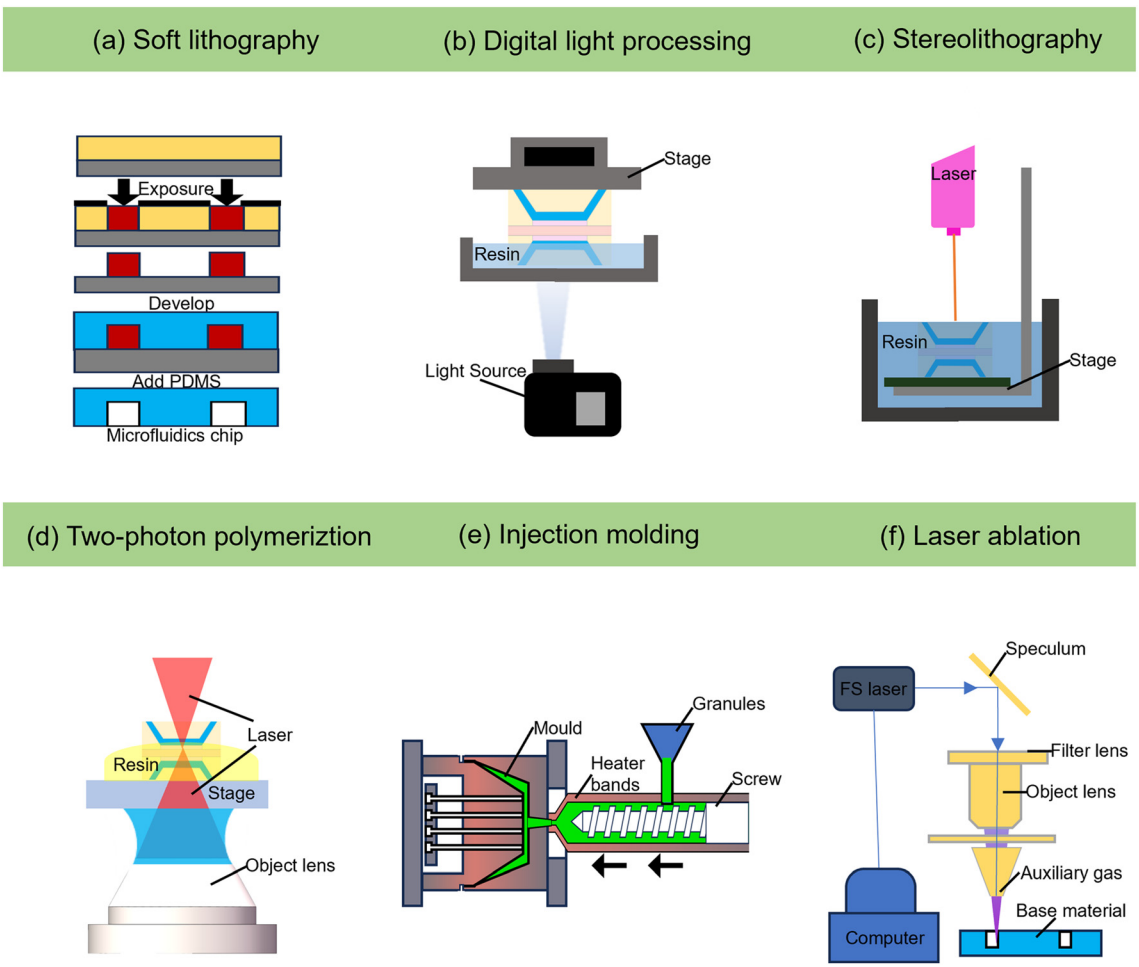

Fig. 3 Fabrication methods for OoCs. (a) Soft lithography. (b–d) 3D printing techniques based on digital light processing (b), stereolithography (c), and two-photon polymerization (d). (e and f) Other methods: injection molding (e) and laser ablation (f).

within the ECM hydrogel. The fabricated hollow channels enable the culture of vascular endothelial cells within the channels, forming a targeted tissue interface. The hydrogel matrix not only facilitates cell seeding and promotes robust tissue barrier formation but also supports nutrient/waste exchange and cell–cell interactions within the microenvironment.[146,160]

3.2 3D printing

3D printing enables precision fabrication of OoC systems *via* additive manufacturing, constructing biomimetic vascular networks and multi-layered microfluidic channels with sub-100 μm resolution.[161] Advanced 3D printing techniques based on extrusion or photopolymerization enable the design of complex geometries and internal channels in multi-channel microfluidic chips. Currently, the main 3D printing technologies include DLP (Fig. 3b), SLA (Fig. 3c), FDM, and TPP (Fig. 3d).

DLP technology utilizes UV light projection with dynamic mask control through micromirror arrays to achieve layer-wise photopolymerization of 3D models, enabling 10–100 μm resolution solidification *via* large-area parallel exposure.[162] Key parameters include layer thickness (20–200 μm),[138] exposure intensity, and curing time, which are optimized for material viscosity and feature fidelity. In multi-channel OoC applications, DLP printing allows the fabrication of branched and parallel microchannel arrays within a single resin body. Integrated cross-linking layers or porous interfaces can be printed between channels, creating dual perfusion systems that simulate vascular–parenchymal coupling, as in liver- or BBB-on-chip designs. DLP's scalability supports both lab-scale prototyping and industrial production, while its high precision enables applications in microfluidics, tissue engineering, and customized medical devices.[163] There are still limitations to address, such as resin shrinkage and the restricted availability of materials capable of withstanding high temperatures and chemical exposure. Recent advancements in nanoparticle-doped resin and grayscale curing techniques, however, are effectively expanding the functional scope of DLP technology.[147]

SLA utilizes a focused UV laser (wavelength: 355–405 nm)[164] to selectively polymerize photopolymer resin in a layer-by-layer fashion, achieving high-precision microstructures with resolutions of 10–150 μm.[139] The process begins with 3D model slicing into digital layers, followed by laser scanning *via* galvanometer mirrors, solidifying liquid resin with controlled curing depths. Key parameters of SLA include laser power (20–500 mW), scanning speed, and layer thickness (25–200 μm).[165] Post-processing steps involve rinsing in solvents to remove uncured resin and UV post-curing to enhance mechanical stability. SLA's compatibility with biocompatible resin and ceramic-loaded formulations enables applications in dental implants, micro-optics, and aerospace components requiring smooth surfaces. This technique is particularly powerful for printing compartmentalized chambers and interconnecting ducts in multi-channel architectures, enabling asymmetric flow distribution and vertical diffusion coupling across stacked microtissues.

FDM constructs 3D objects by extruding the heated thermoplastic filament through a precision nozzle (diameter: 0.2–0.8 mm) in a layer-by-layer manner, achieving feature resolutions of 50–400 μm.[140] Leveraging open-source platforms like RepRap, researchers have demonstrated the cost-effective fabrication of transparent, sealed microfluidic channels using PLA, a biodegradable polymer with a 6–12 month degradation cycle. Key process parameters of FDM include layer height (0.1–0.3 mm), print speed (30–100 mm s^{-1}), and bed temperature (50–110 °C), optimized for interlayer adhesion and dimensional stability.[32] For multi-channel OoCs, FDM excels in printing modular manifolds and recirculating flow loops that link multiple organ compartments or replicate body-on-a-chip circulatory systems. Integrated inlet–outlet connectors and channel manifolds provide scalable fluidic interconnection across modules.

TPP, a nanoscale 3D fabrication technology based on two-photon absorption, employs femtosecond lasers to initiate spatially confined polymerization in photosensitive resin through precise focal point scanning.[166] This technique achieves sub-100 nm resolution beyond optical diffraction limits while enabling freeform manufacturing of intricate architectures like overhanging structures and hollow microtubes.[141,148] Its material compatibility spans acrylates, epoxies, organic–inorganic hybrid composites, and hydrogels. Nevertheless, inherent constraints include millimeter per hour-scale production speeds from pointwise processing and substantial equipment investments for ultrafast laser systems. In multi-channel chip fabrication, TPP enables hierarchical coupling between capillary-scale networks and larger conduits within a continuous 3D construct—realizing true "microvascularized" organ-on-a-chip systems. Overall, 3D printing integrates design flexibility with digital control, allowing OoCs to progress from planar dual-channel structures to fully 3D, multi-compartmental fluidic architectures.[167]

3.3 Other technologies

Currently, in addition to soft lithography and 3D printing techniques, other fabrication methods such as injection molding (Fig. 3e), laser ablation (Fig. 3f), and CNC micro-milling are also employed. Injection molding, laser ablation, and CNC micromilling are also employed in multi-channel chip fabrication due to their scalability and material versatility. Injection molding involves injecting thermoplastic polymer melts into precision-engineered cavities, achieving micron-scale fidelity. Through multi-cavity mold design, injection molding can replicate

parallel microchannel arrays and integrate manifold connectors to establish multi-channel flow routing. It enables industrial-scale production of modular, multi-channel chips suitable for pharmacokinetic screening or high-throughput assays.

Injection molding, renowned for its manufacturing efficiency, is especially suitable for large-scale production. The injection molding process involves the thermoplastic polymer melt being plasticized and injected under high pressure into a precision-engineered mold cavity, followed by controlled cooling and demolding phases. Injection molding excels in precision manufacturing (producing sub-gram components, micron-scale features like micro gears, and intricate 3D structures),[168] material versatility, and high-speed, automated production with optimized cycle times, enabling scalable and cost-effective fabrication of complex devices such as microfluidic chips. Emerging hybrid approaches combine injection molding with laser ablation for sub-25 μm vascular networks, while in-mold UV grafting enables direct surface biofunctionalization without post-processing.[149] Through multi-cavity mold design, injection molding can replicate parallel microchannel arrays and integrate manifold connectors to establish multi-channel flow routing. It enables industrial-scale production of modular, multi-channel chips suitable for pharmacokinetic screening or high-throughput assays.

Laser ablation employs high-energy pulsed laser beams (*e.g.*, excimer lasers at a wavelength of 193–355 nm and femtosecond lasers at a wavelength of 1030–1064 nm)[142,169] to selectively remove materials through photothermal or photochemical interactions, achieving micron-to-submicron precision. The process involves focusing the laser beam onto a substrate (*e.g.*, polymers, glass, and metals) using optical lenses, with material removal rates controlled by pulse duration, fluence, and repetition frequency.[170] For microfluidic device fabrication, UV lasers are commonly used to engrave channels in materials like PMMA or polycarbonate (PC), achieving optical-grade surface finishes. This technique offers several distinct advantages, including non-contact processing that minimizes thermal damage to heat-sensitive substrates, the capability to produce complex 2.5D geometries without inducing mechanical deformation, and seamless multi-material processing[171] enabled by adjustable wavelength configurations. However, laser ablation still faces several challenges, including limited throughput for large-area patterning and potential thermal damage in nanosecond-pulse regimes. Recent advancements in burst-mode femtosecond lasers and beam-shaping optics have enhanced ablation efficiency and enabled submicron features in glass substrates. By patterning intersecting or gradient microchannels directly onto polymer substrates, laser ablation creates asymmetric, serially coupled channel systems—suitable for simulating tissue-to-tissue transport gradients and controlled flow partitioning in multi-channel OoCs.[150]

CNC micro-milling is a precision subtractive manufacturing technique that employs computer-guided rotary tools (*e.g.*, carbide end mills with diameters of 0.1–2 mm) to machine metals, polymers, and composites.[151,152] The process utilizes CAD/CAM-generated toolpaths to precisely control spindle speeds, feed rates (50–500 mm min^{-1}), and cutting depths, achieving dimensional tolerances of ±5 μm and surface roughness values ranging from 0.2 to 1.6 μm.[172] A notable advantage of this method is its ability to machine threads and undercuts without requiring post-processing, while also maintaining compatibility with optical-grade surfaces.[143] It is particularly suited for producing base plates and manifold layers that interconnect PDMS or glass channel modules, thus forming integrated multi-channel chip assemblies with mechanical rigidity and modular reconfigurability. This versatility further enables the fabrication of intricate structures such as microfluidic channels, microlens arrays, and injection cavities. Although its resolution is limited compared to lithographic methods, CNC micro-milling remains indispensable for prototyping high-strength micro-components and advancing the fabrication of microelectromechanical systems and optical devices.

Overall, PDMS-based soft lithography remains dominant for biological fidelity and multi-channel alignment, ideal for early-stage OoC prototypes. Sacrificial templating excels at vascularized 3D networks and tissue perfusion models but suffers from limited reproducibility. DLP/SLA 3D printing bridges rapid prototyping and complex fluid routing, whereas TPP targets nano-scale precision for barrier interfaces (*e.g.*, BBB). Injection molding and CNC milling enable mass production of rigid thermoplastic chips, suited for standardized multi-organ platforms. Laser ablation offers rapid iteration for channel partition optimization and coupling geometry testing. Collectively, these fabrication techniques enable scalable and high-fidelity construction of multi-channel microfluidic architectures. By integrating template-based lithography, 3D volumetric printing, and precision machining, researchers can achieve tailored partitioning, hierarchical flow control, and multi-tissue coupling. Future multi-channel OoC platforms are expected to evolve toward process–structure–performance co-optimization, achieving hierarchical vascularization, compartmentalized signaling, and systemic perfusion modeling.[173]

3.4 Comparison of fabrication techniques and material choices for multi-channel OoC systems

Various fabrication approaches have been developed for constructing multi-channel OoCs, each presenting distinct advantages, limitations, and trade-offs in terms of resolution, scalability, complexity, and material compatibility (see Table 2).

Template methods such as soft lithography remain widely used due to high feature resolution (1–50 μm), optical transparency, and ease of integration with PDMS-based systems. PDMS offers biocompatibility, gas permeability, and mechanical flexibility, making it ideal for cell culture. However, its inherent absorption of small molecules and hydrophobicity may limit long-term pharmacological studies, and planar fabrication constrains true 3D geometries.[174] Sacrificial templates—including nylon microfilaments, microneedles, and hydrogel networks—enable hollow channel formation within ECM or hydrogel matrices, allowing vascular endothelial cell culture and enhanced nutrient/waste exchange. The main trade-offs include limited scalability and potential mechanical fragility of hydrogel-based structures. Injection molding offers high throughput, micron-scale precision, and suitability for large-scale production, although it requires complex mold fabrication and initial tooling investment.

3D printing (additive manufacturing) enables rapid prototyping of complex, multi-layered microchannels with customizable geometries. SLA and DLP achieve high precision (10–150 μm) and are compatible with biocompatible or ceramic-loaded resins, supporting branched, perfusable networks.[175] FDM allows cost-effective fabrication with thermoplastics like PLA,[176] while TPP enables nanoscale resolution (<100 nm) for intricate architectures.[177] Challenges include limited surface smoothness, bonding reliability, material restrictions, and relatively slow throughput for ultrahigh-resolution methods.

Injection molding offers high throughput, micron-scale precision, and suitability for large-scale production, although it requires complex mold fabrication and initial tooling investment.[178] Laser ablation provides non-contact micromachining of polymers and glass with submicron precision, making it suitable for 2.5D and intricate geometries. However, its throughput remains limited, and localized thermal effects may occur. CNC micro-milling enables rapid prototyping of high-strength, complex microstructures with optical-grade surface finishes, though its resolution is generally lower than that of lithographic or laser-based techniques.[179,180]

Hybrid fabrication approaches, which combine soft lithography with 3D printing or sacrificial templating, effectively integrate the geometric precision of photolithography with the structural versatility of additive manufacturing.[181] Such strategies enable the creation of hierarchical multi-channel architectures with improved multi-material compatibility and scalability,[182,183] providing a promising route toward the next generation of physiologically relevant OoC platforms.

Material considerations are critical for multi-channel OoC systems. PDMS remains widely used for elasticity and gas permeability but suffers from small-molecule adsorption.[184] Glass offers chemical inertness and optical clarity but is brittle.[185] Thermoplastics such as PMMA and COC provide lower permeability, better chemical resistance, and suitability for injection molding.[186] Hydrogel-based matrices enhance biocompatibility and structural flexibility, particularly for vascularized tissue modeling, but may lack mechanical robustness.[187] Collectively, the choice of fabrication method and material must balance precision, scalability, chemical/biological compatibility, and ability to support complex, perfusable multi-channel architectures, all of which are essential for physiologically relevant OoC platforms capable of recapitulating inter-organ communication and dynamic perfusion.[25]

4. Applications of multi-channel microfluidics in OoCs

Multi-channel microfluidic chips have emerged as a cornerstone technology for developing OoC systems, enabling the construction of sophisticated models such as heart-on-a-chip, lung-on-a-chip, liver-on-a-chip, kidney-on-a-chip, intestine-on-a-chip, brain-on-a-chip, skin-on-a-chip, and multi-organ systems. By recapitulating physiological and pathological conditions *in vitro*, these systems significantly advance precision medicine by bridging the gap between traditional cell culture models and clinical trials. Table 3 lists some typical OoCs based on multi-channel microfluidics and their fabrication methods, materials, key microstructures, chip design, fluidic conditions, biological readouts, and functions. Multi-channel OoC systems provide clear advantages over single-channel designs by enabling spatially organized co-culture of multiple cell types, closely recapitulating native tissue architectures. This configuration promotes physiologically relevant intercellular signaling, paracrine interactions, and precise control over the transport of nutrients, signaling molecules, and drugs, which are difficult to achieve in single-channel systems.[25] Multi-channel designs are particularly effective for modeling tissue–tissue interfaces, vascularized compartments, and complex barrier functions, thereby enhancing the predictive value for drug screening, disease modeling, and inflammatory or infection studies (Table 4).[27,105,188] Nevertheless, practical limitations, such as fabrication complexity, long-term co-culture stability, non-uniform perfusion, and restricted real-time monitoring, continue to hinder widespread adoption.[18,189] Selection of the appropriate multi-channel architecture should be guided by the specific biological question, balancing physiological relevance with engineering feasibility. Future developments integrating hybrid layouts, computational fluid dynamics-informed optimization, and advanced monitoring strategies are expected to further improve both functional fidelity and translational potential of multi-channel OoCs.

Heart-on-a-chip

The heart is one of the most vital yet least regenerative organs in the human body.[205] Cardiovascular diseases are

Table 3 Typical OoCs based on multi-channel microfluidic chips and their fabrication methods and materials, key microstructures, microfluidic channel parameters, fluidic conditions, and functional readouts

OoCs	Fabrication methods and materials	Key microstructures	Microfluidic chip	Fluidic and other conditions	Readouts	OoC functions	Ref.
Heart	Soft lithography (PDMS)	Micropillar arrays	Dual-channel chip lower channel: 300 μm, upper channel (cell): 600 μm, separated by micropillars	Flow rate: 20 μL min^{-1}, shear stresses 0.1–5 dyn cm^{-2}	Mechanical stretching (55–80 bpm); contraction amplitude 3.1 ± 0.4%; APD_{90} 300–450 ms; isoproterenol EC_{50} = 315 nM	Simulating *in vivo* blood circulation of cardiac tissue and the cardiac tissue response to drugs	21
	Soft lithography (PDMS/PMMA)	Micropillar arrays	Channel width: 300 μm, height: 150 μm and length: 10 mm	Shear stress: 0.1–5 dyn cm^{-2} electrical stimulation 1 Hz; mechanical stretching 10%, 1 Hz	ETH: 0.18–0.86 V cm^{-1}; APD_{90} 370 ± 40 ms, (280 ± 35 ms isoproterenol stimulation); Ca^{2+} oscillation period 1–1.25 Hz; (1.4–2.0 Hz isoproterenol stimulation)	Generating 3D cardiac micro-constructs and evaluating performances upon specific drug supplementation	190
	Soft lithography PDMS/PMMA	Hanging-drop porous networks	Chamber diameter: 3.5 mm, nutrient channel height: 200 μm, width: 200 μm	Flow rate: 0.5–8 μL min^{-1}	Contractile tension (0.9–14.4 mN mm^{-2}); APD_{90} (280 ms), Ca^{2+} oscillation period (1000 ms) isoproterenol increased beat rate; doxorubicin, DOX, induces cardiotoxicity	Simulating liquid circulations in a human physiological environment and evaluating the effects of isoproterenol on cardiac microtissues	191
Lungs	Soft lithography (PDMS)	Microporous membranes	Central channel width: 400 μm, height: 100 μm; air channel width, height: 200 μm; PDMS membrane thickness (10 μm), pore size (10 μm)	Flow rate: 30 μL min^{-1}	TEER (>800 Ω cm^2), permeability coefficient (fluorescent ALB 2.1% h^{-1} under ALI); inflammatory cytokines (ICAM-1 upregulation after TNF-α stimulation); pharmacological response (ROS increased 4× with 10% strain + silica nanoparticles)	Simulating the alveolar–capillary interface of the human lungs and evaluating the toxic and inflammatory effects of silica nanoparticles	20
	Soft lithography (PDMS)	Microporous membranes	Porous membrane thickness (3.5 or 10 μm), pore size (3 or 8 μm)	Flow rate: 10 μL min^{-1}, cyclic strain 10%, 0.2 Hz	Permeability coefficient (FITC–sodium +46%, RITC–dextran no change); inflammatory cytokines (pHPAECs IL-8 3.16 ng mL^{-1} per day); pharmacological response (FITC–sodium transport +46% under mechanical strain, 1.6% after 48 h)	Recreating the microenvironment of the lung parenchyma, including the mechanical stress induced by respiratory movements	2
	Soft lithography (PDMS) and injection molding (GelMA)	GelMA inverse opal porous membranes	Inverse opal: pore size 200 μm, thickness 550 μm	Cyclic strain (5–15%, 0.1–0.8 Hz)	Permeability coefficient (ZO-1 staining confirms tight junctions); inflammatory cytokines (cigarette smoke disrupts ZO-1); pharmacological response (10 μM remdesivir reduces 30% cell death)	Investigating the effects of smoking-related injuries and viral infections	102
Liver	3D bioprinting (PEVA, gelatin)	Microporous membranes	Upper channel: 600 μm height, lower channel: 300 μm height	Flow rate: 25 μL min^{-1} shear stress: 0.1–4 dyn cm^{-2}	Metabolic activity (CYP450 activity *e.g.*, CYP3A4, ALB 10–15 μg mL^{-1} per day, urea 50–100 μg mL^{-1} per day); inflammatory response (drug toxicity model: ALB −0.3 mg mL^{-1}, urea −0.15 nmol); pharmacological response (5 mM acetaminophen: Significant ALB decrease)	Investigating the effects of the biliary system on liver function-related gene expression and physiological functions	192

Table 3 *(continued)*

OoCs	Fabrication methods and materials	Key microstructures	Microfluidic chip	Fluidic and other conditions	Readouts	OoC functions	Ref.
	Soft lithography and laser ablation (PDMS and PMMA)	Micropillar arrays	Lower channel: 300 μm; upper channel: 600 μm	Flow rate: 50 μL min^{-1}	Metabolic activity (ALB 10–15 μg mL^{-1} per day, CYP3A4 100–200 RLU min^{-1} per 10^6 cells, urea 50–100 μg mL^{-1} per day); inflammatory response (Kupffer cells 1.2–1.8%); pharmacological response (acetaminophen APAP toxicity)	Simulating metabolic circuits within hepatic lobules and evaluating acute and chronic drug toxicity	33
Kidneys	Soft lithography (PDMS)	Microporous membranes	Upper channel: (width: 1000 μm, height: 1000 μm) Lower channel: (width: 1000 μm, height: 200 μm)	Urine channel 0.0007 dyn cm^{-2}, vascular channel 0.017 dyn cm^{-2}	VEGF-165 secretion: 0.006 ng mL^{-1}; clearance: inulin (7.5%), ALB (untreated 4%, ADR-treated 28%); ADR exposure induced barrier disruption and ALB leakage	Evaluating the potential of this method for nephrotoxicity screening, therapeutic development, regenerative medicine, and kidney disease research	193
	Soft lithography (PDMS) and electrospinning (silk fibroin)	Microporous silk fibroin and PDMS membranes	Upper channel height: 1000 μm, lower channel height: 200 μm	Flow rate: 1–4 μL min^{-1}	Clearance: inulin (7%), ALB (0.01–0.5%); urea removal: K_t/V = 1.8, URR = 83%; ADR exposure induced barrier disruption and ALB leakage; intercellular cross-talk: VEGF-A 14 ng mL^{-1} or 2.5 ng mL^{-1} in urinary or vascular channels	Reconstituting selective molecular filtration functions of healthy and diseased kidneys, recapitulating glomerular morphogenesis	194
	3D printing PDMS gasket	Perfusion channels separated by gelatin–fibrin ECM	1.8 mm upper channel (kidney organoid) and 0.7 mm lower channel (macrovessel)	Shear stress: 0.058 dyn cm^{-2} upper channel; 0.987 dyn cm^{-2} lower channel	Barrier function: dextran (70 kDa and 2 M Da) remains, dextran (10 kDa) species perfused through macrovessels; significant upregulation of renal functional genes (AQP1, SLC34A1, SLC12A1, and UMOD)	Supporting endothelial–organoid anastomosis and enabling vascularized perfusion mimicking glomerular microcirculation	112
Intestines	Soft lithography (PDMS)	Microporous membranes	Upper and lower channel height: 250 μm, width: 1.5 mm	Flow rate: 50–250 μL min^{-1}	Intestinal villus-like structures, regular and intact distribution of ZO-1 and VE-cadherin; distribution of MUC2-positive cells; barrier disruption after viral infection; virus infection induced CCL5, CXCL1, CXCL10, and CXCL11 upregulation	Recapitulating human-relevant intestinal pathophysiology induced by SARS-CoV-2 at the organ level	195
	DLP and soft lithography (resin and PDMS)	Micropillar arrays	Three parallel microchannels (500 μm wide, 10 mm long, 150 μm high) separated by micropillar arrays	Flow rate: 0.35 μL min^{-1}	Intestinal villus height 35–40 μm; TEER (60 Ω cm^2); LPS-induced TEER and villus height decreases, which can be suppressed by adding bacterial HY7715	Co-culture of human and microbial cells to mimic the gastrointestinal structure	196
	Soft lithography (PDMS) and CVD (CNFs)	Microporous membranes	Upper and lower channels (1000 μm wide, 5000 μm long, 800 μm high)	Flow rate: 100 μL h^{-1}	Permeability: FD20 (20 kDa) Papp: (2D 1.61 × 10^{-5} cm s^{-1}, 3D no flow 4.83 × 10^{-5} cm s^{-1}, 3D with flow 8.04 × 10^{-5} cm s^{-1})	Mimicking the structure and movement of real 3D intestine villi arrays	197

Table 3 *(continued)*

OoCs	Fabrication methods and materials	Key microstructures	Microfluidic chip	Fluidic and other conditions	Readouts	OoC functions	Ref.
Brain & BBB	Soft lithography (PDMS)	Microporous membranes	Upper channel width: 400 μm; lower center channel: 300 μm; side channels: 200 μm, height 100 μm	Flow rate: 16 μL min^{-1}, shear stress: 4 dyn cm^{-2}	TEER (150 Ω cm^2), permeability coefficient (4 kDa FITC–dextran: 2×10^{-6} cm s^{-1}; 40 kDa FITC–dextran: 0.5×10^{-6} cm s^{-1}); ZO-1, occludin, and VE-cadherin upregulation; inflammatory response IL-1β induced LCN2↑, VIM↑	Simulating the key structural and functional characteristics of the BBB and prescreening drug candidates for the treatment of neurological disorders	103
	TPP (resin)	Microporous channels	Capillary inner diameter: 50 μm, length: 1.1 mm.	Flow rate: 1.2–4700 μL min^{-1}; shear stress: 0.4–0.5 Pa	TEER: 75 ± 16 Ω cm^2; permeability: ~10^{-7} cm s^{-1}	Simulating a 1 : 1 scale, 3D-printed, realistic biohybrid model of the brain tumor microenvironment	198
Skin	Soft lithography (PDMS)	Microporous membranes	Cell chamber (8 mm) with lower channels (width: 200 μm, height: 150 μm) separated by PDMS membranes	Flow rate: 1 μL min^{-1}	TEER 4000–6000 Ω cm^2; permeability 10^{-7}–10^{-8} cm s^{-1}; TNF-α stimulation, IL-1β and IL-8 upregulated 3–10×	Developing drugs, testing cosmetics, studying skin biology, and reconstructing skin appendages	118
	Nylon-based template method (collagen hydrogel)	Perfusable vascular microchannels	Channel: 0.52 mm diameter	Flow rate: 2–3 mL h^{-1}	Formation of size-selective barriers (normalized permeated amount of ISDN was 3–4-fold higher than caffeine); capacitance 100–300 nF; cell density (3 times higher than non-perfused model)	Developing skin-equivalents containing vascular channels for studying vascular absorption	94
Dental and oral	Soft lithography (PDMS)	Micropillar arrays	Neuronal chamber dental pulp chamber connected *via* microgrooves (width 300 μm)	Shear stress: 0.02–0.08 dyn cm^{-2})	Stemness markers CD90: 1.76×; BMI1: 2.08×; NANOG: 11.04× (*vs.* 2D culture); gene expression DMP1: 2.5×, OSX: 3.0×	Replicates the dental pulp, supporting vascularization and innervation enabling more accurate drug evaluation for pulp regeneration	199
	Soft lithography (PDMS)	Micropillar arrays	Central gingival chamber, lateral channels and gingival sulcus channel	Flow rate: 7.8 μL h^{-1}	Diffusion characteristics 10 kDa dextran $t_{1/2}$: 41.86 s; 70 kDa dextran $t_{1/2}$: 78.30 s inflammatory response IL-6 secretion increase 2.5×	Replicates the gingival sulcus microenvironment supporting host–microbiome interactions, inflammatory responses	200
	CNC micromilling (PMMA)	PC track-etched porous membrane	Upper chamber (access port for test substances/moist air), middle central gingival culture chamber (diameter 7 mm, 0.4 cm^2 effective area), lower perfusion channel	Lower channel (media perfusion): 1.5 ± 0.1 μL min^{-1}; upper channel (mouth rinse simulation): 50 μL min^{-1}	Lidocaine HCl & articaine HCl: ulcer-on-chip shows ≈4-fold higher cumulative permeation *vs.* intact gingiva-on-chip (4.5 h perfusion); mass balance recovery: 90–110%	Recapitulates healthy/ulcerated gingival microenvironment; supports host–material interactions (oral-care product testing); enables transmucosal drug permeation assessment	201

Table 4 Comparative analysis of structural parameters, fluidic conditions, and functional readouts of single-channel or static OoCs and multi-channel OoCs

OoCs	Model type	Key structures	Shear stress	Functional readouts	Ref.
Heart	Single-channel or static model	2D PDMS substrates with 10–30 mm wells	No shear stress	Beating rate: 0.5–0.8 Hz, contractile tension: 8–20 mN mm^{-2}	16, 22
	Multi-channel dynamic system	Multi-channel chip with flexible PDMS membrane or micropillars enabling mechanical strain	0.1–5 dyn cm^{-2}	Beating rate: 0.92–1.33 Hz, contractile tension: 1–20 mN mm^{-2}, APD_{90}: 300–450 ms, conduction velocity: 10–25 cm s^{-1}, isoproterenol: EC_{50} = 315 nM	21
Liver	Multi-channel static system	Multi-layered system with HA, PV, and CV channels (or micropillar arrays)	No shear stress	ALB (0.6 μg per day), urea (360 μg per day), CYP1A2 (9000 RLU per day)	33–35, 192
	Multi-channel dynamic system	Multi-layered system with HA, PV, and CV channels (or micropillar arrays)	0.2–2 dyn cm^{-2}	ALB (>2 μg per day), urea (>600 μg per day), CYP1A2 (19 000 RLU per day)	33, 35
Lungs	Multi-channel static system	PDMS membrane (pore size: 3–8 μm)	No shear stress	TEER <600 Ω cm^2, permeability (3.5% h^{-1}, ALB), NP translocation rate (<0.2% h^{-1}), ROS generation (1.5×)	2, 20
	Multi-channel dynamic system	PDMS membrane (pore size: 3–8 μm) upon cyclic strain 5–15%, 0.2 Hz	0.1–2 dyn cm^{-2}	TEER >800 Ω cm^2, permeability 2.1% h^{-1}, (ALB), metabolic activity increased (1.20–25%), TNF-α induced ICAM-1 upregulation (5–10×), silica NP translocation (1% h^{-1}), ROS generation (4×)	2, 12, 20
Intestines	Multi-channel static model	Micropillar arrays	No shear stress	Height of the villi (14 μm); TEER 20 Ω cm^2; FD20 permeability 10^{-5} cm s^{-1}; disordered actin staining, weak ZO-1	196
	Multi-channel model	Micropillar arrays or microporous membranes (pore size 1 μm)	0.026–0.053 dyn cm^{-2}	Height of the villi (37 μm), TEER 60 Ω cm^2 (micropillar arrays) or 3500 Ω cm^2 (microporous membranes), permeability (1.46×10^{-7} cm s^{-1}), CYP3A4 activity increased 4×, IL-6 and IL-8 upregulated 2–8× (TNF-α stimulation)	196, 202
BBB	Multi-channel static system	Transwell model (pore size: 0.4 μm)	No shear stress	TEER 25–105 Ω cm^2, permeability 10^{-6} cm s^{-1}	98
	Multi-channel dynamic system	PC membranes (pore size: 0.4 μm) or micropillar arrays	0.4–4 dyn cm^{-2}	TEER 150–300 Ω cm^2, permeability 10^{-6}–10^{-7} cm s^{-1}	98, 103
Skin	Multi-channel static system	Transwell model (pore size: 0.4 μm)	No shear stress	TEER 800–3000 Ω cm^2, permeability >10^{-7}–10^{-8} cm s^{-1}	203
	Multi-channel dynamic system	PDMS membranes (pore size: 1 μm)	0.05–0.5 dyn cm^{-2}	TEER 4000–6000 Ω cm^2, permeability 10^{-8} cm s^{-1}, IL-1β and IL-8 upregulated 3–10× (TNF-α simulation)	118, 204

among the leading causes of death and disability globally, with studies predicting that by 2030, the prevalence of heart failure will reach 46%.[206] To enhance our understanding of heart diseases, the heart-on-a-chip system, an emerging field integrating multi-channel microfluidic chips to mimic heart microenvironments, has shown significant promise.[22] Single-channel cardiac models typically cultured cardiomyocytes on soft PDMS or hydrogel substrates without perfusion or mechanical stretching. For example, in 2011, Grosberg *et al.*[207] used muscular thin film technology to construct engineered ventricular muscle membranes, effectively quantifying the contractility of cardiac experimental tools for cardiac disease research and drug evaluation. However, these systems allowed limited spontaneous beating (0.5–0.8 Hz), and less aligned sarcomeres due to the absence of shear or strain.[22,207] In contrast, multi-channel heart-on-chips employ dual chambers or microgrooved PDMS membranes that permit controlled perfusion (1–50 μL min^{-1}) and cyclic strain (5–10%). This dynamic environment promotes synchronized contractions and enhanced sarcomere alignment (α-actinin, cTnT, Cx43), approaching native myocardium physiology (spontaneous beating 0.92–1.33 Hz).[21,22]

To address the high failure rate of animal models in drug discovery, Mathur *et al.*[21] developed a heart micro-physiological system based on human iPSCs (Fig. 4a), which mimicked myocardial alignment and vascular networks, enabling dynamic drug exposure in cardiac tissue. This multi-channel microfluidic device features a central cell chamber (100–200 μm wide) connected to two adjacent media channels (30–40 μm wide) *via* an array of 2 μm microchannels that function as endothelial-like barriers. Fabricated through a two-step photolithography process using SU-8 photoresist and PDMS, the system enables purely diffusive nutrient and drug transport to the cardiac tissue while protecting it from shear stress. The hiPSC-derived cardiomyocytes self-organized into an aligned, spontaneously beating 3D microtissue exhibiting physiological contraction rates (55–80 bpm). Pharmacological validation demonstrated dose-dependent responses to isoproterenol (EC_{50}: 315 nM) and verapamil (IC_{50}: 950 nM), with drug sensitivity profiles closely matching human tissue-scale data rather than

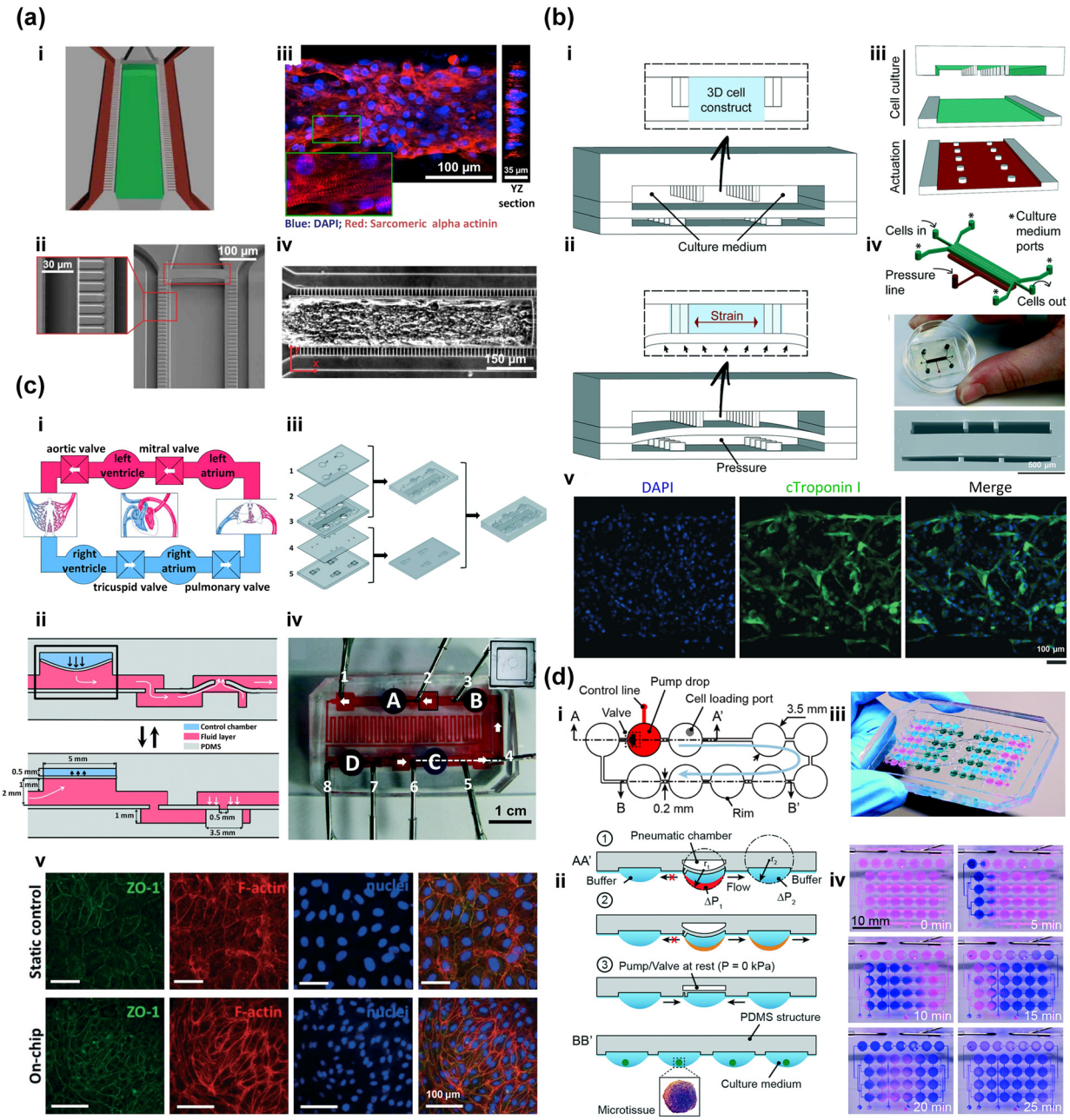

Fig. 4 Heart-on-a-chip platforms. (a) A cardiac microphysiological platform simulating the structure and function of human myocardial tissue for drug screening. i and ii) Design featuring a central cell chamber, two media channels, and connecting microchannels functioning as endothelial-like barriers to ensure purely diffusive transport and protect the tissue. iii and iv) Formation of aligned 3D tissue from human iPSC-derived cardiomyocytes within 24 hours, exhibiting spontaneous beating at physiological rates, adapted from ref. 21 with permission from Springer Nature, Mathur *et al.*, *Sci. Rep.*, 2015, **5**, 8883, Copyright ©2015. (b) A microfluidic platform simulating the native myocardial environment to study cardiomyocyte maturation and function. i–iv) Three-layer PDMS device with a central cell culture channel, side channels for medium perfusion, and a pneumatic system beneath for applying uniaxial strain. v) Immunofluorescence image showing human iPSC-derived cardiomyocytes cultured for 6 days, displaying mature cardiac morphology and enhanced electromechanical coupling, indicated by the expression of cardiac troponin I and functional junctions such as Cx43 and N-cadherin, adapted from ref. 190 with permission from The Royal Society of Chemistry, Marsano *et al.*, *Lab Chip*, 2016, **16**, 599–610, Copyright ©2016. (c) A platform simulating human systemic circulation for studying cardiovascular physiology and cell behaviours. i–iv) Microfluidic circulatory system with an on-chip pumping system comprising four solenoid-driven pumping units (A–D) and four check valves, representing ventricles and atria to ensure unidirectional flow. v) Immunofluorescence image showing HUVECs cultured under arterial-like flow for 8 hours, exhibiting enhanced and sparse ZO-1 distribution, indicative of appropriate mechanobiological responses, adapted from ref. 208 with permission from The Royal Society of Chemistry, Chen *et al.*, *Lab Chip*, 2017, **17**, 653–662, Copyright ©2017. (d) A platform simulating the heart's pumping function for studying compound effects on cardiac and other organ models. i–iii) Microfluidic loop with an integrated micropump, consisting of 10 drops (3 for pumping and 7 for tissue culture), which enables precise control of continuous and pulsatile flow. iv) Three-drop pump within a 24-drop array, demonstrating the capability for fluid circulation across larger networks for multi-tissue "body-on-a-chip" experiments, adapted from ref. 191 with permission from The Royal Society of Chemistry, Yazdi *et al.*, *Lab Chip*, 2015, **15**(21), 4138–4147, Copyright ©2015.

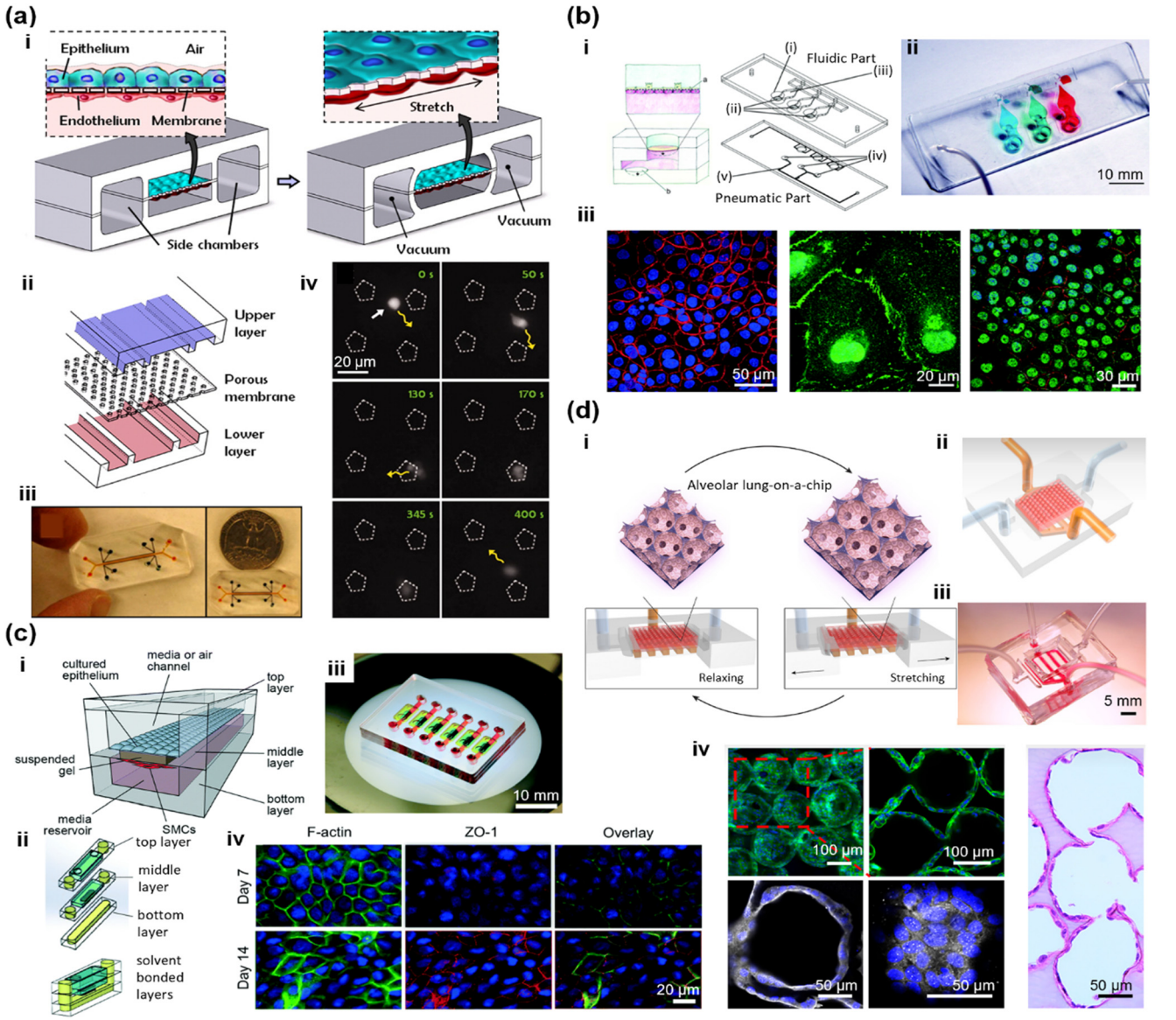

Fig. 5 Lung-on-a-chip platforms. (a) A platform simulating the alveolar–capillary interface for studying lung inflammation and nanoparticle effects. i–iii) Device featuring two microchannels separated by a thin, porous, flexible PDMS membrane coated with the ECM, with alveolar epithelial and endothelial cells cultured on opposite sides; vacuum-induced stretching mimics breathing movements, allowing independent fluid flow and nutrient delivery. iv) Time-lapse image showing neutrophil transmigration across the barrier, demonstrating the device's ability to replicate lung inflammatory responses, adapted from ref. 20 with permission from The American Association for the Advancement of Science, Huh *et al.*, *Science*, 2010, **328**(5986), 1662–1668 Copyright ©2010. (b) A platform simulating the pulmonary parenchymal environment, including the alveolar barrier and cyclic strain from breathing, for studying cellular responses and drug effects. i and ii) Lung-on-a-chip design comprising a fluidic part with three alveolar cell culture wells and a pneumatic part with micro-diaphragms, enabling precise cell seeding and mechanical strain control. iii) Immunofluorescence image demonstrating successful reconstruction of the alveolar barrier with enhanced cell–cell contacts, increased permeability, and elevated metabolic activity under cyclic strain, adapted from ref. 2 with permission from The Royal Society of Chemistry, Stucki *et al.*, *Lab Chip*, 2015, **15**, 1302–1310, Copyright ©2015. (c) A platform simulating the human lung airway microenvironment for studying chronic lung diseases and drug development. i–iii) Microdevice with three compartments (top airflow chamber, middle suspended hydrogel, and bottom media reservoir) fabricated from stacked PMMA layers with precise alignment and leak-free bonding. iv) Immunofluorescence image showing Calu-3 cells forming a stable monolayer with tight junctions (ZO-1) after 14 days of submerged culture, indicating the device's suitability for long-term ALI culture, adapted from ref. 214 with permission from The Royal Society of Chemistry, Humayun *et al.*, *Lab Chip*, 2018, **18**, 1298–1309, Copyright ©2018. (d) A platform simulating the human alveolar microenvironment for studying lung physiology and pathology. i–iii) Alveolar lung-on-a-chip model integrating a 3D GelMA inverse opal hydrogel structure with a PDMS chip, providing an ALI and cyclic mechanical motions to mimic breathing. iv) immunofluorescence image showing successful formation of a confluent alveolar epithelium with tight junctions and preservation of structural integrity after 14 days of culture, adapted from ref. 102 with permission from The Royal Society of Chemistry, Huang *et al.*, *Natl. Acad. Sci. U.S.A.*, 2021, **118**, e2016146118, Copyright ©2021.

conventional 2D cultures. This design effectively recapitulates key aspects of the human myocardial tissue architecture and drug exposure kinetics, providing a more predictive platform for cardiotoxicity screening. Similarly,

Marsano *et al.*[190] developed a microfluidic platform to generate mature and functional 3D cardiac microconstructs and assessed their performances upon specific drug supplementation (Fig. 4b). Auxiliary channels on this platform were positioned outside the culture chamber, allowing for the perfusion of the culture medium during the cultivation process. These channels provide biochemical stimuli and transmit pacing signals. Agarwal *et al.*[16] further employed semi-automated techniques to process soft elastic membrane cantilevers, increasing the throughput of pharmacological studies and opening new avenues for cardiac disease research. To reconstruct the complex human circulatory system *in vitro*, Chen *et al.*[208] developed an advanced multi-channel OoC platform to reconstitute the human circulatory system *in vitro* (Fig. 4c). The PDMS-based device was fabricated using multi-layer soft lithography, incorporating four independently controlled solenoid-driven pumping units (~2.5 μL per chamber) that mimic cardiac chambers, integrated with passive check valves to ensure unidirectional flow. The system employs a capillary-assisted pressure sensor (capillary inner diameter: 100 μm) for real-time pressure monitoring, achieving a high-resolution detection range of 0–142.5 mmHg with rapid response (<0.2 s). Biologically, the sophisticated multi-channel design and independent flow paths enabled the culture of human umbilical vein endothelial cells (HUVECs) under physiologically relevant pulsatile flow (21 dyn cm^{-2} shear stress) without interference from other physical parameters. Under arterial-like pressure profiles (115/69 mmHg systolic/diastolic), the cells exhibited significant morphological changes (shape index decreased from 0.59 to 0.49, $p < 0.001$) and enhanced ZO-1 tight junction protein expression. The platform successfully modeled cardiomyopathy-related hemodynamic conditions and evaluated catecholamine effects, demonstrating its capability to accurately recapitulate human cardiovascular pathophysiology for drug testing applications. The configurable hanging droplet networks designed by Yazdi *et al.*[191] synchronized with the heart tissue beating by controlling the pumping frequency (Fig. 4d), mimicked liquid circulations in a human physiological environment, and evaluated the effects of isoproterenol on cardiac microtissues.

Building upon these advances, researchers have further explored innovative microfluidic platform systems by integrating some new technologies to investigate specific disease mechanisms and organ–organ interactions. In recent years, Fu *et al.*[209] integrated biohybrid-colored hydrogels into microfluidic devices to develop a heart-on-a-chip with micro-physiological visualization for biological research and drug screening. Furthermore, Liu *et al.*[210] demonstrated a heart-on-a-chip integrated with extra- or intra-cellular bioelectronic devices that mimicked coronary occlusion followed by unblocking *via* microfluidic channels and cell culture areas. In some cases, it is critical to study the effects of acute hypoxia on cardiac function. For instance, breast cancer patients with cardiac dysfunction may have varying degrees of chemotherapy-induced cardiotoxicity (CIC). Lee *et al.*[55] proposed a model for investigating CIC, which induced cardiac tissue derived from human iPSCs to interact with breast cancer tissue on a dual-organ platform while monitoring multiple biomarkers secreted by the cells. The development of these technologies has provided new perspectives and tools for the study and treatment of heart diseases.

Lung-on-a-chip

The lungs are the primary organs of the human respiratory system, responsible for maintaining blood oxygen supply through pulmonary circulation and facilitating gas exchange across the alveolar-capillary network.[211] Lung diseases are among the leading causes of morbidity and mortality globally. The lung-on-a-chip[23] represents one of the most mature and physiologically validated OoC models, offering a quantitative platform for studying gas exchange, inflammation, and respiratory disease mechanisms. Static air–liquid interface (ALI) models provide limited air exposure and mechanical motion. They exhibit TEER less than 600 Ω cm^2 and higher permeability, indicative of a leaky barrier.[2,12,20] Multi-channel lung-on-chips typically integrate multiple channels separated by elastic PDMS membranes (10 μm thick, 3–8 μm pores) under cyclic strain (5–10%) and perfusion (0.1–2 dyn cm^{-2}). These conditions reproduce alveolar breathing mechanics, improving TEER to over 800 Ω cm^2, reducing permeability by 60–70%, and promoting epithelial–endothelial cytokine crosstalk, achieving greater IL-6/IL-8 secretion under inflammatory stimuli.[2,12,20]

To replicate the structural and mechanical characteristics of the lungs, particularly the dynamic interactions between tissues and the application of mechanical forces, Huh *et al.*[20] developed a biomimetic microsystem that mimicked the human alveolar–capillary interface (Fig. 5a). The device was fabricated using soft lithography with three bonded PDMS layers, incorporating two parallel microchannels separated by a thin (10 μm), porous, flexible PDMS membrane coated with ECMs. Human alveolar epithelial cells and pulmonary microvascular endothelial cells were cultured on opposite sides of the membrane under an air–liquid interface. Application of cyclic vacuum (10% strain, 0.2 Hz) to side chambers mimicked physiological breathing motions, inducing cell alignment and morphological changes. In nanotoxicology studies, silica nanoparticles (12 nm) induced reactive oxygen species production under mechanical strain, fourfold higher than static conditions, and promoted neutrophil adhesion and transmigration. The system also revealed a fourfold increase in nanoparticle translocation across the barrier under breathing-mimetic conditions, corroborated by *ex vivo* mouse lung studies. This integrated microdevice effectively recapitulates organ-level lung responses to mechanical and chemical stimuli, offering a

physiologically relevant platform for toxicology and drug screening. A similar biomimetic microstructure has also been used to develop a clinically relevant human disease model[212] for chemotherapy-induced pulmonary edema, enabling the identification of new therapies and reliable predictions of their *in vivo* efficacy and toxicity. Furthermore, this chip architecture has been applied to simulate other organs, such as the human intestinal model.[213]

Stucki *et al.*[2] developed a personalized lung cancer spheroid model for chemosensitivity assays (Fig. 5b). The device was fabricated *via* stereolithography using PDMS, featuring a symmetrical tree-like microchannel network (channel width: ~100 μm) that evenly distributes cells to eight round-bottom microwells (diameter: 0.5 mm) *via* hydrostatic pressure. This design enabled homogeneous spheroid formation from minimal cell inputs (as low as 1250 cells per channel). Primary lung adenocarcinoma epithelial cells (PLETCs) and pericytes (PCs) were co-cultured at a 5 : 1 ratio to mimic the tumor microenvironment. Under constant perfusion, co-culture spheroids exhibited significantly higher chemoresistance to cisplatin compared to monoculture spheroids, with peak apoptosis at 80 μM *versus* 16 μM, respectively. The system maintained high cell viability (<10.5% mortality over 8 days) and supported spheroid compaction and proliferation. This platform demonstrates robust replication of tumor–stroma interactions and drug response heterogeneity, highlighting its potential for personalized oncology applications. To investigate the role of interactions between airway epithelial cells (ECs) and smooth muscle cells in the pathogenesis of chronic lung diseases (CLDs), Humayun *et al.*[214] developed a thermoplastic-based microfluidic airway chip (Fig. 5c). This model featured three vertically stacked microfluidic chambers and simulated the lung airway microenvironment using polymeric membranes, particularly the interactions between SMCs, ECs, and the ECM. Benam *et al.*[215] also used this model to analyze human lung inflammation and drug responses. Huang *et al.*[102] proposed a human alveolar-related model to research the effects of smoking injuries and SARS-CoV-2 infection in the distal lung (Fig. 5d). This alveolar-lung chip platform consisted of a 3D porous membrane made of low-stiffness gelatin methacryloyl (GelMA), which had a trabecular structure that mimics human alveolar sacs. By integrating cyclic strain into the device, the system allowed for biomimetic breathing events. This array of models has advanced our ability to replicate human lung physiology, offering valuable tools for pathophysiological investigations and preclinical drug evaluation.

Liver-on-a-chip

The liver is the largest internal organ in the human body, distinguished by its complex microarchitecture and critical physiological functions, particularly in drug metabolism. Conventional *in vitro* liver models often struggle to maintain stable long-term hepatic functions and fail to fully replicate disease progression or drug-induced toxicity responses. Static liver models use hepatocyte monocultures under low or no flow, leading to rapid loss of polarity and reduced hepatic metabolism, albumin (ALB) <0.6 μg per day and urea (360 μg per day), and CYP activity <50% of multi-channel dynamic models.[33,35,216] In contrast, typical multi-channel liver-on-chips feature a multi-layered system with hepatic artery (HA), portal vein (PV), central vein (CV) channels, and cell-loading chambers, separated by a porous PET or PDMS membrane (5–20 μm thick, 0.4–3 μm pores) or micropillar arrays, supporting co-culture of hepatocytes, Kupffer cells, and LSECs. Controlled perfusion (0.2–2 dyn cm^{-2}) maintains the bile canaliculi structure and enhances metabolic performance, albumin (ALB) >2 μg per day, urea > 600 μg per day, and CYP activity approaching physiologically relevant levels.[33,35]

With the advancement of microfluidic engineering, researchers have developed a range of innovative liver-on-chips that more accurately replicate hepatic microenvironments and structural complexity. Lee *et al.*[192] utilized 3D cell printing technology to fabricate a liver-on-a-chip (Fig. 6a) with dual-fluid channels, consisting of two distinct, segregated flow paths: an upper vascular channel and a lower biliary channel. This model enables the co-culture of hepatocytes and the formation of functional bile duct structures, significantly enhancing liver-specific gene expression and metabolic activity. Mi *et al.*[217] constructed a dual-layer liver sinusoid chip that replicates *in vivo*-like permeability and promotes uniform distribution of endothelial cells. Ya *et al.*[33] designed a biomimetic liver lobule chip modeled as a six-layer hexagonal prism (Fig. 6b). The third and fourth layers incorporate circular platforms with through-holes, while the fifth layer includes an array of circular micropillars. Using a microfluidic strategy to guide angiogenesis, the culture medium flows at a controlled rate through the micropillar gaps, leading to the self-assembly of perfusable liver sinusoids. This setup mimics oxygen delivery and facilitates the formation of complex hepatic microstructures and evaluated acute and chronic drug toxicity. Zheng *et al.*[218] developed a 3D multicellular dynamic liver-on-a-chip utilizing a microporous membrane as the structural scaffold, which supports hepatocyte spheroid formation under continuous perfusion, closely mimicking the liver tissue microenvironment.

In recent years, these platforms have been increasingly applied to toxicological assessment and disease-specific liver studies. Du *et al.*[35] developed a liver model that reproduces both the morphological and metabolic characteristics of native liver tissue (Fig. 6c). The model successfully metabolized 5-fluorouracil and capecitabine, with drug metabolism efficiency dependent on the duration of culture. Frojdenfal *et al.*[220] designed a hexagonal liver lobule chip composed of three PDMS layers, capable of inducing lipid accumulation in hepatocytes, thereby establishing a more physiologically accurate model of NAFLD. Tian *et al.*[79] developed a liver sinusoid chip composed of three integrated

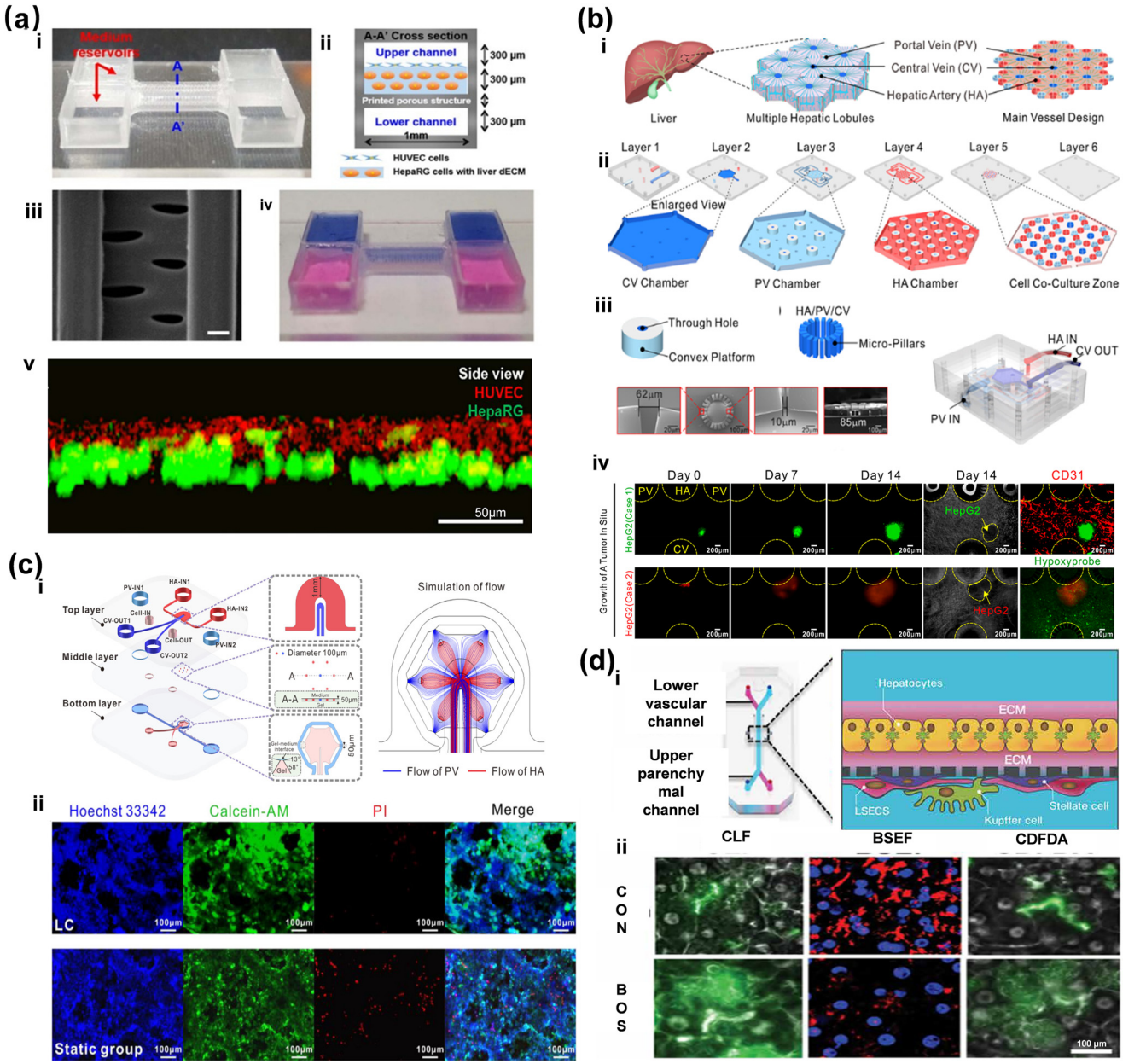

Fig. 6 Liver-on-a-chip platforms. (a) A platform simulating the liver microenvironment and biliary system for studying liver physiology and drug responses. i–iv) 3D liver-on-a-chip design featuring dual fluidic channels (i and iv) and a porous structure (iii) in the cross-sectional view (ii) for cell positioning and fluid separation, mimicking vascular and biliary functions. v) Confocal microscopy image obtained immediately after cell printing, showing accurate placement of green-labeled HepaRG cells and red-labeled HUVECs, with HUVECs positioned above the HepaRG cell-laden liver dECM bioink, adapted from ref. 192 with permission from IOP Publishing Ltd., Lee *et al.*, *Biofabrication*, 2019, **11**, 025001, Copyright ©2019. (b) A platform simulating the liver structure and function for studying drug toxicity and liver disease progression. i–iii) Design of the 3D liver chip featuring a six-layer structure with micropillar arrays guiding sinusoid formation and dual fluid channels (portal vein [PV] and hepatic artery [HA]) simulating the liver's dual blood supply. iv) Fluorescence image showing angiogenesis and hypoxia around implanted HepG2 cell clusters, demonstrating the chip's ability to simulate tumor growth *in situ* and study liver cancer progression, adapted from ref. 33 with permission from American Chemical Society, Ya *et al.*, *ACS Appl. Mater. Interfaces*, 2021, **13**, 32640–32652, Copyright ©2021. (c) A platform simulating the liver lobule structure and function for studying liver diseases. i) Detailed design consisting of three PDMS layers: a top layer with HA and central vein (CV) channels, a middle layer with micro-holes for HA and CV, and a bottom layer with a hexagonal cell culture zone and portal vein (PV) channels, enabling dual blood supply to mimic *in vivo* conditions. ii) Fluorescence microscopy image showing high cell viability for at least 7 days, with formation of HepaRG cell clusters, HHSEC vascular networks, and sparse LX2 cells, indicating successful liver lobule-like microtissue formation, adapted from ref. 35 with permission from Elsevier Ltd., Du *et al.*, *Acta Biomaterialia*, 2021, **134**, 228–239, Copyright ©2021. (d) A platform simulating the liver cell structure and physiological functions for studying liver-specific functions and drug-induced toxicities. i) Liver-on-a-chip design with a dual-channel structure, culturing hepatocytes above and non-parenchymal cells (LSECs, Kupffer cells, and stellate cells) below, allowing dynamic studies of cell-specific functions and interactions. ii) Fluorescence microscopy image showing that bosentan inhibits bile acid efflux, leading to intracellular accumulation of CLF, confirming the chip's ability to replicate human-specific mechanisms of drug-induced hepatotoxicity, adapted from ref. 219 with permission from the American Association for the Advancement of Science (AAAS), Jang *et al.*, *Sci. Transl. Med.*, 2019, 11, eaax5516, Copyright ©2019.

components: wells, a compartmentalized chip with microchannels, and pressure-sensitive adhesive tape. This system simulates the microanatomical structure and dynamic environment of the liver and was applied to assess drug-induced hepatotoxicity. Upon acetaminophen (APAP) exposure, the model detected changes in reactive oxygen species levels and albumin secretion, effectively recapitulating APAP-induced liver injury. Jang *et al.*[219] employed micro-engineered OoC technology to construct a system integrating primary human hepatocytes and sinusoidal endothelial cells across ECM-coated porous membranes (Fig. 6d), enabling the evaluation of species-specific liver toxicity and diverse phenotypic drug responses. These technological advancements offer novel insights and robust tools for liver disease modeling, personalized medicine, and comprehensive toxicity evaluation.[217]

Kidney-on-a-chip

The kidney is a vital yet highly complex organ composed of more than 16 specialized cell types, each fulfilling unique and essential physiological roles in filtration, reabsorption, and secretion.[221] The intricate interplay among these diverse cells presents considerable challenges for *in vitro* simulation. The kidney-on-a-chip system provides a microphysiological model for studying renal filtration, tubular reabsorption, and drug-induced nephrotoxicity. Static kidney chips or Transwell models of proximal tubular cells suffer from low polarization, with lower TEER and weak reabsorption capacity. In recent years, kidney-on-chips based on multi-channel microfluidics offer promising applications in the investigation of kidney pathophysiology, preclinical drug evaluation, and nephrotoxicity assessment by enabling the precise control of physical and chemical microenvironments, as well as dynamic fluid flow that closely mimics *in vivo* conditions.[222]

To study the physiology and drug responses of the proximal tubule, Homan *et al.*[223] engineered a perfusable 3D proximal tubule-on-a-chip composed of human proximal tubule epithelial cells. This system successfully replicated the structure and function of native renal tubules, providing a reliable platform for drug screening and nephrotoxicity testing. The glomerulus, serving as the functional cornerstone of the kidney, constitutes a pivotal target for advancements in therapeutic interventions. Roye *et al.*[193] further advanced the concept by developing a patient-specific kidney-on-a-chip (Fig. 7a) utilizing VECs and mesodermal cells differentiated from a single donor's iPSCs. Their PDMS-based microfluidic chip effectively reproduced the glomerular microenvironment through tailored channel geometry, a porous membrane, and controlled incubation conditions, replicating critical features such as cell monolayer formation, endothelial–mesodermal crosstalk, VEGF-A signaling, and filtration dynamics. The kidney-on-a-chip evaluates the effects of the chemotherapeutic agent adriamycin on the glomerular structure and function. Similarly, Mou *et al.*[194] constructed a glomerulus kidney-on-a-chip system (Fig. 7b) using an electro-spun silk fibroin membrane. This chip comprised two fluidic channels, mimicking glomerular morphogenesis and barrier function. It effectively supported the differentiation and propagation of human iPSCs and achieved selective molecular filtration, serving as a dynamic platform for kidney research. For the purpose of achieving applicability in high-throughput drug testing or therapeutic uses, Kroll *et al.*[112] developed a perfusable, vascularized kidney-on-a-chip (Fig. 7c) with two separate channels. In this model, kidney organoids and human umbilical vein endothelial cells were respectively seeded in the two channels, with the vein endothelial cells forming a confluent endothelium. This structured setup allowed for the migration of endothelial cells present within the kidney organoids through the ECM towards the macrovessel, achieving micro-vessel integration. Furthermore, it enabled the transport of fluorescently labeled dextran of varying molecular weight and red blood cells from the macrovessel through the microvascular network to the glomerular epithelia within the kidney organoids, thus providing a novel and physiologically relevant route for drug delivery and evaluation. To mimic the glomerular internal environment, Musah *et al.*[39] constructed a dual-channel chip separated by a porous membrane, enabling the co-culture of human iPSC-derived podocytes and VECs (Fig. 7d). This model reconstructed the glomerular filtration barrier and evaluated the potential of this method for nephrotoxicity screening, therapeutic development, regenerative medicine, and mechanistic studies of kidney development and disease.

Intestine-on-a-chip

The intestinal tissue encompasses a diverse array of cell types and harbors a rich and complex microbial community, serving as a crucial immunological barrier within the human body.[224] Static intestinal models have long served as the foundation for intestinal epithelial studies but present fundamental structural and physiological limitations,[29] yielding weak tight junctions, high permeability, and limited metabolic activity (low CYP3A4).[30,225] Multi-channel intestine-on-chips typically employ stacked channels separated by a 10 μm porous membrane with 0.4 μm pores, perfused at 0.02–0.06 dyn cm^{-2} and coupled with peristaltic strain. These dynamic stimuli induce key physiological hallmarks of the intestine, including villus morphogenesis, mucus secretion (MUC2+), and increased barrier integrity (TEER). The elevated expression of the metabolic enzyme CYP3A4 further indicates a more *in vivo*-like state, thereby enhancing the model's predictive power for drug absorption.[30,225] Wu *et al.*[202] developed an intelligent intestine-on-a-chip integrated with machine learning algorithms (Fig. 8a). Through the construction of a 16-channel microfluidic chip equipped with PC porous membranes, combined with an anaerobic environment control system, an intelligent intestine-on-a-chip integrated with machine learning is developed to screen *Bifidobacterium longum* 3–14 as a relief-enteritis functional

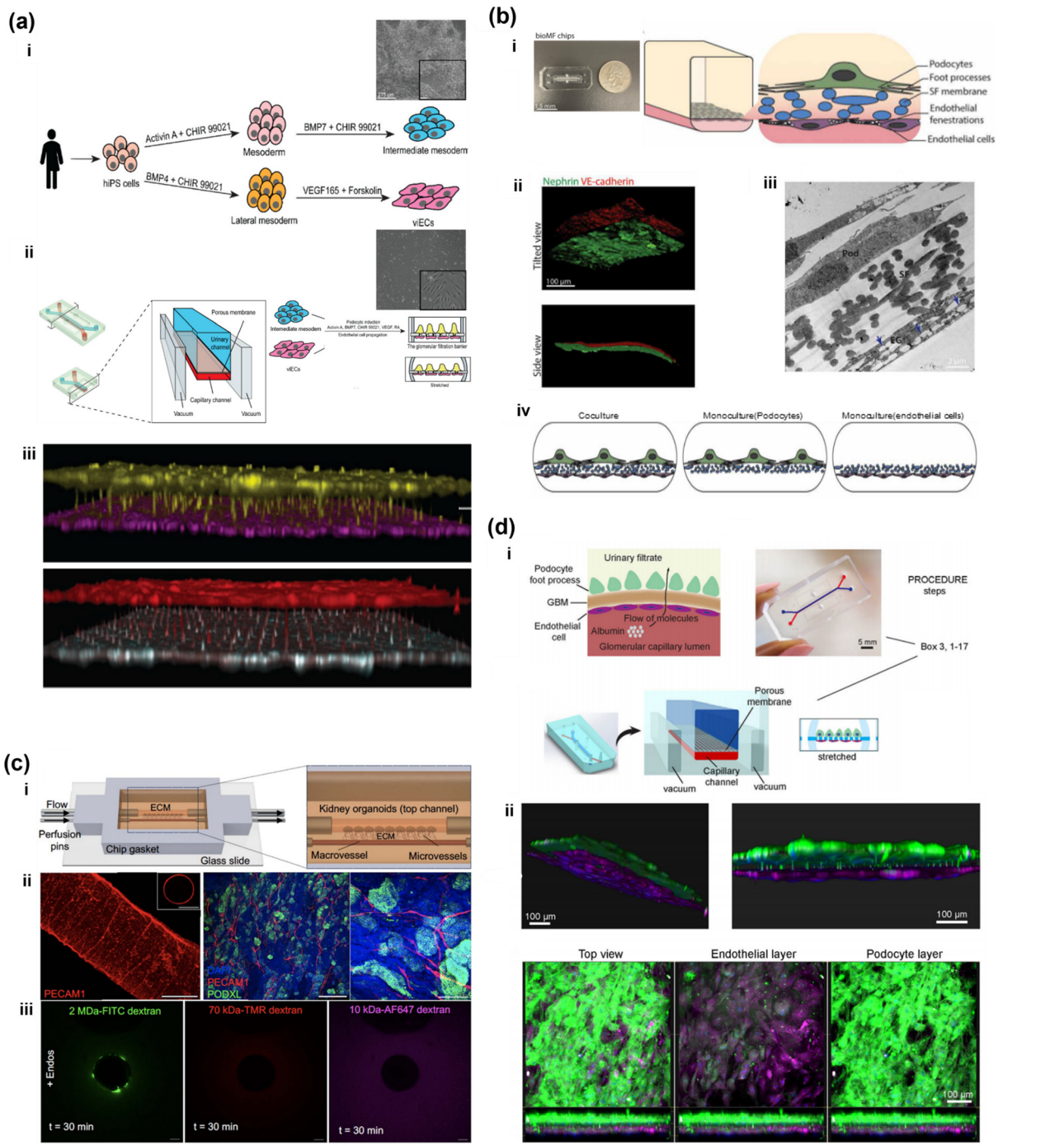

Fig. 7 Kidney-on-a-chip platforms. (a) A platform simulating the human kidney glomerulus for studying kidney disease mechanisms and drug effects. i and ii) Glomerulus chip design featuring two fluidic channels separated by a porous membrane, mimicking the urinary and capillary spaces. iii) Confocal microscopy image showing podocytes extending processes through the membrane to interact with endothelial cells, indicating successful formation of a functional filtration barrier, adapted from ref. 193 with permission from Multidisciplinary Digital Publishing Institute, Roye *et al.*, *Micromachines*, 2021, **12**, 967, Copyright ©2021. (b) A platform simulating the human kidney glomerulus for studying kidney function and disease. i) Chip design with two parallel microfluidic channels separated by an ultrathin silk fibroin membrane. ii) Confocal image showing distinct layers of podocytes and endothelial cells on opposite sides of the membrane. iii) TEM image showing fenestrations in endothelial cells, indicating functional glomerular filtration. iv) Immunofluorescence image revealing VEGF-A signaling between podocytes and endothelial cells, supporting tissue-specific morphogenesis (scale bar, 2 μm), adapted from ref. 194 with permission from American Association for the Advancement of Science, Mou *et al.*, *Sci. Adv.*, 2024, **10**, eadn2689, Copyright ©2024. (c) A platform simulating the kidney's native microenvironment for studying nephrotoxicity and disease mechanisms. i) Kidney-on-a-chip design featuring two channels embedded in the ECM for organoids and endothelial cells. ii and iii) Immunofluorescence images confirming endothelial layer formation, organoid fusion with microvessels, and selective barrier function of the macrovessel (scale bar, 100 μm), adapted from ref. 112 with permission from IOP Publishing Ltd., Kroll *et al.*, *Biofabrication*, 2024, **16**, 045003, Copyright ©2024. (d) A platform simulating the human kidney glomerular capillary wall for studying kidney development and disease. i) Glomerulus chip's two-channel design with a porous PDMS membrane separating urinary and capillary compartments. ii) Confocal fluorescence image showing successful co-culture of podocytes and endothelial cells, with selective filtration of molecules like albumin and inulin, indicating functional glomerular mimicry, adapted from ref. 39 with permission from Springer Nature, Musah *et al.*, *Nat. Protoc.*, 2018, **13**, 1662–1685, Copyright ©2018.

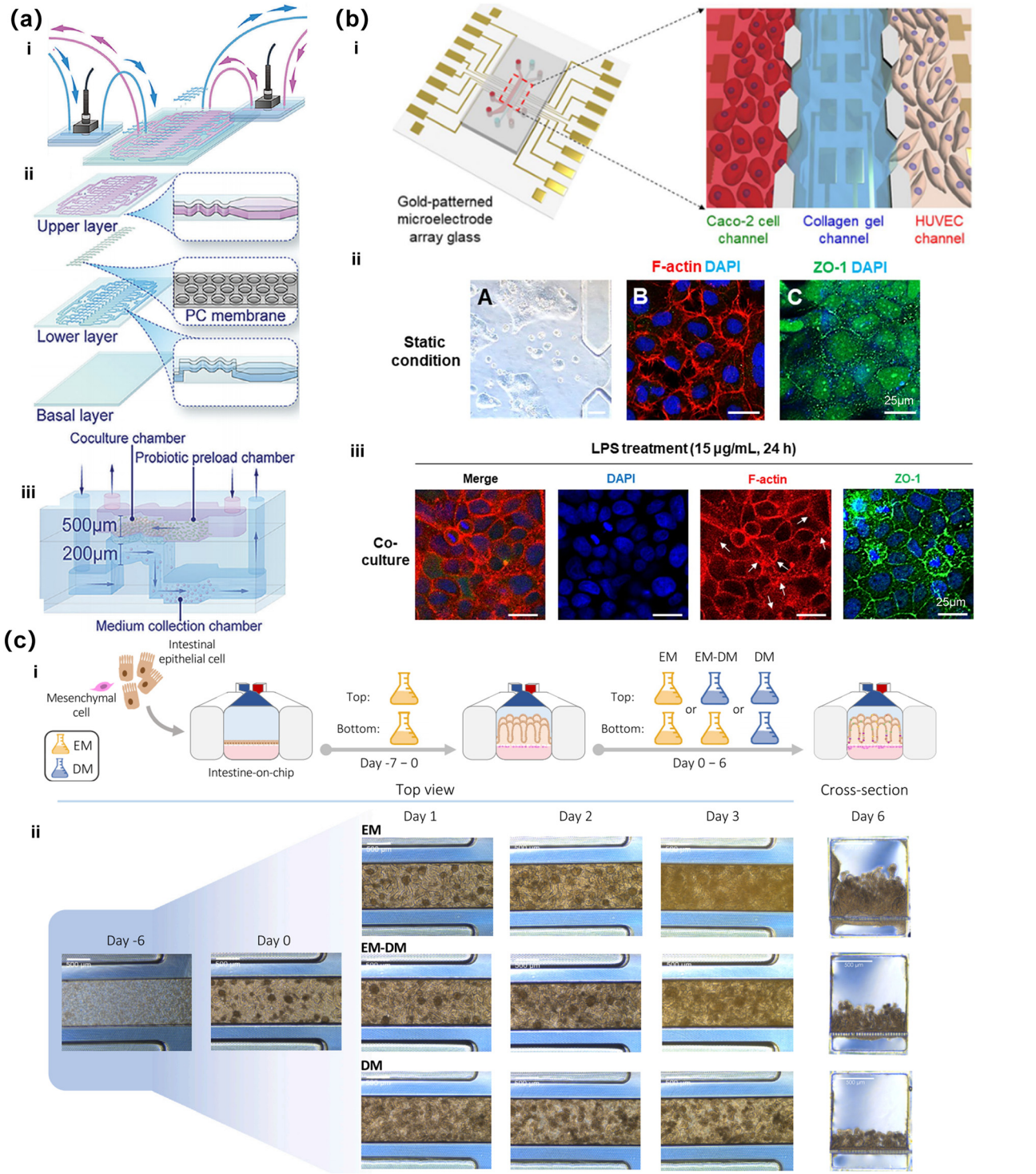

Fig. 8 Intestine-on-a-chip platforms. (a) A platform simulating the human intestinal microenvironment for studying interactions between probiotics and intestinal cells. i and ii) 16-channel microfluidic chip featuring a three-layer PDMS structure, with upper microchannels for cell seeding and probiotic storage, lower dual-sided channels for medium perfusion, and flexible porous membranes for coculture, iii) the multi-chamber design of the chip, adapted from ref. 202 with permission from Wiley-VCH GmbH, Wu *et al.*, *Adv. Mater.*, 2024, **36**, 2408485, Copyright ©2024. (b) A platform simulating the human intestinal environment for studying host–microbiome interactions and intestinal diseases. i) Three-channel design with collagen gel separating epithelial and endothelial cell cultures. ii) Immunofluorescence image showing enhanced cell differentiation and barrier integrity under fluid flow. iii) Confocal fluorescence image revealing intestinal barrier damage and inflammation induced by LPS (scale bar, 25 μm), adapted from ref. 196 with permission from Springer Nature, Jeon *et al.*, *Nano Convergence*, 2022, **9**(8), 1–13, Copyright ©2022. (c) A platform simulating the small intestinal barrier for studying cell interactions and disease mechanisms. i) Intestine-on-a-chip design featuring two channels separated by a porous membrane. ii) Brightfield images showing tissue self-organizing into villus-like folds, with different media conditions affecting tissue height and cell density, indicating balanced proliferation and differentiation under EM–DM conditions, adapted from ref. 227 with permission from Elsevier Inc., Moerkens *et al.*, *Cell Rep.*, 2024, **43**, 114247, Copyright ©2024.

probiotic. Kim *et al.*[42] devised an intestine-on-a-chip that simulates the cyclic strain associated with physiological peristaltic motion, thereby reconstructing key aspects of the intestinal microenvironment. This model replicated various dynamic physical and functional characteristics of the intestine, accurately mimicking the mechanical forces, structural features, absorptive capabilities, transport processes, and pathophysiological interactions of the intestine along with its essential microbial symbionts. It holds significant potential for accelerating drug development processes.[213,226]

Jeon *et al.*[196] proposed a novel microfluidic-based intestine-on-a-chip with microelectrode arrays (Fig. 8b), allowing fluid to flow through the microchannel at a low rate (21 μL h^{-1}) to reconstruct the intestinal microenvironment and mimicking the stable fluidic flow of the intestinal lumen. This provides a novel platform for in-depth exploration of the interaction between the intestinal microbiome and host cells. In order to resemble the conditions along the crypt–villus axis in the intestine, Moerkens *et al.*[227] successfully constructed a sophisticated dual-channel intestine-on-chip (Fig. 8c) using human iPSC differentiation techniques. Within this model, the apical channel meticulously replicated the microenvironment of intestinal contents, housing a spectrum of intestinal epithelial cell types derived from human iPSCs. Conversely, the basal channel harbored a constellation of mesenchymal cells, neurons, and potential glial cells, collectively recapitulating the intestine's intricate physiological architecture and barrier functionality. This innovative platform offers insights into the study of intestinal physiology and pathophysiology. Similarly, Jang *et al.*[197] created a 3D *in vitro* intestinal microvilli OoC, featuring an array of carbon nanofiber bundles, which accurately mimicked the functional and physical activities of the intestine for drug screening purposes. These models enhance intestinal physiology replication, aiding disease research and drug testing.

Brain & BBB-on-a-chip

The brain is one of the most complex and functionally diverse organs, responsible for sensation, cognition, emotion, and motor control. Traditional neuroscience research is limited by ethical concerns, species differences in animal models, and difficulties in replicating the brain's 3D structure and microenvironment *in vitro*.[228] To overcome these challenges, brain-on-a-chip technologies have emerged, enabling the co-culture of various brain cell types, such as neurons, astrocytes, and oligodendrocytes, under dynamic conditions. Static brain or BBB models produce tight junctions but limited physiological performance, with low barrier integrity and high permeability. In contrast, multi-channel brain-on-chips have integrated endothelial, astrocytic, and pericyte layers separated by a porous membrane (0.4–8 μm pores), perfused at 2–4 dyn cm^{-2}. These dynamic conditions elevate TEER to 150–250 Ω cm^2 and lower permeability (10^{-7}–10^{-8} cm s^{-1}), achieving enhanced barrier selectivity.[19,103,104]

Generally, these brain-on-a-chip platforms can be categorized into two types: one designed for simulating peripheral neuronal circuits[229] and the other focused on neurotransmission and disease modeling in CNS tissues.[104,230,231]

To mimic peripheral neural circuits, researchers have developed multi-channel microfluidic systems that support the co-culture of spatially distinct neuronal populations and promote intercellular communication through defined pathways. For instance, Vysokov *et al.*[232] developed a three-compartment microfluidic system for co-culturing DRG and DH neurons, with interconnecting channels that mimic the peripheral pain pathway. The device allows independent microenvironmental control for drug testing and axotomy to investigate neuronal and synaptic responses to axonal injury. Johnson *et al.*[229] fabricated a 3D-printed neural circuit platform comprising microfluidic channels and compartmentalized chambers (Fig. 9a). In this system, the microchannels guide axonal pathfinding, while the chambers facilitate cell isolation and spatial organization, together forming an effective *in vitro* model for investigating the significantly enhanced chemotactic response of human neural progenitors to shallow gradients of CXCL12.

With the expanding scope of brain-on-a-chip technologies, growing research efforts have been directed toward recapitulating complex CNS tissue functions and elucidating the mechanisms underlying neurological disease progression. Focusing on *in vitro* culture and research of whole brain tissues, Park *et al.*[231] introduced a CNS chip (Fig. 9b) integrating concave micropore arrays and an osmotic micropump system *via* soft lithography, enabling the formation of uniform neurospheres that replicate the 3D structure of brain tissue. The platform also supports slow interstitial flow, mimicking *in vivo* nutrient transport and waste clearance, thus offering an effective model for investigating Alzheimer's disease and neurodegenerative conditions. More recently, Wang *et al.*[104] developed a PDMS-based microfluidic chip (Fig. 9c) fabricated *via* soft lithography, integrating dual brain organoid culture chambers and trapezoidal pillar-arrayed medium channels for dynamic perfusion, enabling the study of prenatal nicotine exposure (PNE)-induced neurodevelopmental disorders and revealing aberrant neuronal differentiation, disrupted brain regionalization, and impaired cortical development in organoids. This platform facilitates precise spatiotemporal regulation of nutrient and drug delivery, and has been applied to model prenatal nicotine exposure, providing insights into mechanisms of neurodevelopmental toxicity.

In addition to extensive efforts in simulating the peripheral and central nervous systems using brain-on-a-chip technologies, increasing attention has been directed toward the BBB, which plays a vital intermediary role by regulating molecular exchange between the systemic circulation and the

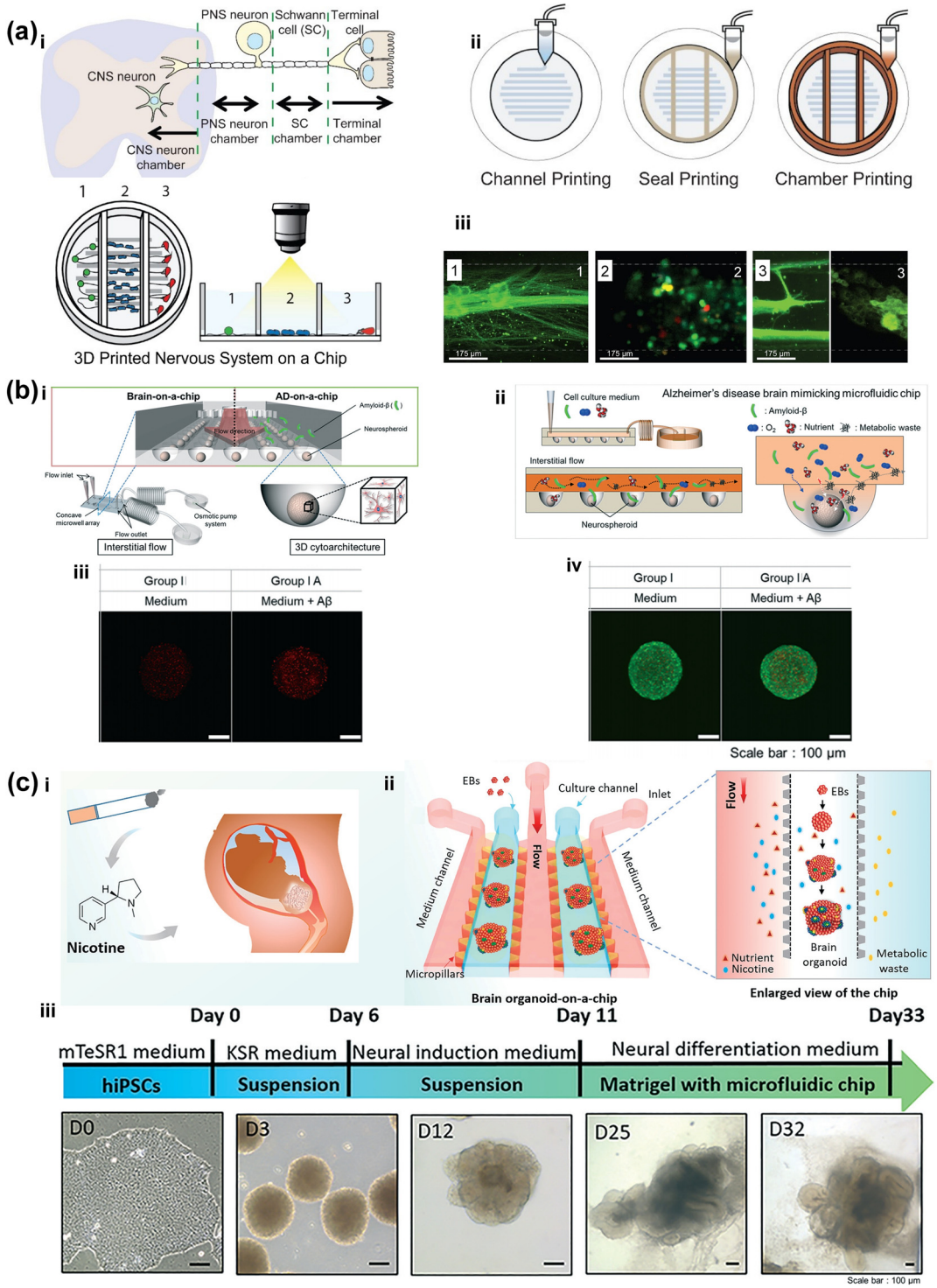

Fig. 9 Brain-on-a-chip platforms. (a) A platform simulating the nervous system for studying viral infections and cellular interactions. i and ii) 3DNSC design featuring microchannels for axonal alignment and compartmented chambers for cell isolation. iii) Fluorescence images showing Schwann cells associated with axons and spatial separation of cell types, indicating effective biomimicry of neural interactions, adapted from ref. 229 with permission from The Royal Society of Chemistry, Johnson *et al.*, (2015). *Lab Chip*, **16**, 1393–1400, Copyright ©2015. (b) A platform simulating the brain's 3D cytoarchitecture and interstitial flow for studying neurodegenerative diseases and drug screening. i and ii) Brain-on-a-chip design with concave microwells and an osmotic micropump enabling continuous flow. iii and iv) Immunostaining images showing enhanced neural differentiation and network formation under flow, and greater amyloid-β-induced damage under dynamic conditions, indicating the chip's potential for disease modeling and toxicity testing, adapted from ref. 231 with permission from The Royal Society of Chemistry, Park *et al.*, *Lab Chip*, 2014, **14**, 1–8, Copyright ©2014. (c) A platform simulating early human brain development for studying the effects of prenatal nicotine exposure. i and ii) Brain organoid-on-a-chip design with two culture chambers separated by a central channel for fluid flow. iii) Brightfield images showing embryoid bodies self-organizing into neuroepithelial spheroids, indicating successful neural differentiation and brain organoid formation, adapted from ref. 104 with permission from The Royal Society of Chemistry, Qin *et al.*, *Lab Chip*, 2018, **18**, 851–860, Copyright ©2018.

CNS. The BBB chip is a highly selective and dynamic physiological interface composed of endothelial cells connected *via* tight junctions, astrocytic end feet, and pericytes. It mediates both passive diffusion and active transport, ensuring CNS homeostasis. Conventional *in vitro* BBB models, typically based on 2D monocultures, lack the structural and functional complexity of the native barrier. In contrast, BBB-on-chips allow precise control of multiple cell types in 3D configurations, enabling the construction of physiologically relevant vascular structures. Current BBB chips mainly fall into three structural categories: the planar multi-channel multi-fluidic structures,[233] 3D layered structures,[98,103] and cylindrical structures.[158,198]

The planar multi-channel microfluidic chip exhibits high precision in regulating medium flow, enabling the delivery of nutrients and oxygen through independent channels, thereby supporting complex co-culture systems and real-time cellular monitoring. Based on this design, Shin *et al.*[233] developed a human BBB chip integrating a 3D astrocyte culture with a layered channel structure (Fig. 10a). The chip consists of upper vascular and lower perivascular layers, incorporating endothelial cells, perivascular cells, and astrocytes, thereby closely mimicking the BBB structure and function. This platform enables quantitative analysis of cell interactions, permeability, and gene expression, and facilitates evaluation of nanoparticle distribution and cellular uptake within vascular and perivascular regions.

Multilayer microfluidic structures offer an evolution of the planar design by enabling closer spatial arrangement of different cell types, thereby promoting enhanced cellular communication and more physiologically representative co-culture conditions. These systems enable independent modulation of layer-specific environments. Ahn *et al.*[103] developed a human BBB-on-a-chip that recapitulates the essential structure and function of the neurovascular unit (Fig. 10b). The PDMS-based device was fabricated using soft lithography and features a multi-layered architecture, comprising an upper vascular channel (400 μm wide, 100 μm high) and a lower perivascular compartment consisting of three parallel channels separated by micropillars. This model demonstrated significant physiological relevance, as the tri-culture of human brain microvascular endothelial cells (HBMECs), human brain vascular pericytes (HBVPs), and human astrocytes (HAs) under physiological shear stress (4 dyne cm^{-2}) enhanced the expression of BBB-specific genes (*e.g.*, ZO-1, GLUT1, LRP1) and achieved a low permeability coefficient ($\sim 1.5 \times 10^{-7}$ cm s^{-1} for 4 kDa FITC-dextran). A key advance was the establishment of a 3D astrocytic network exhibiting polarized aquaporin-4 (AQP4) distribution alongside reduced markers of reactive gliosis (*e.g.*, downregulation of LCN2 in 3D *versus* 2D cultures), enabling modeling of neuroinflammation upon IL-1β stimulation. The platform uniquely allows for 3D mapping of nanoparticle transport (*e.g.*, HDL-mimetics), and through precise sampling and FACS analysis,it revealed transcytosis mechanisms mediated by the SR-B1 receptor. In contrast to earlier BBB models relying on simple 3D co-cultures, this system employs a multi-channel design that effectively balances cellular compartmentalization with intercellular crosstalk. It thus provides superior reconstitution of astrocyte physiology, polarized AQP4 localization, and quantitative analysis of molecular trafficking at cellular resolution, offering a robust tool for studying central nervous system drug delivery.

In parallel, cylindrical BBB chip designs have emerged as a strategy to more accurately replicate the spatial architecture and dynamic flow of cerebral vasculature. Tricinci *et al.*[198] employed TPP to create an innovative 1 : 1 scale 3D biohybrid model of the brain tumor microenvironment (Fig. 10c). This platform featured a capillary-like microfluidic channel with co-cultured endothelial and astrocyte cells on the inner surfaces, forming a biomimetic barrier. The system employed micro-pumping technology to simulate *in vivo* fluid dynamics and assess drug diffusion across the BBB, as well as the efficacy of magnetically guided tumor spheroid therapy. Additionally, the platform demonstrated excellent compatibility, allowing seamless integration with other experimental techniques or models, thus expanding its applications in multidisciplinary research. Similarly, Seo *et al.*[158] developed a physiologically relevant triculture blood–brain barrier–glioblastoma (BBB–GBM) model using a soft-lithography-fabricated PDMS microfluidic device (Fig. 10d). The device features a three-layer architecture, with a central chamber (4.5 × 10.5 mm) containing a cylindrical vascular channel (580 μm) formed by removable microneedles within a type I collagen hydrogel. The BBB was constituted by coculturing human brain microvascular endothelial cells, human astrocytes, and human brain vascular pericytes, while patient-derived GBM spheroids were embedded in the collagen matrix at a controlled distance from the vasculature. The triculture BBB exhibited superior barrier functionality, as evidenced by low permeability coefficients and enhanced expression of junctional proteins and transporters—with ZO-1 and claudin-5 expression levels increased by 1.3-fold and 1.2-fold, respectively, compared to biculture controls.[158] Crucially, GBM spheroids in the coculture system exhibited heightened chemoresistance, with a 58.3-fold increase in the EC_{50} value for vincristine compared to monoculture, thereby replicating clinical drug resistance patterns. Compared to conventional Transwell or pillar-based array models, this platform utilizes removable microneedles to achieve a fully enclosed, continuous 3D cylindrical vascular structure. This design supports comprehensive, direct tumor–vessel interactions and provides an advanced solution for the formation of intact tubular networks and real-time assessment of transendothelial nanoparticle delivery.

Skin-on-a-chip

The skin, the largest organ of the human body, consists primarily of the stratum corneum and dermis, playing a crucial role in barrier protection, immune defense, and thermoregulation.[203] Static skin equivalents at the air–liquid

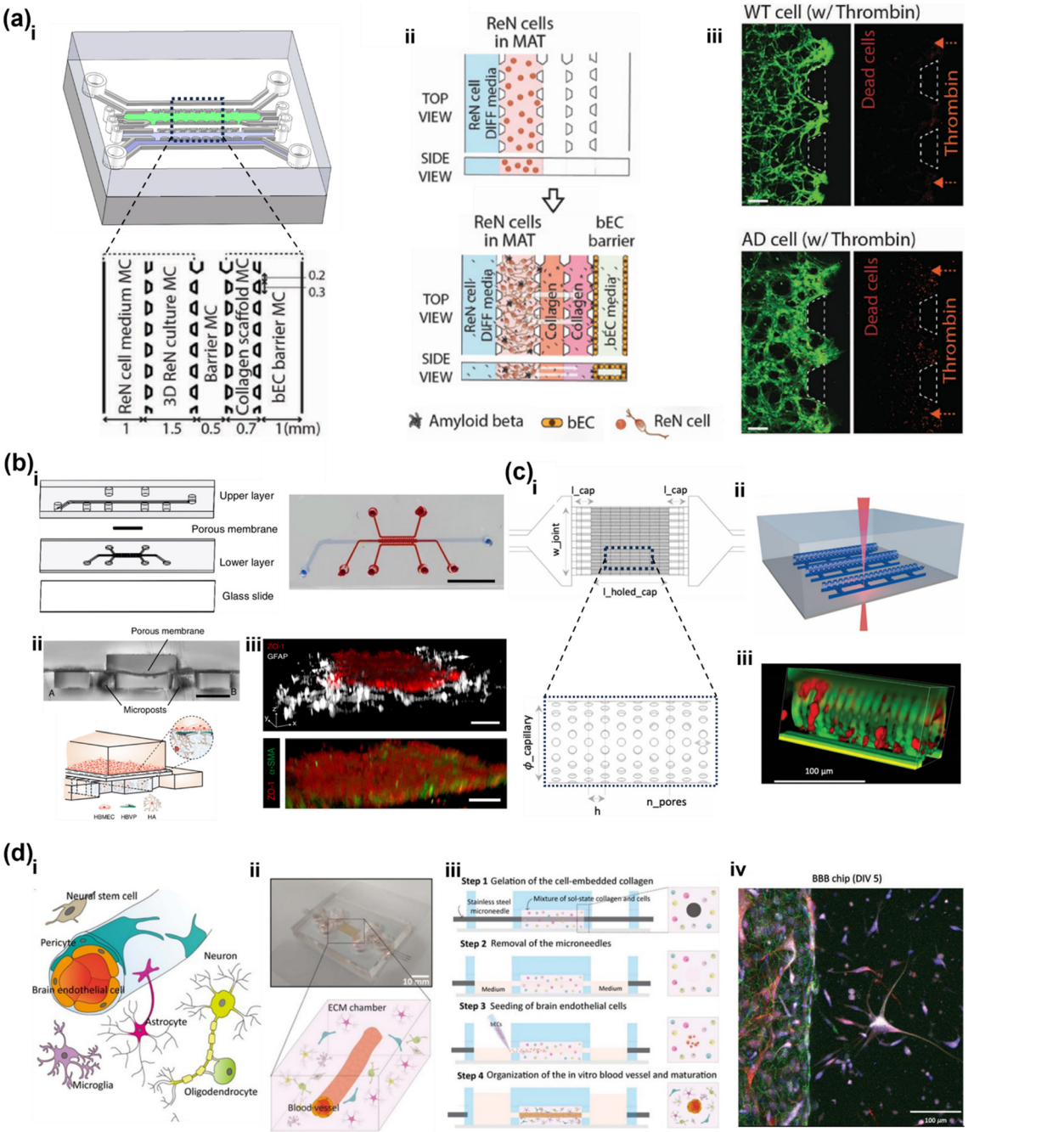

Fig. 10 BBB-on-a-chip platforms. (a) A platform simulating BBB dysfunction in Alzheimer's disease for studying BBB permeability and drug screening. i and ii) Microfluidic chip design featuring a 3D neural cell chamber and a BBB chamber separated by a barrier microchannel. iii) Fluorescence image showing increased cell death (red) in the AD model after thrombin treatment, indicating that BBB integrity is crucial for preventing neurotoxin-induced cell death, adapted from ref. 233 with permission from WILEY-VCH Verlag GmbH & Co. KGaA, Weinheim, Shin *et al.*, *Adv. Sci.*, 2019, **6**, 1900962, Copyright ©2019. (b) A platform simulating the human BBB for studying nanoparticle transport and BBB integrity. i and ii) BBB-on-a-chip design featuring upper and lower layers separated by a porous membrane, with micropillars stabilizing the 3D hydrogel environment. iii) Fluorescence images showing a tight endothelial monolayer and polarized AQP4 expression in astrocytic end-feet, indicating successful reconstruction of the BBB structure and function, adapted from ref. 103 with permission from Springer Nature, Ahn *et al.*, *Nat. Commun.*, 2020, **11**, 175, Copyright ©2020. (c) A biomimetic microfluidic platform recapitulating the glioblastoma microenvironment and BBB for investigating tumor–stroma crosstalk and nanoparticle-mediated drug delivery. i and ii) BBB chip design featuring an array of porous microtubes mimicking brain capillaries. iii) 3D reconstruction of endothelial cells forming a biohybrid barrier inside the microtubes, indicating successful barrier formation, adapted from ref. 198 with permission from Wiley-VCH GmbH, Tricinci *et al.*, Adv. Mater. Technol., 2020, **5**, 2000540, Copyright ©2020. (d) A platform simulating the *in vivo* BBB for studying brain tumor interactions and drug delivery. The BBB chip features a 3D hydrogel matrix with endothelial cells, pericytes, and astrocytes forming a triculture model. iv) Fluorescence image showing successful integration of these cells, with specific markers indicating the formation of a functional BBB structure, adapted from ref. 158 with permission from Wiley-VCH GmbH, Seo *et al.*, *Adv. Funct. Mater.*, 2021, **32**, 2106860, Copyright ©2022.

interface (ALI) form partial epidermal stratification with moderate barrier integrity, failing to accurately mimic the multilayered architecture and dynamic physiological processes of native skin, thus limiting their utility in disease modeling and drug evaluation. In recent years, skin-on-chips, leveraging multi-channel microfluidic technologies, have emerged as advanced *in vitro* models capable of reproducing stratified 3D tissues under dynamic perfusion conditions. These dynamic multi-channel skin-on-chips integrate perfused dermal and epidermal compartments with flow rates of 0.05–0.5 dyn cm^{-2}. This enhances nutrient delivery and barrier maturation (TEER $>$ 3000–5000 Ω cm^2, permeability 10^{-7}–10^{-8} cm s^{-1}) and leads to IL-6/IL-8 upregulation several folds after chemical challenge, providing a physiologically responsive epidermal model, offering *in vivo*-like physiological fidelity and prolonged experimental stability.[94,203] A variety of structural designs have been developed, including the perfusable microfluidic network,[234–236] and the porous membranes.[118,237,238]

With advancements in microfluidic technology, researchers have developed a range of representative skin-on-chips aimed at reconstructing multilayered skin structures and enhancing their applicability in toxicity testing and disease studies. For instance, Jeon *et al.*[204] fabricated a PDMS-based microfluidic chip composed of upper and lower layers separated by a porous membrane, integrated with a gravity-driven perfusion system to investigate sorafenib-induced skin side effects. Sriram *et al.*[118] developed a full-thickness human skin chip device (Fig. 11a) with modular compartments and a fibrin-based dermal matrix, which effectively reconstructed a realistic skin barrier microenvironment and supported research on epidermal morphogenesis, differentiation, and barrier function. To further replicate the skin structure and function, and to expand applications in disease modeling and cosmetic drug testing, researchers have introduced more targeted and innovative structural designs in recent years. For instance, Lim *et al.*[239] employed soft lithography to create a wrinkled skin-on-a-chip (Fig. 11b) integrated with a cyclic uniaxial stretching device, simulating the skin aging process for anti-wrinkle research. This study also provides a reference for the development of better skin models within the skin-on-a-chip. Such polymorphic systems hold promise as platforms for predicting cosmetic and dermatological toxicity. To investigate drug absorption, distribution, and mechanisms of action in the skin, Sun *et al.*[51] developed an immunologically active skin chip with vascularized dermis, supporting immune cell perfusion and drug delivery for simulating HSV infection and immune responses. To further validate the role of perfusable vascular networks in simulating skin barrier function, Mori *et al.*[94] developed a skin equivalent model (Fig. 11c) featuring perfusable vascular channels that exhibited typical dermal/epidermal morphology and formed effective barrier structures through endothelial tight junctions. The model supported nutrient delivery and demonstrated superior physiological relevance compared to static cultures, highlighting its potential for applications in vascular uptake studies, drug discovery, and cosmetic testing. These technological advances offer powerful platforms for more physiologically relevant, high-throughput studies in skin biology and disease research.[240]

Dental and oral OoCs

The oral cavity is a complex and dynamic biological system comprising multiple interacting tissues, including the oral mucosa, gingiva, enamel, dentin, and a diverse community of resident microbiota. These components form intricate structural and functional interfaces that collectively maintain oral homeostasis, provide mechanical and chemical protection, and mediate immune defense. However, conventional 2D cell cultures and static Transwell systems fail to recapitulate the physiological conditions of the oral microenvironment, such as the air–liquid interface, saliva flow, and host–microbe interactions. They also lack the capacity to reproduce the dynamic mechanical stimuli and continuous chemical exposures that occur *in vivo*. Consequently, these traditional *in vitro* models are limited in their ability to faithfully mimic oral barrier function, biofilm development, and host–pathogen crosstalk.[241] To overcome these limitations, emerging dental and oral OoC platforms, based on multichannel microfluidic architectures, have been developed as promising tools to replicate the complex biological, chemical, and mechanical microenvironments of the oral cavity, enabling more physiologically relevant investigations into oral health and disease mechanisms.[242]

With advances in microfluidic and tissue-engineering technologies, a variety of oral and dental OoC systems have been developed to reproduce the complex microarchitecture and dynamic environment of the oral cavity. Muniraj *et al.*[201] developed a gingiva-on-a-chip with three interconnected microchannels (epithelial, connective-tissue, perfusion) using a thermoplastic material and a vertically-stacked design—enabling the air–liquid interface critical for barrier maturation, co-culture of keratinocytes and fibroblasts under continuous flow, preservation of barrier integrity and immune responsiveness, and dynamic exposure to bacterial stimuli and dental materials. Similarly, Makkar *et al.*[200] developed a gingival crevice-on-a-chip, which reproduces the dynamic flow and host–microbe interactions of the gingival sulcus through a parallel microchannel architecture (Fig. 12a). Gingival epithelial cells and periodontal pathogens were co-cultured in adjacent channels, enabling real-time observation of biofilm formation and epithelial inflammatory responses under controlled microflow conditions. This platform effectively mimics the local microenvironment of the oral cavity and provides a versatile tool for studying periodontal inflammation and antimicrobial drug testing. These soft tissue-based oral chips have enabled dynamic and physiologically relevant modeling of host–microbe interactions, overcoming the limitations of conventional static co-culture systems. Beyond soft tissue modeling, recent

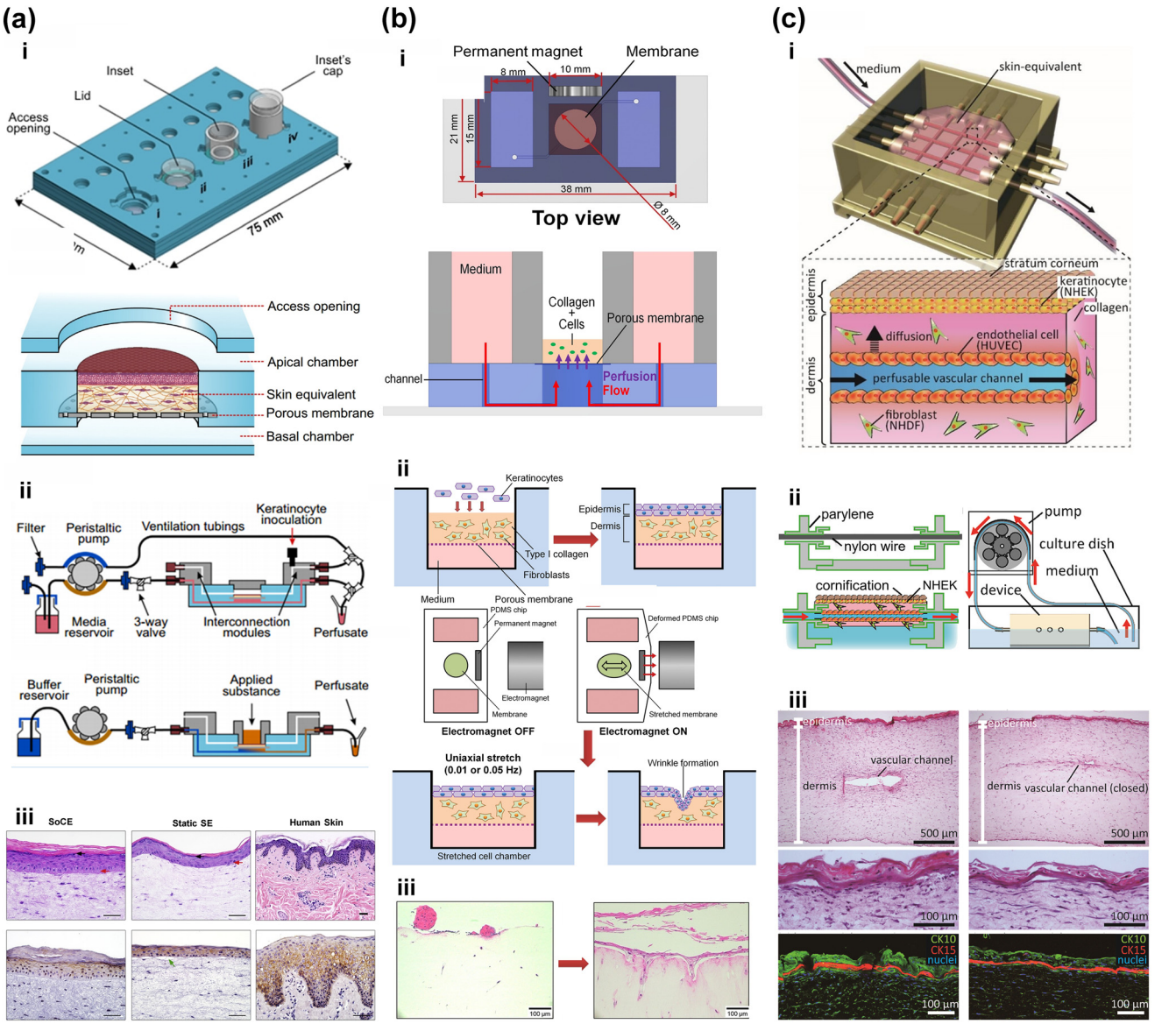

Fig. 11 Skin-on-a-chip platforms. (a) A platform simulating the human skin structure and function for studying skin physiology and applications in drug screening and toxicology. i and ii) Platform design featuring a microfluidic chip with four independent culture units separated by permeable membranes. iii) Histological images of skin-on-a-chip equivalents showing enhanced epidermal differentiation and barrier function, indicated by a thicker stratum corneum and stronger basement membrane compared to static skin equivalents, adapted from ref. 118 with permission from Elsevier Ltd., Sriram *et al.*, *Mater. Today*, 2017, **21**, 326–340, Copyright ©2017. (b) A platform simulating skin stretching and aging for studying wrinkle formation and anti-aging treatments. i and ii) Wrinkled skin-on-a-chip design featuring a PDMS chamber with an embedded magnet for cyclic stretching. iii) H&E staining images showing more pronounced and deeper wrinkles in skin equivalents stretched at 0.01 Hz compared to static conditions, indicating optimal wrinkle induction at this frequency, adapted from ref. 239 with permission from Elsevier Ltd., Lim *et al.*, *J. Ind. Eng. Chem.*, 2018, **68**, 238–245, Copyright ©2018. (c) A platform simulating human skin with perfusable vascular channels for studying skin physiology and drug absorption. i and ii) Platform design featuring vascular channels coated with endothelial cells, integrated into the dermal layer and connected to an external perfusion system *via* connectors. iii) Histological images showing a well-organized epidermal and dermal layer with open vascular channels under perfused conditions, indicating functional barrier properties and nutrient supply pathways, adapted from ref. 94 with permission from Elsevier Ltd., Mori *et al.*, *Biomaterials*, 2017, **116**, 48–56, Copyright ©2017.

research has extended OoC strategies to hard dental tissues, such as dentin, to better simulate the structural and biochemical interactions within the tooth architecture. Zhang *et al.*[243] developed a dentin-on-a-chip platform integrating microfluidic design with tissue-engineering techniques to model dentin formation and evaluate dental biomaterials. The device features three parallel microchannels loaded with stem cells from the apical papilla (SCAPs) encapsulated in a GelMA hydrogel. Optimal conditions were identified at a 5% GelMA concentration and a seeding density of 2×10^4 cells per μL, which promoted higher cell viability and enhanced odontogenic

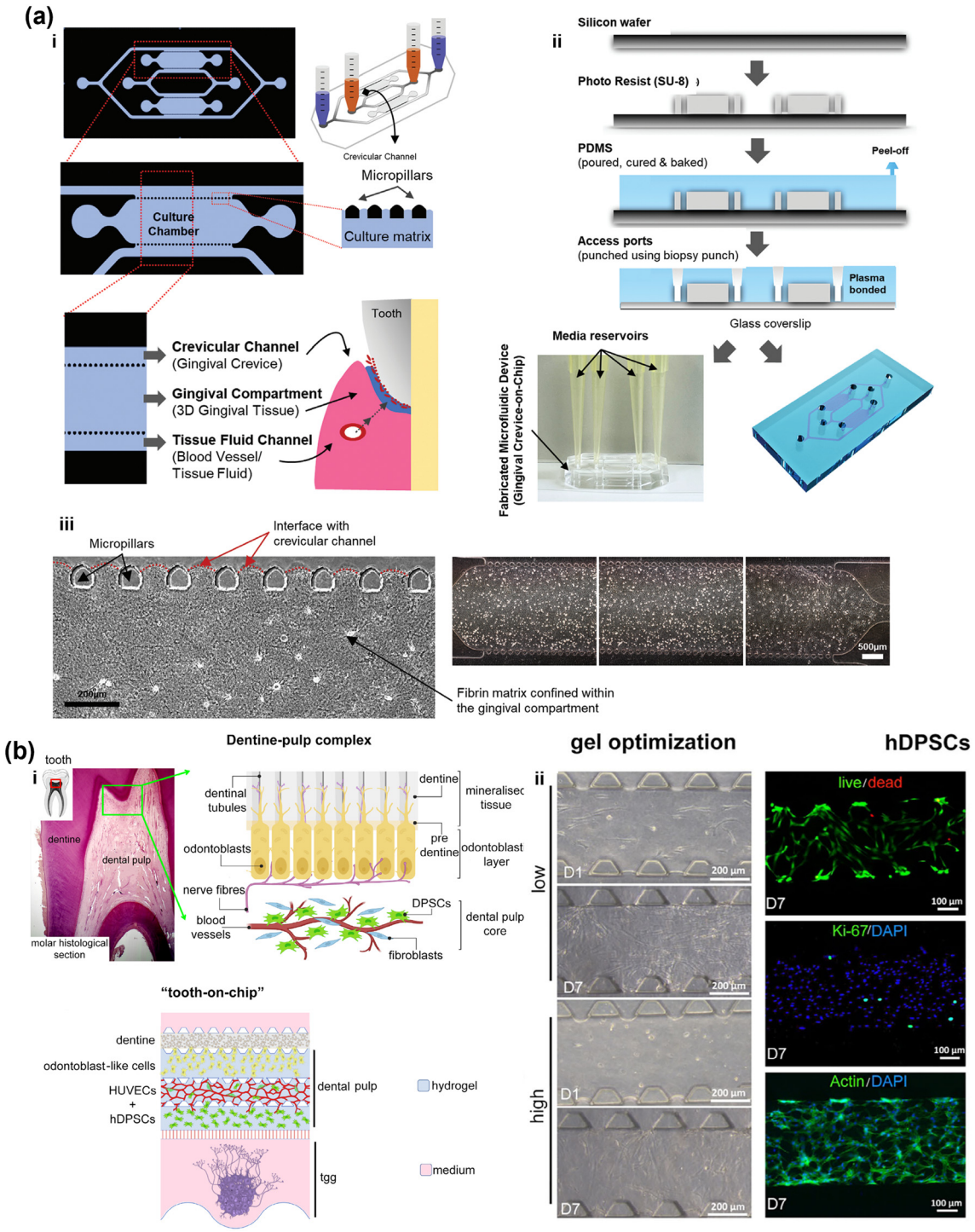

Fig. 12 Oral and dental OoCs platforms. (a) Gingival crevice-on-a-chip microfluidic device. i) Schematic of the device (overall design and components). Enlarged insets show the central culture chamber (gingival compartment) flanked by microfluidic channels (tissue fluid and crevicular channels). Channels connect to the chamber *via* micropillar gaps (act as burst valves) for confining the cell-enmeshed matrix. ii) Schematic of fabrication process flow *via* soft lithography. iii) Stitched micrographs of the gingival compartment showing uniform seeding of the cells enmeshed in the human fibrin matrix, adapted from ref. 200 with permission from Wiley-VCH GmbH, Makkar *et al.*, *Adv. Healthcare Mater.*, 2023, **12**, 2202376, Copyright ©2022. (b) Dental microanatomy & microfluidic model. i) Left: Human molar H&E staining (dental pulp organization). Right: Dentine–pulp interface schematic. ii) Tooth-on-a-chip (post-seeding): dental pulp compartment (dentine layer, odontoblasts, HUVECs, hDPSCs); trigeminal ganglion compartment (mouse embryo-derived ganglion). iii) hDPSC niche characterisation. Left, upper image: representative images of live (green) and dead (red) cells, adapted from ref. 199 with permission from Wiley-VCH GmbH, Cordiale *et al.*, *Adv. Healthcare Mater.*, 2025, e02080, Copyright ©2025.

differentiation compared to 10% GelMA. Live/dead staining and mineralization assays confirmed uniform cell distribution and robust dentin-like matrix deposition. This simplified dentin-on-a-chip model provides a promising *in vitro* platform for regenerative endodontics and dental material testing. In recent years, with deeper investigation, an integrated "tooth-on-a-chip", incorporating dentin, pulp, and related dental tissue, has emerged as a novel and promising research direction. Cordiale *et al.*[199] developed an innovative tooth-on-a-chip platform that emulates the complex structure and physiological functions of the dental pulp tissue (Fig. 12b). The microfluidic device integrates multiple interconnected chambers representing vascular, neuronal, and odontoblastic compartments, thereby recapitulating the native architecture of the dentin–pulp complex. Human dental pulp stem cells (DPSCs), endothelial cells, and trigeminal-derived neurons were co-cultured within these compartments to reconstruct the vascularized and innervated microenvironment of the pulp tissue. This design enables the real-time investigation of dentin–pulp interactions, neurovascular coupling, and pulp regenerative responses under near-physiological flow conditions. By integrating vascular and neuronal elements into a single microfluidic framework, the system provides a high-fidelity biomimetic platform for studying dental pulp physiology, inflammatory mechanisms, and biomaterial responses *in vitro*. Franca *et al.*[241] developed a tooth-on-a-chip platform that replicates the dentin–pulp interface to investigate the biological responses of dental tissues to restorative materials. The device consists of two microchambers separated by a thin dentin slice, allowing controlled perfusion of the culture medium and precise evaluation of cell–material interactions. This setup effectively mimics the native tooth microenvironment and enables real-time monitoring of odontoblastic cell responses to dental adhesives and resin monomers, including cytotoxicity and molecular diffusion across the dentin barrier. These hard tissue-focused models extend the OoC concept beyond soft-tissue barriers, providing a biomimetic framework for evaluating dental biomaterials, regenerative strategies, and pulp–dentin dynamics under near-physiological conditions.

Multi-organ-on-a-chip

Multi-OoCs, a sophisticated multi-channel microfluidic platform, seamlessly integrate multiple organotypic components within a single chip. Single organ chips are interconnected in series or parallel configurations, sharing a perfusion system, thus enabling the formation of multi-OoCs such as liver–heart–bone–skin platforms. Each component, comprised of specific tissues or cells, endows the system with the capacity to accurately emulate complex interorgan crosstalk and reconstruct the physiological microenvironment.[244] Compared to single-OoCs, multi-OoCs significantly enhance physiological relevance and reproduce physiological interactions between tissues by integrating microfluidic modules that mimic the dynamic exchange of metabolites, hormones, and cytokines, thereby improving the accuracy of drug efficacy predictions and toxicity assessments.[245] Quantitative alignment among organ compartments, specifically in terms of flow rate, circulating volume, and residence time, is essential to ensure physiological scaling. Inappropriate flow ratios or residence times can lead to metabolic overload or inaccurate pharmacokinetic modeling. Details of the fluidic parameters, matched physiological biomarkers, and coupling models employed in different multi-OoC systems are listed in Table 5. Characterized by their flexibility, cost-effectiveness, and reproducibility, these chips emerge as optimal tools for personalized and precision medicine research. In contemporary research, multi-OoCs are predominantly utilized for the assessment of metabolic function,[246,247] the modeling of diseases and the investigation of their mechanisms.[248–250]

The integration of multiple organotypic components within multi-OoC platforms enables the precise replication of interorgan interactions and systemic metabolic functions,

Table 5 Key fluidic parameters, physiological biomarkers, and coupling models employed in representative multi-organ platforms

Model example	Coupling architecture	Chip and fluidic parameters	Matched biomarkers	Ref.
Gut-to-liver	Serial connection; pump-driven closed loop	Circulating volume: gut OoC 2 mL, liver OoC 1.6 mL; recirculating flow rates: 30 mL per day; relative flow ratio: gut : liver = 1 : 5; shear stress: gut 0.02–0.2 dyn cm^{-2}, liver 0.1–1 dyn cm^{-2}	SCFA, ketone bodies, glycolysis, and lipogenesis; IFN-γ, TNF-α, IL-1a, RANTES, IL-5, IL-8, IL-10, and IL-13; RNA-seq	45
Liver–heart	Parallel coupling; pump-driven closed loop	Circulating volume: liver OoC 75 μL, heart OoC 75 μL; relative flow ratio: liver–heart = 1 : 6; shear stress of 0.1–1 dyn cm^{-2}	Albumin and urea, CYP450 enzyme genes, desmethylclomipramine; cTnT, TNNT3, calcium flux	246
Adipose–liver	Serial connection; closed-loop perfusion	Circulating volume: 0.3–0.5 mL for adipocyte–liver OoC; relative flow ratio: adipocyte–liver = 1 : 6–1 : 15, shear stress of 0.01–0.1 dyn cm^{-2} (adipose) and 0.1–1 dyn cm^{-2} (liver)	Insulin resistance biomarkers, adipocytes TNF-α, CYP3A4	47
Gut–skin	Parallel coupling; gravity-induced flow for perfusion	Circulating volume: gut OoC 200 μL, skin OoC 200 μL; flow rate of 10 μL min^{-1} after 1 day; 0.05–0.3 dyn cm^{-2} (skin)	Interleukin-6, nitric oxide (NO) levels, efensin-2	248

making these systems valuable tools for disease modeling and therapeutic research. For instance, Trapecar *et al.*[45] employed a multi-OoC to integrate gut, liver, and immune cell microphysiological system (MPS), featuring a gut-to-liver flow rate ratio of 1 : 5–1 : 10, with a shear stress of 0.02–0.2 dyn cm^{-2} and 0.1–1 dyn cm^{-2}. This setup demonstrated that SCFAs exert paradoxical effects in inflammatory bowel disease (IBD) depending on the T-cell activation status, thereby uncovering a novel immunometabolism regulatory mechanism. Slaughter *et al.*[47] designed a two-channel microfluidic chip platform (Fig. 13a) (fabricated *via* laser ablation, channel width: 50–200 μm) separated by a porous polycarbonate membrane (pore size: 4–10 μm), providing a robust tool for in-depth research on NAFLD pathogenesis.

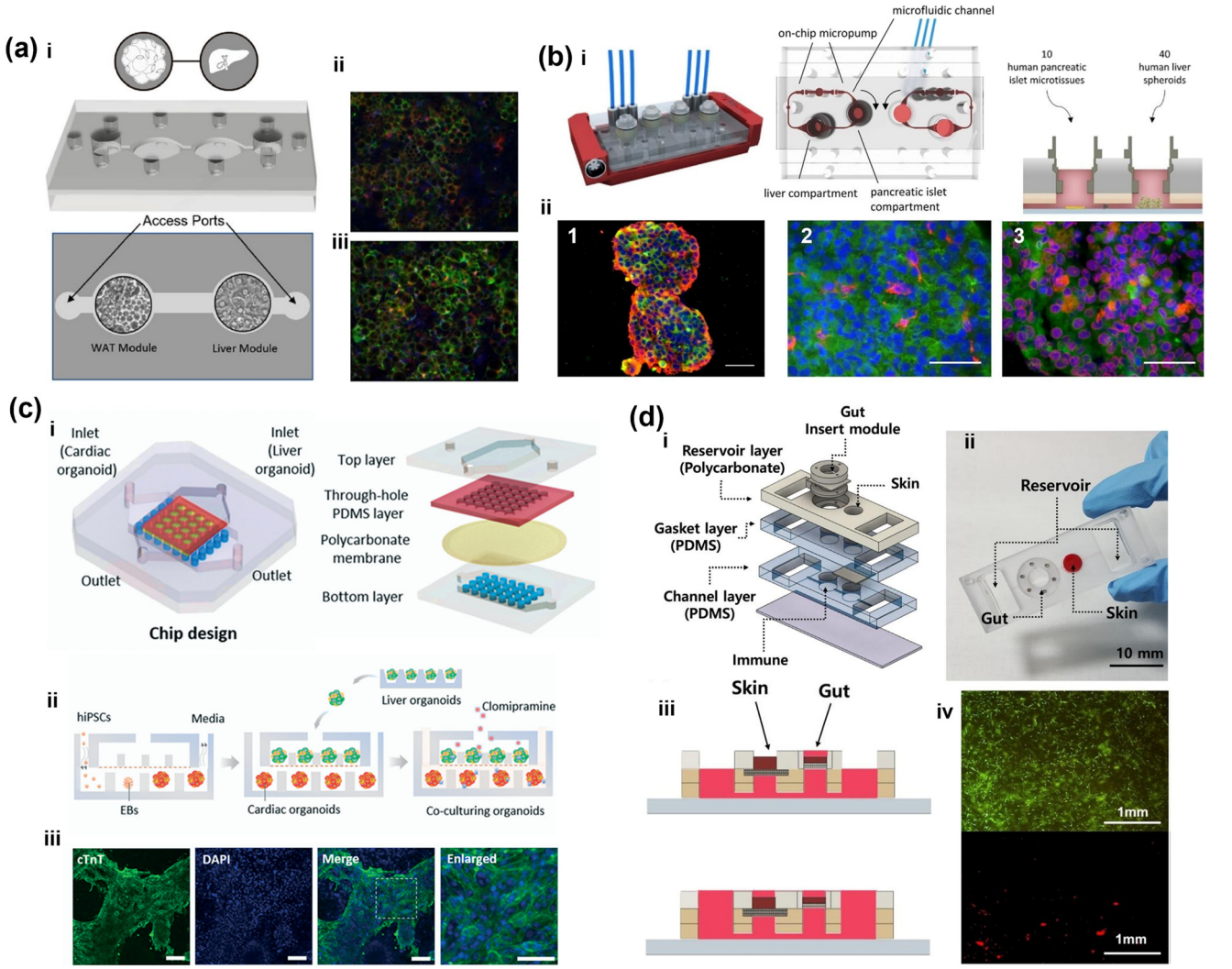

Fig. 13 Multi-organ-on-a-chip platforms. (a) A platform simulating adipose–liver interactions for studying NAFLD mechanisms and drug efficacy. i) Two-chamber microfluidic design with interconnected adipocyte and hepatocyte modules. ii and iii) Oil Red O staining images showing increased hepatocyte lipid accumulation in obese and proinflammatory media, indicating that adipocyte-derived factors drive NAFLD progression, adapted from ref. 47 with permission from Springer Nature, Slaughter *et al.*, *Sci. Rep.*, 2021, **11**, 13159, Copyright ©2021. (b) A platform simulating human pancreas–liver interactions for studying glucose homeostasis and type 2 diabetes mechanisms. i and ii) Two-organ-on-a-chip design with separate compartments for pancreatic islets and liver spheroids connected by microfluidic channels. iii–v) Immunohistochemistry images of pancreatic islets and liver spheroids showing functional insulin and glucagon expression in islets and intact cellular distribution in liver spheroids, indicating preserved functionality before co-culture. Scale bar: 50 μm, adapted from ref. 247 with permission from Springer Nature, Bauer *et al.*, *Sci. Rep.*, 2017, **7**, 14620, Copyright ©2018. (c) A platform simulating human liver–heart interactions for studying drug metabolism and cardiotoxicity. i and ii) Multi-organoid-on-a-chip design featuring compartmentalized chambers for culturing liver and heart organoids. iii) Immunostaining of cTnT in cardiac organoids, indicating successful differentiation and functional maturation of cardiomyocytes. Scale bars, 100 μm, adapted from ref. 246 with permission from The Royal Society of Chemistry, Yin *et al.*, *Lab Chip*, 2020, **21**, 571–581, Copyright ©2020. (d) A platform simulating the gut–skin axis for studying interorgan communication and inflammatory responses. i–iii) Dual-organ chip design with separate gut and skin compartments connected by microfluidic channels. iv) Fluorescence microscopy image showing live/dead staining results with high viability of skin cells (fibroblasts and keratinocytes), indicating effective maintenance of cell health during coculture, adapted from ref. 248 with permission from Wiley Periodicals LLC, Lee *et al.*, *Biotechnol. Bioeng.*, 2022, **119**, 2590–2601, Copyright ©2022.

This platform achieved an adipocyte-to-liver flow ratio of 1 : 6–1 : 15, with a shear stress of 0.01–0.1 dyn cm^{-2} (adipose) and 0.1–1 dyn cm^{-2} (liver), and quantified lipid accumulation in hepatocytes to evaluate drug treatment effects. Bauer *et al.*[247] engineered a two-OoC system with spatially segregated pancreatic islets and hepatic microtissues interconnected *via* microfluidic channels (Fig. 13b). This system demonstrated functional mimicry of pancreas–liver interactions through biomarker validation, offering a biomimetic model to study diabetes pathogenesis. Yin *et al.*[246] developed a liver–heart OoC with a four-layer structure to co-culture iPSC-derived liver and heart organoids (Fig. 13c). This platform maintained a liver-to-heart flow rate ratio of 1 : 3–1 : 6, with a shear stress of 0.1–1 dyn cm^{-2} (both organs), achieved TEER values of 600–1200 Ω cm^2 for cardiac endothelial barriers, and enabled cardiotoxicity screening by tracking CYP3A4 activity in liver organoids and functional changes (synchronized beating at 1–2 Hz, systolic stress of 8–20 kPa) in heart tissues exposed to metabolized drugs. Lee *et al.*[248] created a modular gut–skin axis chip with interconnected channels and 0.05–0.3 dyn cm^{-2} (skin), supporting an independent yet integrated culture of intestinal and 3D skin tissues (Fig. 13d). By enabling perfusion-driven inter-organ communication, it models gut barrier dysfunction-induced skin inflammation—characterized by reduced gut TEER (from 600–800 to 200–300 Ω cm^2), with potential for integration into microbiome–immune system interaction studies. These systems collectively advance *in vitro* multi-organ modeling for precision disease research and drug development.

Recent developments have extended the use of these systems to model complex pathological processes, such as tumor metastasis and drug pharmacokinetics, enabling more refined analyses of systemic disease dynamics. Xu *et al.*[251] developed a dynamic BBB organoid-on-a-chip *via* photolithography, integrating vascular, gas, and gel channels to replicate a multi-layer structure. These microfluidic channels enable precise modeling of tumor cell metastasis by tracking cancer cell migration from vascular compartments to brain regions, while excluding non-invasive cells (*e.g.*, liver cancer), in alignment with clinical observations. Moon *et al.*[252] designed a dual-layer microfluidic platform through soft lithography. The chip's circulatory system simulates key drug delivery stages: vascular extravasation, tumor tissue diffusion, cellular uptake, and lymphatic clearance, effectively replicating human pharmacokinetics. These cutting-edge multi-OoC systems offer versatile tools for high-fidelity disease modeling and drug evaluation, providing a new paradigm for precision medicine and biomedical research.

Other organ-on-chips

In addition to the aforementioned models, emerging multi-channel microfluidic platforms such as spleen-on-a-chip,[253,254] cochlea-on-a-chip,[255] and cornea-on-a-chip[256,257] have been developed to replicate complex human organ structures and functions. By mimicking physiological processes such as splenic red blood cell (RBC) filtration,[253] cochlear Ca^{2+} signaling dynamics, and corneal drug absorption, these platforms support high-fidelity studies on drug toxicity, disease mechanisms, and personalized treatment strategies.

The spleen, an organ that mechanically filters aging/damaged red blood cells (RBCs), can be functionally replicated by OoCs through multi-channel microfluidics that mimic splenic microcirculation and retention of poorly deformable RBCs. To study the mechanical filtration function of the spleen, Picot *et al.*[253] developed a microfluidic device to investigate and quantify the mechanical properties of RBCs as they traverse the human spleen (Fig. 14a). The structure comprises eight parallel filtration units and access channels, which include narrow filtering slits located at the exit of the slow circulation pathway. When these slits become saturated, they redirect RBCs through a wider, rapid circulation pathway. The filtration units consist of localized mechanical filters with equivalent pore sizes ranging from 5 to 2 μm. This device effectively filters RBCs with altered mechanical properties, enabling differentiation between infected and non-infected RBCs, as well as between young and late-stage infected RBCs. Similarly, Businaro *et al.*[258] designed a chip featuring two main channels adjacent to cell culture chambers, effectively simulating tumor–immune cell interactions such as infiltration and efflux. L. G. Rigat-Brugarolas *et al.*[254] designed a novel microengineering device that simulates hydrodynamic conditions and the physical characteristics of the spleen (Fig. 14b). The chip structure includes fast and slow flow channels, with the slow flow channel incorporating a columnar matrix to replicate the filtering bed of the red pulp. This platform integrates two compartments representing the reticular network and intra-splenic erythrocyte (IES) system, utilizing human RBCs and malaria-infected cells to evaluate the spleen's mechanical and physiological responses.

Hearing loss is one of the most common sensory disorders, and its pharmacological treatment is constrained by the complex structure of the ear. In recent years, various cellular models have been employed to develop therapeutic drugs for inner ear injury. Hu *et al.*[259] combined cochlear organoid cultures with a microfluidic device to construct a branched cochlea-on-a-chip (Fig. 14c). This structure comprises a four-layer concentration gradient generator, six independent rectangular cell culture chambers, two inlets, and one outlet. The cell culture chambers are connected to the terminal branches of the generator. By integrating inner ear progenitor cells encapsulated in a hydrogel into the culture chambers, mature cochlear organoids can be cultured to maturity, enabling high-throughput screening of ototoxicity and therapeutic efficacy for hearing loss. In a related study, Shen *et al.*[255] developed a cochlear chip integrated with a biosensor to monitor intercellular Ca^{2+} signaling and ATP-mediated responses, shedding light on hearing acquisition and age-related degeneration.

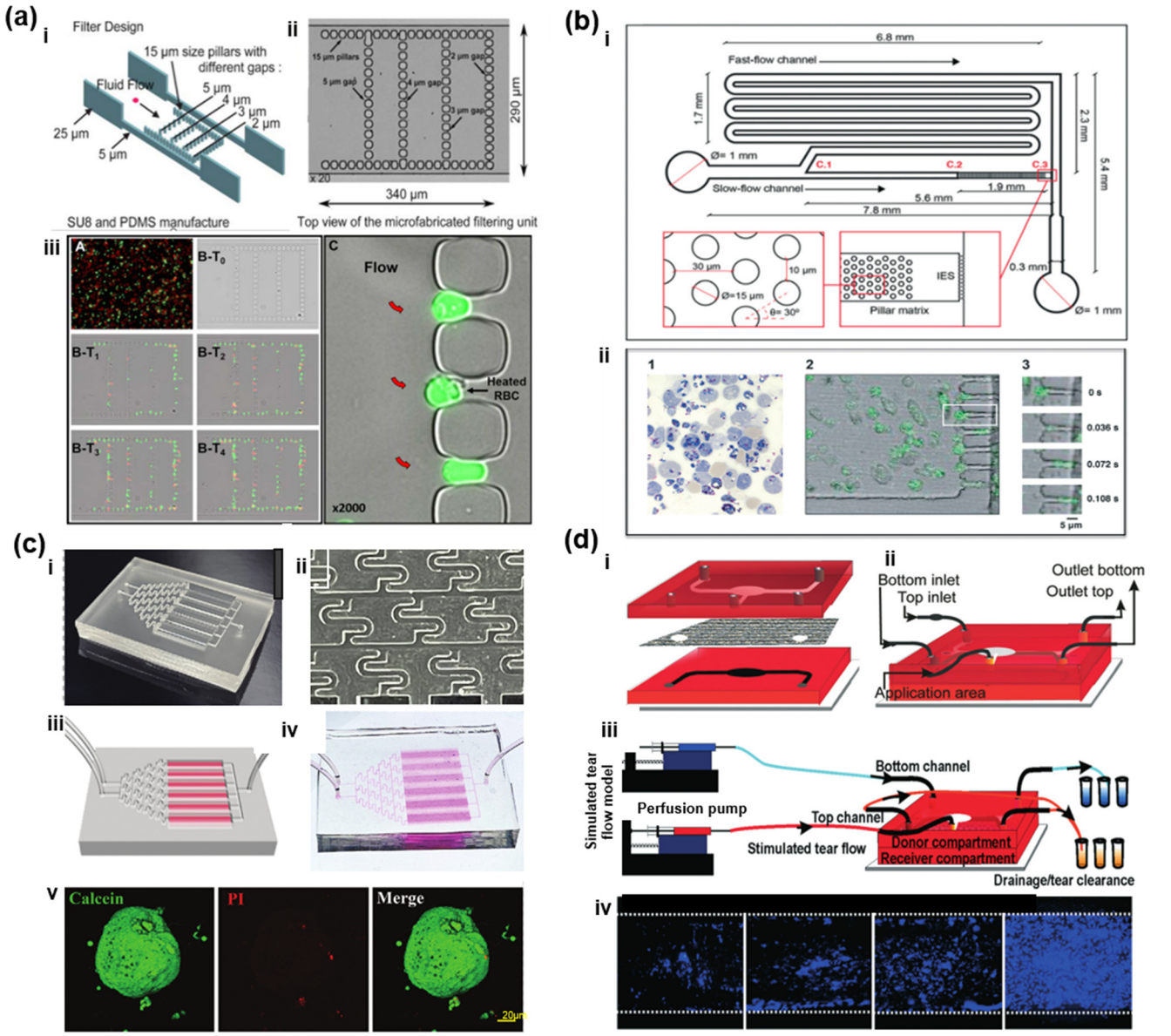

Fig. 14 Other OoCs platforms. (a) A microfluidic chip simulating the spleen's mechanical filtration for studying RBC deformability and retention. i and ii) Chip design with microchannels leading to filtering units containing 53 slits (2 mm wide) between 15 mm pillars, with side channels for flow distribution. iii) Experimental results showing heated RBCs (green, PKH67) accumulating in narrow slits over time, while normal RBCs (red, PKH26) flow through without retention, demonstrating the chip's ability to discriminate poorly deformable RBCs, adapted from ref. 253 with permission from Wiley Periodicals, Picot *et al.*, *Am. J. Hematol.*, 2015, **90**, 339–345, Copyright ©2015. (b) A platform simulating the human spleen's filtering function for studying malaria and hematological disorders. i) Spleen-on-a-chip design with two microfluidic channels and microconstrictions representing the interendothelial slits. ii) Fluorescence images of malaria-infected reticulocytes passing through microconstrictions, indicating higher deformability of infected cells compared to non-infected ones, adapted from ref. 254 with permission from The Royal Society of Chemistry, Rigat-Brugarolas *et al.*, *Lab Chip*, 2014, **14**, 1715–1724, Copyright ©2014. (c) A platform simulating the inner ear environment for studying cochlear organoid development and drug screening. i–iv) Cochlea-on-a-chip design with a tree-shaped concentration gradient generator, six independent culture chambers, and a microfluidic layout for dynamic drug exposure. v) Live/dead staining of cochlear organoids, showing high cell viability and indicating the chip's effectiveness in supporting organoid maturation, adapted from ref. 259 with permission from Wiley-VCH GmbH, Hu *et al.*, *Adv. Mater.*, 2024, **36**, 2309002, Copyright ©2024. (d) A platform simulating the human corneal epithelium for studying ocular drug permeation and pharmacokinetics. i–iii) Cornea chip structure with apical and basal microfluidic channels separated by a fibronectin-coated porous membrane, designed to simulate tear dynamics and corneal epithelium interactions under static, continuous flow, and pulsatile flow conditions. iv) Cell growth results showing uniform cell coverage at 1.5×10^6 cells per mL, indicating optimal cell density for confluence and barrier formation, adapted from ref. 256 with permission from The Royal Society of Chemistry, Bennet *et al.*, *Lab Chip*, 2018, **18**, 1539–1551, Copyright ©2018.

The human cornea is closely associated with severe visual impairment, ocular diseases, and eye disorders. Current ocular drug testing urgently requires physiologically relevant models that replicate the structure and function of the

cornea. Bennet *et al.*[256] developed a membrane epithelial chip to simulate the barrier function of the human corneal epithelium during drug testing (Fig. 14d). This chip features an upper channel, a lower channel, and one drug application area, separated by a porous membrane coated with the ECM. The model investigated the mass transfer efficiency of ophthalmic drugs in both suspended and liquid forms, validating the correlation between the mass transfer efficiency of two formulations and their compositional ingredients. Deng *et al.*[257] developed an *in vitro* biomimetic construct *via* co-culturing immortalized human corneal epithelial cells and primary fibroblasts on porous PDMS membranes. This open system enabled analysis of bacterial, epithelial, and fibroblast responses to antibiotics (levofloxacin, tobramycin, and chloramphenicol), revealing differences in antibacterial efficacy, apoptosis inhibition, and scar reduction under corneal epithelial barrier conditions. These models provide support for methods in ocular drug testing.

Relevance of multi-channel systems for barrier tissue modeling

Barrier tissues such as alveoli, oral and nasal mucosa, intestinal epithelium, and skin are continuously exposed to complex physiological interfaces, including air–liquid,[23,260] host–microbe,[42,96,100] and tissue–tissue interfaces.[20,31,261] These interfaces are not only structurally compartmentalized but also dynamically regulated by biochemical and mechanical cues that maintain epithelial homeostasis and barrier integrity. Conventional single-channel systems often fail to recapitulate the coordinated physiological processes that occur across these interconnected interfaces.

Multi-channel OoC platforms offer an effective solution to these challenges. By integrating spatially separated microenvironments with precisely controlled fluidic networks, multi-channel designs enable the simultaneous reconstruction of multiple physiological interfaces within a single device. This architecture allows orderly intercompartmental communication and dynamic simulation of key physiological processes—such as epithelial barrier permeability regulation,[29] immune cell trafficking,[20,30] microbial colonization,[225] and responses to environmental stress[262] or under near-physiological conditions.[49]

Representative architectures have been proposed to meet the specific functional requirements of different interfaces. For instance, in lung or oral epithelial chip models, vertically aligned dual-channel structures separated by a porous membrane can establish an ALI, where the upper channel is exposed to air while the lower channel is continuously perfused with a medium.[25,263] This configuration promotes epithelial polarization and tight junction formation, both of which are essential for maintaining barrier selectivity and permeability. In host–microbe interface models, parallel or layered microchannel architectures enable spatial co-culture of host cells and microorganisms.[42,96] Under controlled shear flow, such systems preserve microbial viability and allow real-time observation of host–pathogen interactions and inflammatory signaling. Moreover, host–environment interface models often[106,108,264] employ lateral perfusion channels or dedicated exposure chambers to introduce aerosols, nanoparticles, or chemical agents in a controlled manner, enabling dynamic monitoring of epithelial and immune responses to exogenous challenges.

Through these structurally and functionally integrated designs, multi-channel OoC platforms can faithfully recapitulate the intricate interactions among epithelial, microbial, and environmental components of barrier tissues *in vitro*, offering a powerful tool for studying barrier physiology and advancing translational disease modeling.

5. Conclusions and future prospects

In conclusion, this paper explores the design principles, fabrication methods, and applications involved in the development of OoC models based on multi-channel microfluidics. Although current OoC systems use simplified tissue structures, they have successfully replicated key organ functions, including pulmonary gas exchange, skin barrier integrity, myocardial contractility, and renal filtration. Furthermore, by integrating multiple tissue units, these multi-unit systems can effectively model complex disease processes such as cancer metastasis, inflammation, and infection. Multi-channel microfluidic chips hold great promise as a transformative approach to advancing biomedical research, driving progress in pathophysiological studies, preclinical drug development, and personalized medicine. However, to fully realize the potential of these systems, many opportunities and challenges remain to be addressed (Fig. 15).

5.1 Structural design of OoCs

Currently, multi-channel microfluidic chips often employ porous membranes or micropillar arrays as interfacial structures to construct flow channel combinations. These designs address several key requirements, including supporting cell growth, facilitating material transport, and enabling signal transmission across different compartments. However, it remains uncertain whether discontinuous co-cultured cell layers can fully retain their physiological functions. To overcome these limitations, innovative solutions such as open-channel designs under restrictive conditions and gel-based fully open channels have been developed. These advances not only promote greater cell-to-cell contact and enhance substance exchange, but they also introduce challenges such as operational instability and increased complexity.[265,266]

To better replicate complex physiological conditions, recent advances in microfluidic design have focused on vertical stacking structures and suspended microstructures, enabled by 3D porous membranes or 3D-printed processing technologies.[267] These technologies allow for more efficient

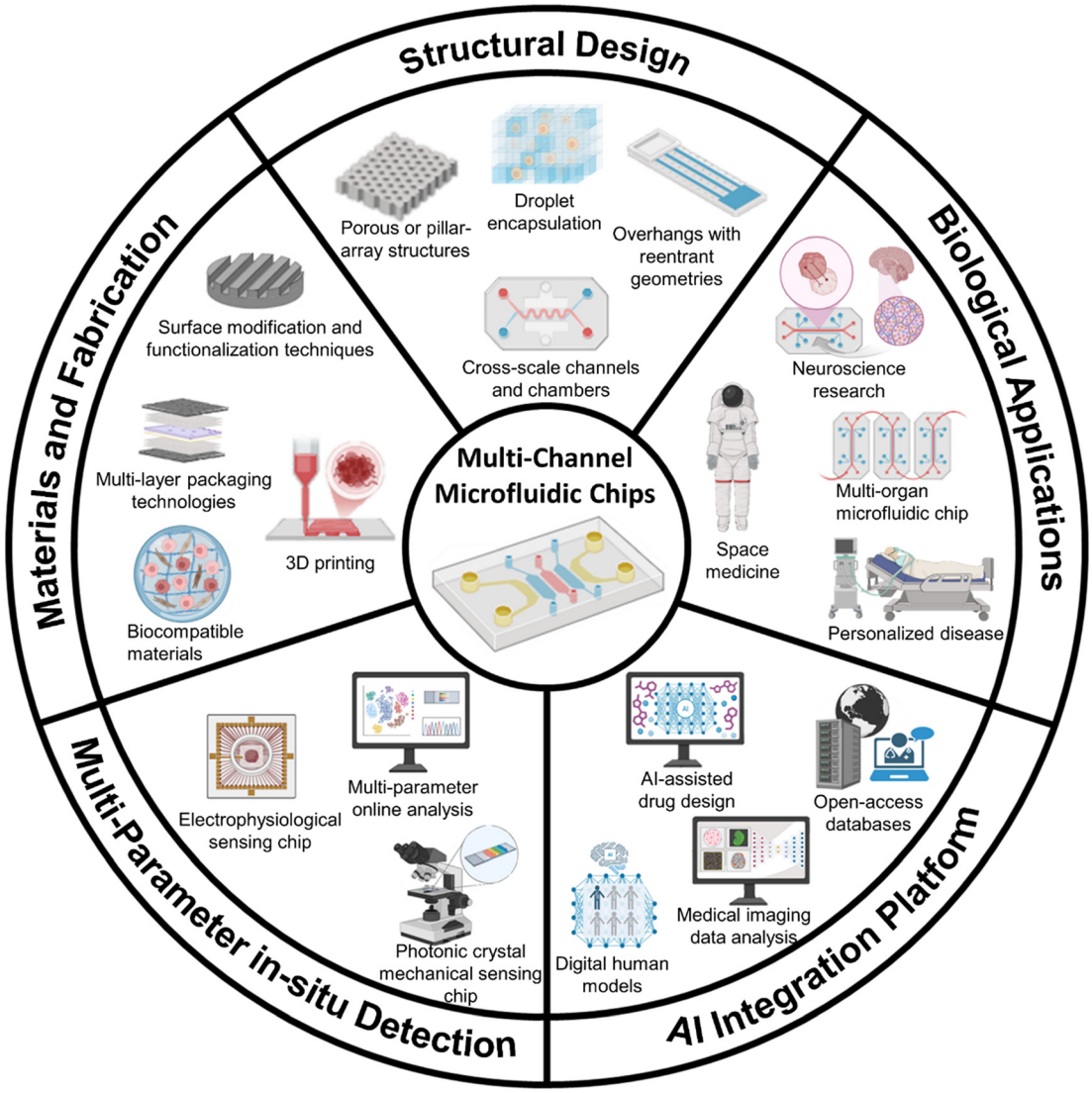

Fig. 15 Future perspectives for OoCs (created using https://www.biorender.com).

3D cell growth and spatial arrangement within ECM networks, improving the efficiency of multi-organ interactions and enabling spatial omics studies. For example, flexible substrates like PDMS-based elastic films are commonly used to fabricate microchambers. Pneumatic or mechanical actuation induces periodic stretching of these membranes, simulating dynamic mechanical stimuli beyond fluid mechanics, such as alveolar breathing, gastrointestinal peristalsis, and cardiac contraction. Furthermore, elastic micropillar structures, which exhibit both deformability and resistance to deformation, are incorporated into OoCs to enhance cell attachment and facilitate the growth and mechanical testing of stretchable cells, such as muscle cells.

While advances in materials, interfaces, and mechanical microstructures have greatly expanded the functional capabilities of OoC platforms, the structural design of multi-channel systems remains a key determinant of physiological relevance. Horizontal and vertical stacking strategies have consequently emerged as distinct architectural paradigms for constructing multi-channel systems with varying levels of structural complexity and biological fidelity.

Horizontal stacking configurations have been extensively explored in multi-channel OoC systems to arrange multiple flow channels or cell compartments side by side. Horizontal stacking offers advantages such as simplified fabrication, convenient optical access for real-time imaging, and easier integration of external fluidic connections. However, it often limits vertical cell-to-cell interactions and the establishment of physiologically relevant three-dimensional microenvironments, which may compromise the fidelity of complex tissue interfaces and multi-organ interactions.[26,104]

In contrast, vertical stacking designs align multiple cellular layers or organ compartments along the *z*-axis, enabling more direct inter-compartment communication, improved spatial organization, and more faithful replication of epithelial–endothelial or vascular–tissue interfaces. These

configurations are particularly suited for modeling barrier functions, paracrine signaling, and substance exchange under physiologically realistic gradients.[23,62] Nevertheless, vertical stacking typically requires more sophisticated fabrication techniques, presents challenges in maintaining uniform perfusion and oxygenation across layers, and increases operational complexity.

Critically, the choice between horizontal and vertical stacking should be guided by the intended biological functions and the specific microphysiological parameters under investigation—for instance, whether spatially coordinated mechanical stimulation, biochemical coupling, or controlled shear stress gradients are essential.[19,268] Moreover, hybrid strategies that integrate both horizontal and vertical compartmentalization, supported by computational fluid dynamics (CFD)-based optimization, are emerging as promising approaches to balance biological realism with engineering feasibility.[17] The incorporation of tailored channel geometries and dynamic flow regulation can further enhance intercellular communication and spatiotemporal control, thereby improving the physiological relevance and scalability of next-generation multi-organ OoC platforms. The incorporation of tailored channel geometries and dynamic flow regulation can further enhance intercellular communication and spatiotemporal control, thereby improving the physiological relevance and scalability of next-generation multi-organ OoC platforms.

The structural design of microfluidic systems also benefits from fluid modeling, which provides theoretical support and optimization strategies for the fine construction of biomimetic structures and multi-organ cascading applications. This helps to precisely control local fluid shear stress and establish fluid gradients in multi-organ circulation systems. Additionally, design theories like the corner effect and pinning effect, combined with advanced microstructures such as overhangs with reentrant geometries, have been incorporated into OoCs to achieve efficient liquid confinement and flexible channel selection.[269] These innovations lay a strong foundation for the stable construction of programmable OoCs.[270] Application cases that leverage capillary forces and Laplace pressure differences demonstrate the feasibility of integrated coupling for droplet encapsulation in drug delivery systems or localized stimuli.[271] These advances further enhance the precise control of dynamic microenvironments within OoCs, enabling more accurate and functional *in vitro* models.

5.2 Materials and fabrication of OoCs

The advancement of materials science has provided the groundwork for improving OoCs. Biocompatibility is a key requirement, while other critical factors include breathability, optical transparency, and minimal molecule adsorption. PDMS is widely used for chip fabrication because it is gas-permeable, biocompatible, and easy to process. However, PDMS absorbs small molecules like drugs and lipophilic substances, which can alter concentrations of biochemical compounds during experiments and reduce accuracy. To address this, surface treatments to reduce extractables on PDMS have been developed.[157,174,184] Alternatives like PMMA and cyclic olefin copolymer (COC) also minimize molecule adsorption and stabilize surface properties. Multi-layer composite packaging techniques optimize the combination of flexible chambers (*e.g.*, PDMS) with rigid materials like glass or silicon. Methods such as plasma surface activation, UV adhesive bonding, thermal pressing, solvent bonding, and heat fusion bonding help mimic the coexistence of soft and hard biological tissues in physiological environments. Gradient-wettability surfaces are created through chemical modification or nanoscale patterning. Biomimetic coatings that simulate ECM components enhance these surfaces, thereby improving fluid flow, biocompatibility, cell adhesion, and functional expression.[272–274]

The manufacturing of OoCs is progressively becoming more diversified. By integrating both additive and subtractive fabrication techniques, multi-layered and 3D interlocking structures with enhanced resolution and stacking precision can be achieved.[274] Multi-scale 3D printing enables the fabrication of tissue features at both micro and macro scales within a single chip, such as vascularized, layered tissue architectures.[148] Additionally, multi-material 3D printing allows for the incorporation of various biomaterials, including hydrogels, thermoplastics, and bio-inks, to create more physiologically relevant and heterogeneous tissue environments.[273] The combination of different 3D printing methods—such as SLA for fine-resolution features and FDM for structural integrity—enables the production of OoCs with tailored performance characteristics, such as improved mechanical strength, optimized fluid dynamics, and enhanced biological activity.[275] These advanced manufacturing techniques significantly improve the ability of OoC models to more accurately replicate human organ physiology, thus advancing their potential applications in disease modeling, drug screening, and the development of personalized therapies.

5.3 Biological applications of OoCs

The ultimate goal of OoCs is to achieve more precise and comprehensive biological structures and functions. These models are powerful tools for investigating physiological mechanisms and developmental processes. For example, brain organoid-on-a-chip systems combine organoid culture with dynamic microenvironments to help unravel human brain complexities or advance bio-intelligence research.[141] Complex disease models and multi-organ interconnected systems are valuable for investigating disease mechanisms, developing therapies, and exploring pathologies of major diseases. Immunized tumor/target organ MPSs aid research into tumor immunotherapy, inflammatory diseases, autoimmune disorders, and infectious diseases.[86,87] These systems also accelerate treatment development, exemplified

by their critical role in addressing the global COVID-19 pandemic. Vascularized or vascular-connected multi-organ MPSs are vital for pharmacokinetics (PK), pharmacodynamics (PD), and toxicology studies in drug development, including environmental evaluations.[4,276] These systems further enable investigations into intercellular and inter-organ interactions, as well as drug distribution in multi-organ diseases such as metabolic disorders (*e.g.*, diabetes and obesity) and cancer metastasis. By integrating flexible biological components and advanced biotechnologies—such as primary tissue culture, stem cell induction, and CRISPR gene editing—MPSs provide a robust platform to address personalized diseases, genetic disorders, and rare conditions. Highly biomimetic MPSs are also critical for space medicine and extreme environment research. They simulate physiological changes under conditions like deep-space radiation (*e.g.*, skeletal muscle loss and cardiovascular degeneration), microgravity, and extreme environments (*e.g.*, hypoxia at high altitudes and extreme cold).[277,278] This supports mission planning for aerospace, polar expeditions, and military operations, ensuring health and safety in challenging environments.

While OoCs show great promise, challenges remain in replicating human physiology, integrating dynamic stimuli, ensuring scalability, and reducing costs.[97] Current OoCs can model basic organ functions but struggle to replicate complex tissues like the brain and heart. Advancements in 3D printing, bioactive hydrogels, and multi-organ systems aim to enhance the tissue architecture and vascular networks. Many models also fail to incorporate essential dynamic stimuli, such as pulsatile forces and shear stress, but integrating pneumatic actuation and microfluidic gradient generators could address this. Cost is another barrier, but low-cost materials and open-source platforms could increase accessibility. Lastly, while OoCs are useful for disease modeling, simulating complex diseases like cancer metastasis and chronic conditions remains limited. Incorporating immune cells, stem cell technologies, and CRISPR gene editing could improve disease modeling and facilitate personalized medicine.[279,280] Overcoming these challenges will be key to fully realizing OoCs' potential in biological applications and personalized treatments.

5.4 Other development directions for OoCs

Integrating multi-parameter *in situ* detection into OoCs represents a key direction for their future development, enabling real-time, non-invasive monitoring of the microenvironment and cellular responses within the microfluidic device. Simultaneous multi-parameter online analysis facilitates the identification of cross-dimensional signaling networks and advances integrated diagnostic and therapeutic strategies. Electrochemical sensors are particularly suitable for real-time monitoring of metabolic activities.[281] For instance, miniaturized electrodes integrated into a liver-on-a-chip can dynamically detect concentration changes of key metabolites such as glucose, lactate, and urea, thereby enabling continuous assessment of organ metabolic function. Optical sensors, including those based on fluorescence or chemiluminescence, are widely used for highly sensitive detection of signaling molecules such as cytokines (*e.g.*, IL-6 and TNF-α). This capability is crucial for deciphering complex cell–cell communication networks in infection or inflammation models. Microelectrode arrays (MEAs) specialize in recording electrophysiological signals.[282,283] In cardiac or neuronal chips, MEAs enable long-term, millisecond-precision recording of field potentials from cardiomyocytes or action potentials from neurons, providing direct evidence for assessing drug-induced cardiotoxicity or neuroactivity. Impedance-based sensors allow for label-free, real-time monitoring of cellular barrier integrity, exemplified by TEER measurements, serving as a core tool for evaluating the function of the BBB or intestinal barrier.[284] Furthermore, emerging physical sensors, such as those incorporating photonic crystal technology, can quantitatively detect mechanical properties of single cells or microtissues (*e.g.*, contractile forces and stiffness). This offers a unique perspective for understanding tissue mechanics and its alterations in disease states.[285] The convergence of these multi-modal sensing technologies ultimately enables the simultaneous acquisition of multi-dimensional biological information, laying a solid technical foundation for constructing precise drug efficacy evaluation platforms and sophisticated disease models.

By combining these sensing modalities, multi-channel OoC platforms can achieve multi-parameter monitoring—simultaneously assessing metabolic activity, electrophysiology, and barrier function in real time.[63,90] Such integrated detection enhances mechanistic understanding and improves predictive accuracy in pharmacodynamic and toxicological assays, thereby advancing OoC systems toward regulatory-grade analytical performance. Furthermore, the mutually reinforcing synergy between artificial intelligence—specifically deep learning that mines complex biological patterns from massive datasets—and microphysiological systems that generate high-throughput, standardized, and physiologically relevant data may become a critical driver in advancing next-generation *in vitro* evaluation and modeling platforms, such as digital human models.[286,287] This integration has the potential to revolutionize our understanding and simulation of complex biological processes. It paves the way for advanced applications in personalized medicine, such as designing customized treatment plans based on individual genetic profiles. Additionally, it enables more efficient drug discovery by screening compounds in a more realistic microenvironment. By combining innovations in materials science, engineering, computational modeling, and biology, this interdisciplinary approach is poised to advance microfluidic technology and expand its impact across diverse fields of biomedical research.

Author contributions

Ji Qiu: writing – original draft; writing – review and editing; visualization; investigation. Jia Yang: writing – original draft; writing – review and editing; visualization. Lihao Liu: writing – review and editing; visualization. Jiameng Wen: writing – review and editing; visualization. Jiachen Yang: writing – review and editing; visualization. Wenwan Shi: writing – review and editing; visualization. Xiaoxiang Gao: writing – review and editing; visualization. Jing Sun: writing – review and editing; funding acquisition. Ling Bai: writing – review and editing; funding acquisition; visualization; conceptualization. Xiaojiang Liu: writing – review and editing; supervision; funding acquisition; visualization; conceptualization. Zhongze Gu: writing – review and editing; funding acquisition; visualization; conceptualization.

Conflicts of interest

There are no conflicts to declare.

Data availability

No primary research results, software or code have been included and no new data were generated or analysed as part of this review.

Acknowledgements

The authors acknowledge the support by the Natural Science Foundation of Jiangsu Province (BK20241268), the Open Research Fund of Southeast University and Jiangsu Province Hospital (2024-M02), the Jiangsu Province Youth Science and Technology Talent Support Project (JSTJ-2024-096), the Start-up Research Fund of Southeast University (RF028623292), the Southeast University Interdisciplinary Research Program for Young Scholars (2024FGC1003), and the National Natural Science Foundation of China (52033002, 82227808, 22002051). Xiaojiang Liu acknowledges the support by the Research Program for Xiaomi Youth Scholars.

Notes and references

1 S. Mi, Z. Du, Y. Xu, Z. Wu, X. Qian, M. Zhang and W. Sun, *Sci. Rep.*, 2016, **6**, 35544.
2 A. O. Stucki, J. D. Stucki, S. R. R. Hall, M. Felder, Y. Mermoud, R. A. Schmid, T. Geiser and O. T. Guenat, *Lab Chip*, 2015, **15**, 1302–1310.
3 L. Di, B. Feng, T. C. Goosen, Y. Lai, S. J. Steyn, M. V. Varma and R. S. Obach, *Drug Metab. Dispos.*, 2013, **41**, 1975–1993.
4 T. Tuntland, B. Ethell, T. Kosaka, F. Blasco, R. X. Zang, M. Jain, T. Gould and K. Hoffmaster, *Front. Pharmacol.*, 2014, **5**, 174.
5 H. Yang, J. Li, Z. Wang, D. Khutsishvili, J. Tang, Y. Zhu, Y. Cai, X. Dai and S. Ma, *Life Med.*, 2024, **3**, lnae016.
6 P. Pound and M. Ritskes-Hoitinga, *J. Transl. Med.*, 2018, **16**, 304.
7 G. Hugo, *CNS Drugs*, 2009, **23**, 915–926.
8 P. Steve, *Nature*, 2014, **507**, 423–425.
9 T. Hartung, *Front. Drug Discovery*, 2024, **4**, 1355044.
10 C. Ma, Y. Peng, H. Li and W. Chen, *Trends Pharmacol. Sci.*, 2021, **42**, 119–133.
11 Y. Wang and J. Qin, *Life Med.*, 2023, **2**, lnad007.
12 Y. Zhang, X. Wang, Y. Yang, J. Yan, Y. Xiong, W. Wang, J. Lei and T. Jiang, *Front. Immunol.*, 2023, **14**, 1093460.
13 J. Vetter, I. Palagi, A. Waisman and A. Blaeser, *Acta. Biomater.*, 2025, **197**, 1–28.
14 A. G. G. Toh, Z. P. Wang, C. Yang and N. Nam-Trung, *Microfluid. Nanofluid.*, 2014, **16**, 1–18.
15 C. Li, W. He, Y. Song, X. Zhang, J. Sun and Z. Zhou, *Biosensors*, 2024, **14**, 336.
16 A. Agarwal, J. A. Goss, A. Cho, M. L. McCain and K. K. Parker, *Lab Chip*, 2013, **13**, 3599.
17 Y. Song, Y. Zhou, K. Zhang, Z. Fan, F. Zhang and M. Wei, *Lab Chip*, 2024, **24**, 4483–4513.
18 D. E. Ingber, *Nat. Rev. Genet.*, 2022, **23**, 467–491.
19 B. Zhang, A. Korolj, B. F. L. Lai and M. Radisic, *Nat. Rev. Mater.*, 2018, **3**, 257–278.
20 D. Huh, B. D. Matthews, A. Mammoto, M. Montoya-Zavala, H. Y. Hsin and D. E. Ingber, *Science*, 2010, **328**, 1662–1668.
21 A. Mathur, P. Loskill, K. Shao, N. Huebsch, S. Hong, S. G. Marcus, N. Marks, M. Mandegar, B. R. Conklin, L. P. Lee and K. E. Healy, *Sci. Rep.*, 2015, **5**, 8883.
22 G. Vunjak-Novakovic, K. Ronaldson-Bouchard and M. Radisic, *Cell*, 2021, **184**, 4597–4611.
23 I. Francis, J. Shrestha, K. R. Paudel, P. M. Hansbro, M. E. Warkiani and S. C. Saha, *Drug Discov. Today*, 2022, **27**, 2593–2602.
24 C. M. Leung, P. de Haan, K. Ronaldson-Bouchard, G.-A. Kim, J. Ko, H. S. Rho, Z. Chen, P. Habibovic, N. Li Jeon, S. Takayama, M. L. Shuler, G. Vunjak-Novakovic, O. Frey, E. Verpoorte and Y.-C. Toh, *Nat. Rev. Methods Primers*, 2022, **2**, 29.
25 Z. Izadifar, A. Sontheimer-Phelps, B. A. Lubamba, H. Bai, C. Fadel, A. Stejskalova, A. Ozkan, Q. Dasgupta, A. Bein, A. Junaid, A. Gulati, G. Mahajan, S. Kim, N. T. LoGrande, A. Naziripour and D. E. Ingber, *Adv. Drug Delivery Rev.*, 2022, **191**, 114542.
26 A. Tajeddin and N. Mustafaoglu, *Micromachines*, 2021, **12**, 1443.
27 S. H. Lee and J. H. Sung, *Adv. Healthcare Mater.*, 2018, **7**, 1700419.
28 L. A. Low, C. Mummery, B. R. Berridge, C. P. Austin and D. A. Tagle, *Nat. Rev. Drug Discovery*, 2020, **20**, 345–361.
29 A. Fedi, C. Vitale, G. Ponschin, S. Ayehunie, M. Fato and S. Scaglione, *ACS Appl. Mater. Interfaces*, 2021, **335**, 247–268.
30 B. Ko, J. Son, J. In Won, B. M. Kang, C. W. Choi, R. Kim and J. H. Sung, *Lab Chip*, 2025, **25**, 2609–2619.
31 D. Park, J. Lee, J. J. Chung, Y. Jung and S. H. Kim, *Trends Biotechnol.*, 2020, **38**, 99–112.
32 G.-J. Kim, K.-J. Lee, J.-W. Choi and J. H. An, *Int. J. Mol. Sci.*, 2021, **22**, 6997.

33 S. Ya, W. Ding, S. Li, K. Du, Y. Zhang, C. Li, J. Liu, F. Li, P. Li, T. Luo, L. He, A. Xu, D. Gao and B. Qiu, *ACS Appl. Mater. Interfaces*, 2021, **13**, 32640–32652.
34 S. Lasli, H. J. Kim, K. Lee, C. A. E. Suurmond, M. Goudie, P. Bandaru, W. J. Sun, S. M. Zhang, N. Y. Zhang, S. Ahadian, M. R. Dokmeci, J. Lee and A. Khademhosseini, *Adv. Biosyst.*, 2019, **3**, 1900104.
35 K. Du, S. Li, C. Li, P. Li, C. Miao, T. Luo, B. Qiu and W. Ding, *Acta Biomater.*, 2021, **134**, 228–239.
36 Y. Zhao, N. Rafatian, E. Y. Wang, Q. Wu, B. F. L. Lai, R. X. Lu, H. Savoji and M. Radisic, *Adv. Drug Delivery Rev.*, 2020, **165-166**, 60–76.
37 V. Y. Sidorov, P. C. Samson, T. N. Sidorova, J. M. Davidson, C. C. Lim and J. P. Wikswo, *Acta Biomater.*, 2017, **48**, 68–78.
38 S. S. Nunes, J. W. Miklas, J. Liu, R. Aschar-Sobbi, Y. Xiao, B. Zhang, J. Jiang, S. Masse, M. Gagliardi, A. Hsieh, N. Thavandiran, M. A. Laflamme, K. Nanthakumar, G. J. Gross, P. H. Backx, G. Keller and M. Radisic, *Nat. Methods*, 2013, **10**, 781.
39 S. Musah, N. Dimitrakakis, D. M. Camacho, G. M. Church and D. E. Ingber, *Nat. Protoc.*, 2018, **13**, 1662–1685.
40 J. Wang, C. Wang, N. Xu, Z.-F. Liu, D.-W. Pang and Z.-L. Zhang, *Biomaterials*, 2019, **219**, 8.
41 C. Bouffi, K. A. Wikenheiser-Brokamp, P. Chaturvedi, N. Sundaram, G. R. Goddard, M. Wunderlich, N. E. Brown, J. F. Staab, R. Latanich, N. C. Zachos, E. M. Holloway, M. M. Mahe, H. M. Poling, S. Vales, G. W. Fisher, J. R. Spence, J. C. Mulloy, A. M. Zorn, J. M. Wells and M. A. Helmrath, *Nat. Biotechnol.*, 2023, **41**, 824–831.
42 H. J. Kim, H. Li, J. J. Collins and D. E. Ingber, *Proc. Natl. Acad. Sci. U. S. A.*, 2016, **113**, E7-15.
43 B. Wysoczański, M. Świątek and A. Wójcik-Gładysz, *Biomolecules*, 2024, **14**, 1569.
44 K. Ronaldson-Bouchard, D. Teles, K. Yeager, D. N. Tavakol, Y. Zhao, A. Chramiec, S. Tagore, M. Summers, S. Stylianos, M. Tamargo, B. M. Lee, S. P. Halligan, E. H. Abaci, Z. Guo, J. Jackow, A. Pappalardo, J. Shih, R. K. Soni, S. Sonar, C. German, A. M. Christiano, A. Califano, K. K. Hirschi, C. S. Chen, A. Przekwas and G. Vunjak-Novakovic, *Nat. Biomed. Eng.*, 2022, **6**, 351–371.
45 M. Trapecar, C. Communal, J. Velazquez, C. A. Maass, Y.-J. Huang, K. Schneider, C. W. Wright, V. Butty, G. Eng, O. Yilmaz, D. Trumper and L. G. Griffith, *Cell Syst.*, 2020, **10**, 223–239.
46 A. Essaouiba, T. Okitsu, R. Kinoshita, R. Jellali, M. Shinohara, M. Danoy, C. Legallais, Y. Sakai and E. Leclerc, *Biochem. Eng. J.*, 2020, **164**, 107783.
47 V. L. Slaughter, J. W. Rumsey, R. Boone, D. Malik, Y. Cai, N. N. Sriram, C. J. Long, C. W. McAleer, S. Lambert, M. L. Shuler and J. J. Hickman, *Sci. Rep.*, 2021, **11**, 13159.
48 B. Venzac, *Lab Chip*, 2025, **25**, 2129–2147.
49 D. Kumar, R. Nadda and R. Repaka, *Med. Biol. Eng. Comput.*, 2024, **62**, 1925–1957.
50 P. De Saram, N. T. Nguyen, S. Jamali and N. Kashaninejad, *Small Sci.*, 2025, **5**, 2400410.
51 S. Sun, L. Jin, Y. Zheng and J. Zhu, *Nat. Commun.*, 2022, **13**, 5481.
52 Z. M. Deng, F. F. Dai, R. Q. Wang, H. B. Deng, T. L. Yin, Y. X. Cheng and G. T. Chen, *J. Nanobiotechnol.*, 2024, **22**, 455.
53 J. H. Lee, Z. Chen, S. He, J. Zhou, A. Tsai, G. Truskey and K. W. Leong, *Adv. Biol.*, 2021, **5**, e2000428.
54 E. Pan, D. Bogumil, V. Cortessis, S. Yu and J. Nieva, *Front. Oncol.*, 2020, **10**, 591.
55 J. Lee, S. Mehrotra, E. Zare-Eelanjegh, R. O. Rodrigues, A. Akbarinejad, D. Ge, L. Amato, K. Kiaee, Y. Fang, A. Rosenkranz, W. Keung, B. B. Mandal, R. A. Li, T. Zhang, H. Lee, M. R. Dokmeci, Y. S. Zhang, A. Khademhosseini and S. R. Shin, *Small*, 2020, **17**, 2004258.
56 P. Suryavanshi and D. Bodas, *Nanotheranostics*, 2024, **8**, 380–400.
57 Y. Guan, L. Racioppi and S. Gerecht, *Nat. Rev. Mater.*, 2023, **8**, 688–699.
58 C. W. McAleer, C. J. Long, D. Elbrecht, T. Sasserath, L. R. Bridges, J. W. Rumsey, C. Martin, M. Schnepper, Y. Wang, F. Schuler, A. B. Roth, C. Funk, M. L. Shuler and J. J. Hickman, *Sci. Transl. Med.*, 2019, **11**, 12.
59 A. Ugodnikov, H. Persson and C. A. Simmons, *Lab Chip*, 2024, **24**, 3199–3225.
60 L. J. Y. Ong, T. Ching, L. H. Chong, S. Arora, H. Li, M. Hashimoto, R. DasGupta, P. K. Yuen and Y.-C. Toh, *Lab Chip*, 2019, **19**, 2178–2191.
61 A. K. Au, N. Bhattacharjee, L. F. Horowitz, T. C. Chang and A. Folch, *Lab Chip*, 2015, **15**, 1934–1941.
62 K. Corral-Najera, G. Chauhan, S. O. Serna-Saldivar, S. O. Martinez-Chapa and M. M. Aeinehvand, *Microsyst. Nanoeng.*, 2023, **9**, 107.
63 Y. Zhu, K. Mandal, A. L. Hernandez, S. Kawakita, W. Huang, P. Bandaru, S. Ahadian, H.-J. Kim, V. Jucaud, M. R. Dokmeci and A. Khademhosseini, *Curr. Opin. Biomed. Eng.*, 2021, **19**, 100309.
64 F. Pisani, V. Castagnola, L. Simone, F. Loiacono, M. Svelto and F. Benfenati, *Cell Death Dis.*, 2022, **13**, 582.
65 L. Cools, M. K. Dastjerd, A. Smout, V. Merens, Y. Yang, H. Reynaert, N. Messaoudi, V. Smet, M. Kumar, S. Verhulst, C. Verfaillie and L. A. van Grunsven, *Biofabrication*, 2024, **16**, 035032.
66 S. Park, Y. Gwon, S. A. Khan, K. J. Jang and J. Kim, *Biomater. Res.*, 2023, **27**, 67.
67 J. D. Stucki, N. Hobi, A. Galimov, A. O. Stucki, N. Schneider-Daum, C. M. Lehr, H. Huwer, M. Frick, M. Funke-Chambour, T. Geiser and O. T. Guenat, *Sci. Rep.*, 2018, **8**, 14359.
68 V. Kartsogiannis and K. W. Ng, *Mol. Cell. Endocrinol.*, 2004, **228**, 79–102.
69 L. Si, H. Bai, M. Rodas, W. Cao, C. Y. Oh, A. Jiang, R. Moller, D. Hoagland, K. Oishi, S. Horiuchi, S. Uhl, D. Blanco-Melo, R. A. Albrecht, W. C. Liu, T. Jordan, B. E. Nilsson-Payant, I. Golynker, J. Frere, J. Logue, R. Haupt, M. McGrath, S. Weston, T. Zhang, R. Plebani, M. Soong, A. Nurani, S. M. Kim, D. Y. Zhu, K. H. Benam, G. Goyal, S. E. Gilpin, R. Prantil-Baun, S. P. Gygi, R. K. Powers, K. E. Carlson, M. Frieman, B. R. tenOever and D. E. Ingber, *Nat. Biomed. Eng.*, 2021, **5**, 815–829.

70 H. J. Rippon and A. E. Bishop, *Cell Proliferation*, 2004, **37**, 23–34.
71 K. Kim, A. Doi, B. Wen, K. Ng, R. Zhao, P. Cahan, J. Kim, M. J. Aryee, H. Ji, L. I. R. Ehrlich, A. Yabuuchi, A. Takeuchi, K. C. Cunniff, H. Hongguang, S. McKinney-Freeman, O. Naveiras, T. J. Yoon, R. A. Irizarry, N. Jung, J. Seita, J. Hanna, P. Murakami, R. Jaenisch, R. Weissleder, S. H. Orkin, I. L. Weissman, A. P. Feinberg and G. Q. Daley, *Nature*, 2010, **467**, 285–290.
72 S. Yamanaka, *Cell Stem Cell*, 2012, **10**, 678–684.
73 H. E. Young and A. C. Black, *Anat. Rec., Part A*, 2003, **276**, 75–102.
74 P. K. Nguyen, J.-W. Rhee and J. C. Wu, *JAMA Cardiol.*, 2016, **1**, 831.
75 S. Gunti, A. T. K. Hoke, K. P. Vu and N. R. London, Jr., *Cancers*, 2021, **13**, 874.
76 T. Yu, Q. Yang, B. Peng, Z. Gu and D. Zhu, *Angiogenesis*, 2024, **27**, 147–172.
77 G. Fang, Y. C. Chen, H. Lu and D. Jin, *Adv. Funct. Mater.*, 2023, **33**, 2215043.
78 M. S. Yousafzai and J. A. Hammer, *Biosensors*, 2023, **13**, 905.
79 T. Tian, Y. Ho, C. Chen, H. Sun, J. Hui, P. Yang, Y. Ge, T. Liu, J. Yang and H. Mao, *Chin. Chem. Lett.*, 2022, **33**, 3167–3171.
80 E. M. Strohm, N. I. Callaghan, Y. Ding, N. Latifi, N. Rafatian, S. Funakoshi, I. Fernandes, C. J. Reitz, M. Di Paola, A. O. Gramolini, M. Radisic, G. Keller, M. C. Kolios and C. A. Simmons, *ACS Nano*, 2024, **18**, 314–327.
81 M. G. Andrews and A. R. Kriegstein, *Annu. Rev. Neurosci.*, 2022, **45**, 23–39.
82 K. Kretzschmar and H. Clevers, *Dev. Cell*, 2016, **38**, 590–600.
83 G. J. Yoshida, *J. Hematol. Oncol.*, 2020, **13**, 4.
84 J. Liang, X. Li, Y. Dong and B. Zhao, *Cell Transplant*, 2022, **31**, 1–15.
85 J. J. Vandana, C. Manrique, L. A. Lacko and S. Chen, *Cell Stem Cell*, 2023, **30**, 571–591.
86 F. Weeber, S. N. Ooft, K. K. Dijkstra and E. E. Voest, *Cell Chem. Biol.*, 2017, **24**, 1092–1100.
87 V. Veninga and E. E. Voest, *Cancer Cell*, 2021, **39**, 1190–1201.
88 A. Aazmi, D. Zhang, C. Mazzaglia, M. Yu, Z. Wang, H. Yang, Y. Y. S. Huang and L. Ma, *Bioact. Mater.*, 2024, **31**, 475–496.
89 E. Ergir, B. Bachmann, H. Redl, G. Forte and P. Ertl, *Front. Physiol*, 2018, **9**, 1417.
90 S. Liu, S. Kumari, H. He, P. Mishra, B. N. Singh, D. Singh, S. Liu, P. Srivastava and C. Li, *Biosens. Bioelectron*, 2023, **231**, 115285.
91 F. T. Lee-Montiel, S. M. George, A. H. Gough, A. D. Sharma, J. Wu, R. DeBiasio, L. A. Vernetti and D. L. Taylor, *Exp. Biol. Med.*, 2017, **242**, 1617–1632.
92 N. Jiang, G. Ying, Y. Yin, J. Guo, J. Lozada, A. Valdivia Padilla, A. Gomez, B. A. Gomes de Melo, F. Lugo Mestre, M. Gansevoort, M. Palumbo, N. Cala, C. E. Garciamendez-Mijares, G. A. Kim, S. Takayama, M. D. Gerhard-Herman and Y. S. Zhang, *PNAS*, 2024, **121**, e2413684121.
93 A. Ehrlich, S. Tsytkin-Kirschenzweig, K. Ioannidis, M. Ayyash, A. Riu, R. Note, G. Ouedraogo, J. Vanfleteren, M. Cohen and Y. Nahmias, *Lab Chip*, 2018, **18**, 2510–2522.
94 N. Mori, Y. Morimoto and S. Takeuchi, *Biomaterials*, 2017, **116**, 48–56.
95 C. Ding, X. Chen, Q. Kang and X. Yan, *Front. Bioeng. Biotechnol.*, 2020, **8**, 823.
96 S. Jalili-Firoozinezhad, F. S. Gazzaniga, E. L. Calamari, D. M. Camacho, C. W. Fadel, A. Bein, B. Swenor, B. Nestor, M. J. Cronce, A. Tovaglieri, O. Levy, K. E. Gregory, D. T. Breault, J. M. S. Cabral, D. L. Kasper, R. Novak and D. E. Ingber, *Nat. Biomed. Eng.*, 2019, **3**, 520–531.
97 B. Park, J. Park, S. Han, T. Kwon, J. Y. Sung, J. Kim, M. Safarkhani, K.-H. Min, E.-H. Lee, S.-M. Kang and Y. S. Huh, *Mater. Today*, 2025, **84**, 75–94.
98 R. Booth and H. Kim, *Lab Chip*, 2012, **12**, 1784.
99 A. Jain, R. Barrile, A. D. van der Meer, A. Mammoto, T. Mammoto, K. De Ceunynck, O. Aisiku, M. A. Otieno, C. S. Louden, G. A. Hamilton, R. Flaumenhaft and D. E. Ingber, *Clin. Pharmacol. Ther.*, 2017, **103**, 332–340.
100 H. Makkar and G. Sriram, *Lab Chip*, 2025, **25**, 1342–1371.
101 T. Zhang, S. Yang, Y. Ge, L. Yin, Y. Pu, Z. Gu, Z. Chen and G. Liang, *ACS Nano*, 2024, **18**, 31569–31585.
102 D. Huang, T. Liu, J. Liao, S. Maharjan, X. Xie, M. Perez, I. Anaya, S. Wang, A. Tirado Mayer, Z. Kang, W. Kong, V. L. Mainardi, C. E. Garciamendez-Mijares, G. Garcia Martinez, M. Moretti, W. Zhang, Z. Gu, A. M. Ghaemmaghami and Y. S. Zhang, *PNAS*, 2021, **118**, e2016146118.
103 S. I. Ahn, Y. J. Sei, H. J. Park, J. Kim, Y. Ryu, J. J. Choi, H. J. Sung, T. J. MacDonald, A. I. Levey and Y. Kim, *Nat. Commun.*, 2020, **11**, 175.
104 Y. Wang, L. Wang, Y. Zhu and J. Qin, *Lab Chip*, 2018, **18**, 851–860.
105 T. Osaki, V. Sivathanu and R. D. Kamm, *Curr. Opin. Biotechnol.*, 2018, **52**, 116–123.
106 S. Koornneef, F. J. Horne, H. B. Thio, M. Mastrangeli, R. J. Rottier, W. A. Dik and E. D. de Geus, *Environ. Res.*, 2025, **285**, 122289.
107 E. Khanjani, A. Fergola, J. A. López Martínez, S. Nazarnezhad, J. Casals Terre, S. L. Marasso and B. Aghajanloo, *Front. Lab Chip Technol.*, 2025, **4**, 1502127.
108 R. X. Z. Lu and M. Radisic, *Bioact. Mater.*, 2021, **15**, 2801–2819.
109 S. Wang, X. Zhang, C. Ma, S. Yan, D. Inglis and S. Feng, *Biosensors*, 2021, **11**, 405.
110 S. Silva, J. Bicker, A. Falcao and A. Fortuna, *Eur. J. Pharm. Biopharm.*, 2023, **184**, 62–82.
111 J. Kim, J. Kim, Y. Jin and S.-W. Cho, *Biofabrication*, 2023, **15**, 042002.
112 K. T. Kroll, K. A. Homan, S. G. M. Uzel, M. M. Mata, K. J. Wolf, J. E. Rubins and J. A. Lewis, *Biofabrication*, 2024, **16**, 045003.
113 Z. J. Wang, R. Samanipour, K.-i. Koo and K. Kim, *Sens. Mater.*, 2015, **27**, 487–506.
114 O. Y. F. Henry, R. Villenave, M. J. Cronce, W. D. Leineweber, M. A. Benz and D. E. Ingber, *Lab Chip*, 2017, **17**, 2264–2271.

115 U. Ben-David, B. Siranosian, G. Ha, H. Tang, Y. Oren, K. Hinohara, C. A. Strathdee, J. Dempster, N. J. Lyons, R. Burns, A. Nag, G. Kugener, B. Cimini, P. Tsvetkov, Y. E. Maruvka, R. O'Rourke, A. Garrity, A. A. Tubelli, P. Bandopadhayay, A. Tsherniak, F. Vazquez, B. Wong, C. Birger, M. Ghandi, A. R. Thorner, J. A. Bittker, M. Meyerson, G. Getz, R. Beroukhim and T. R. Golub, *Nature*, 2018, **560**, 325.
116 D. H. Elbrecht, C. J. Long and J. J. Hickman, *J. Rare Dis. Res. Treat.*, 2016, **1**, 46–52.
117 M. Buchert, K. Turksen and F.Hollande, *Stem Cell Rev. Rep.*, 2012, **8**, 1030–1034.
118 G. Sriram, M. Alberti, Y. Dancik, B. Wu, R. Wu, Z. Feng, S. Ramasamy, P. L. Bigliardi, M. Bigliardi-Qi and Z. Wang, *Mater. Today*, 2017, **21**, 326–340.
119 P. R. Twentyman and M. Luscombe, *Br. J. Cancer*, 1987, **56**, 279–285.
120 S. Kothari, Q. Chaudry and M. D. Wang, *Proc. IEEE Int. Symp. Biomed. Imaging*, 2009, **2009**, 795–798.
121 N. James, S. Kini, S. Pai, N. Shenoy and S. P. Kabekkodu, *Clin., Cosmet. Invest. Dent.*, 2022, **14**, 87–94.
122 L. Garibyan and N. Avashia, *J. Invest. Dermatol.*, 2013, **133**, 1–4.
123 W. Liu and D. A. Saint, *Anal. Biochem.*, 2002, **302**, 52–59.
124 F. Ye, D. C. Samuels, T. Clark and Y. Guo, *Mitochondrion*, 2014, **17**, 157–163.
125 Z. Wang, M. Gerstein and M. Snyder, *Nat. Rev. Genet.*, 2009, **10**, 57–63.
126 B. Baddal, *Dis.*, 2019, **77**, ftz060.
127 P. Zhao, Q. Yao, P.-J. Zhang, E. The, Y. Zhai, L. Ao, M. J. Jarrett, C. A. Dinarello, D. A. Fullerton and X. Meng, *Sci. Adv.*, 2021, **7**, eabg1694.
128 A. Abdulla, T. Zhang, S. Li, W. Guo, A. R. Warden, Y. Xin, N. Maboyi, J. Lou, H. Xie and X. Ding, *Microsyst. Nanoeng.*, 2022, **8**, 13.
129 J. J. Bass, D. J. Wilkinson, D. Rankin, B. E. Phillips, N. J. Szewczyk, K. Smith and P. J. Atherton, *Scand. J. Med. Sci. Sports*, 2017, **27**, 4–25.
130 P. Peng, C. Liu, Z. Li, Z. Xue, P. Mao, J. Hu, F. Xu, C. Yao and M. You, *TrAC, Trends Anal. Chem.*, 2022, **152**, 116605.
131 K. Im, S. Mareninov, M. F. P. Diaz and W. H. Yong, *Methods Mol. Biol.*, 2019, **1897**, 299–311.
132 T. Guo, J. A. Steen and M. Mann, *Nature*, 2025, **638**, 901–911.
133 S. Kogler, K. S. Kømurcu, C. Olsen, J.-y. Shoji, F. S. Skottvoll, S. Krauss, S. R. Wilson and H. Røberg-Larsen, *TrAC, Trends Anal. Chem.*, 2023, **161**, 116996.
134 M. W. Toepke and D. J. Beebe, *Lab Chip*, 2006, **6**, 1484–1486.
135 J. D. Wang, N. J. Douville, S. Takayama and M. ElSayed, *Ann. Biomed. Eng.*, 2012, **40**, 1862–1873.
136 F. Zheng, F. Fu, Y. Cheng, C. Wang, Y. Zhao and Z. Gu, *Small*, 2016, **12**, 2253–2282.
137 K. Ronaldson-Bouchard and G. Vunjak-Novakovic, *Cell Stem Cell*, 2018, **22**, 310–324.
138 A. Bhusal, E. Dogan, H.-A. Nguyen, O. Labutina, D. Nieto, A. Khademhosseini and A. K. Miri, *Biofabrication*, 2021, **14**, 014103.
139 A. P. Kuo, N. Bhattacharjee, Y. S. Lee, K. Castro, Y. T. Kim and A. Folch, *Adv. Mater. Technol.*, 2019, **4**, 1800395.
140 D. Syrlybayev, B. Zharylkassyn, A. Seisekulova, M. Akhmetov, A. Perveen and D. Talamona, *Polymers*, 2021, **13**, 1587.
141 L. Xu, H. Ding, S. Wu, N. Xiong, Y. Hong, W. Zhu, X. Chen, X. Han, M. Tao, Y. Wang, D. Wang, M. Xu, D. Huo, Z. Gu and Y. Liu, *ACS Nano*, 2024, **18**, 26201–26214.
142 F. Sima, K. Sugioka, R. M. Vázquez, R. Osellame, L. Kelemen and P. Ormos, *Nanophotonics*, 2018, **7**, 613–634.
143 M. J. C. Modarelli, D. M. Kot-Thompson and K. Hoshino, *Lab Chip*, 2025, **25**, 127–142.
144 R. Paoli, D. Di Giuseppe, M. Badiola-Mateos, E. Martinelli, M. J. Lopez-Martinez and J. Samitier, *Sensors*, 2021, **21**, 12382.
145 H. R. Caires, Ó. Castillo-Fernández, N. Sima, M. V. Magalhães, A. Benavent-Claró, N. Masó-Castro, W. Roobsoong, C. Fernandez-Becerra, A. Hernández-Machado, H. A. Del Portillo and C. C. Barrias, *Small Methods*, 2025, **9**, e00652.
146 D. B. Kolesky, K. A. Homan, M. A. Skylar-Scott and J. A. Lewis, *Proc. Natl. Acad Sci. U. S. A.*, 2016, **113**, 3179–3184.
147 S. M. Montgomery, F. Demoly, K. Zhou and H. J. Qi, *Adv. Funct. Mater.*, 2023, **33**, 2213252.
148 S. O'Halloran, A. Pandit, A. Heise and A. Kellett, *Adv. Sci.*, 2023, **10**, e2204072.
149 H. Fu, H. Xu, Y. Liu, Z. Yang, S. Kormakov, D. Wu and J. Sun, *ES Mater. Manuf.*, 2020, **8**, 3–23.
150 Y. K. Hsieh, S. C. Chen, W. L. Huang, K. P. Hsu, K. A. V. Gorday, T. Wang and J. Wang, *Polymers*, 2017, **9**, 242.
151 N. Chen, H. N. Li, J. Wu, Z. Li, L. Li, G. Liu and N. He, *Int. J. Mach. Tool Manu.*, 2021, **160**, 103670.
152 N. Ullah, M. Rehan, M. U. Farooq, H. Li, W. S. Yip and S. S. To, *Int. J. Adv. Manuf. Technol.*, 2025, **137**, 4309–4351.
153 J. A. Rogers and R. G. Nuzzo, *Mater. Today*, 2005, **8**, 50–56.
154 M. Sun, J. Zhang, T. Xuanyuan, X. Liu and W. Liu, *ACS Appl. Mater. Interfaces*, 2024, **16**, 20132–20142.
155 G. Csucs, R. Michel, J. W. Lussi, M. Textor and G. Danuser, *Biomaterials*, 2003, **24**, 1713–1720.
156 J. P. Urbanski, W. Thies, C. Rhodes, S. Amarasinghe and T. Thorsen, *Lab Chip*, 2006, **6**, 96–104.
157 I. Miranda, A. Souza, P. Sousa, J. Ribeiro, E. M. S. Castanheira, R. Lima and G. Minas, *J. Funct. Biomater.*, 2021, **13**, 2.
158 S. Seo, S. Y. Nah, K. Lee, N. Choi and H. N. Kim, *Adv. Funct. Mater.*, 2021, **32**, 2106860.
159 A. W. L. Liew and Y. Zhang, *Int. J. Bioprint.*, 2017, **3**, 3–17.
160 B. F. L. Lai, L. D. Huyer, R. X. Z. Lu, S. Drecun, M. Radisic and B. Zhang, *Adv. Funct. Mater.*, 2017, **27**, 17003524.
161 L. A. Milton, M. S. Viglione, L. J. Y. Ong, G. P. Nordin and Y. C. Toh, *Lab Chip*, 2023, **23**, 3537–3560.
162 M. Yang, L. Chu, Y. Zhuang, C. Qi, S. Meng, Z. Liu and T. Kong, *Adv. Funct. Mater.*, 2024, **34**, 2316456.
163 A. Fritschen, A. K. Bell, I. Königstein, L. Stühn, R. W. Stark and A. Blaeser, *Biomater. Sci.*, 2022, **10**, 1981–1994.

164 A. Jonsson, A. Toppi and M. Dufva, *HardwareX*, 2020, **8**, e00115.
165 S. A. Skoog, P. L. Goering and R. J. Narayan, *J. Mater. Sci.: Mater. Med.*, 2014, **25**, 845–856.
166 A.-I. Bunea, N. del Castillo Iniesta, A. Droumpali, A. E. Wetzel, E. Engay and R. Taboryski, *Micro*, 2021, **1**, 164–180.
167 J. F. Xing, M. L. Zheng and X. M. Duan, *Chem. Soc. Rev*, 2015, **44**, 5031–5039.
168 B. J. Haspels, F. Bakker, L. J. A. M. Beckers, R. Kanaar, K. C. Kriege, S. M. Valster, R. C. M. Vulders and M. M. P. Kuijten, *Adv. Mater. Technol.*, 2025, **10**, 2401450.
169 R. Qin, M. Hu, N. Zhang, Z. Guo, Z. Yan, J. Li, J. Liu, G. Shan and J. Yang, *Adv. Electron. Mater.*, 2019, **5**, 1900365.
170 J. Huft, D. J. Da Costa, D. Walker and C. L. Hansen, *Lab Chip*, 2010, **10**, 2358–2365.
171 H. Gu, C. Wei, L. Li, Q. Han, R. Setchi, M. Ryan and Q. Li, *Int. J. Heat Mass Transfer*, 2020, **151**, 119458.
172 E. Creighton, A. Honegger, A. Tulsian and D. Mukhopadhyay, *Int. J. Mach. Tools Manuf.*, 2010, **50**, 386–393.
173 U. M. N. Cao, Y. Zhang, J. Chen, D. Sayson, S. Pillai and S. D. Tran, *Int. J. Mol. Sci.*, 2023, **24**, 3232.
174 T. C. Cameron, A. Randhawa, S. M. Grist, T. Bennet, J. Hua, L. G. Alde, T. M. Caffrey, C. L. Wellington and K. C. Cheung, *Micromachines*, 2022, **13**, 1573.
175 H. Goodarzi Hosseinabadi, E. Dogan, A. K. Miri and L. Ionov, *ACS Biomater. Sci. Eng.*, 2022, **8**, 1381–1395.
176 F. Kotz, M. Mader, N. Dellen, P. Risch, A. Kick, D. Helmer and B. E. Rapp, *Micromachines*, 2020, **11**, 873.
177 H. J. McLennan, A. J. Blanch, S. J. Wallace, L. J. Ritter, S. L. Heinrich, D. K. Gardner, K. R. Dunning, M. J. Gauvin, A. K. Love and J. G. Thompson, *Sci. Rep.*, 2023, **13**, 562.
178 U. N. Lee, X. Su, D. J. Guckenberger, A. M. Dostie, T. Zhang, E. Berthier and A. B. Theberge, *Lab Chip*, 2018, **18**, 496–504.
179 X. Li, R. Tang, D. Li, F. Li, L. Chen, D. Zhu, G. Feng, K. Zhang and B. Han, *Polymers*, 2024, **16**, 2361.
180 M. C. Allen, S. Lookmire and E. Avci, *Micromachines*, 2024, **15**, 905.
181 J. Kajtez, S. Buchmann, S. Vasudevan, M. Birtele, S. Rocchetti, C. J. Pless, A. Heiskanen, R. A. Barker, A. Martinez-Serrano, M. Parmar, J. U. Lind and J. Emneus, *Adv. Sci.*, 2020, **7**, 2001150.
182 B. Lee, S. Kim, J. Ko, S.-R. Lee, Y. Kim, S. Park, J. Kim, S. Hyung, H.-Y. Kim and N. L. Jeon, *NPG Asia Mater.*, 2022, **14**, 6.
183 Z. Luo, H. Zhang, R. Chen, H. Li, F. Cheng, L. Zhang, J. Liu, T. Kong, Y. Zhang and H. Wang, *Microsyst. Nanoeng.*, 2023, **9**, 103.
184 M. P. Wolf, G. B. Salieb-Beugelaar and P. Hunziker, *Prog. Polym. Sci.*, 2018, **83**, 97–134.
185 S. Aralekallu, R. Boddula and V. Singh, *Mater. Des.*, 2023, **225**, 111517.
186 A. Shakeri, S. Khan, N. A. Jarad and T. F. Didar, *Materials*, 2022, **15**, 6478.
187 Z. Wei, M. Lei, Y. Wang, Y. Xie, X. Xie, D. Lan, Y. Jia, J. Liu, Y. Ma, B. Cheng, S. Gerecht and F. Xu, *Nat. Commun.*, 2023, **14**, 8307.
188 E. W. K. Young and D. J. Beebe, *Chem. Soc. Rev.*, 2010, **39**, 1036–1048.
189 V. Mancini and V. Pensabene, *Bioengineering*, 2019, **6**, 103.
190 A. Marsano, C. Conficconi, M. Lemme, P. Occhetta, E. Gaudiello, E. Votta, G. Cerino, A. Redaelli and M. Rasponi, *Lab Chip*, 2016, **16**, 599–610.
191 S. Rismani Yazdi, A. Shadmani, S. C. Bürgel, P. M. Misun, A. Hierlemann and O. Frey, *Lab Chip*, 2015, **15**, 4138–4147.
192 H. Lee, S. Chae, J. Y. Kim, W. Han, J. Kim, Y. Choi and D.-W. Cho, *Biofabrication*, 2019, **11**, 025001.
193 Y. Roye, R. Bhattacharya, X. Mou, Y. Zhou, M. A. Burt and S. Musah, *Micromachines*, 2021, **12**, 967.
194 X. Mou, J. Shah, Y. Roye, C. Du and S. Musah, *Sci. Adv.*, 2024, **10**, eadn2689.
195 Y. Guo, R. Luo, Y. Wang, P. Deng, T. Song, M. Zhang, P. Wang, X. Zhang, K. Cui, T. Tao, Z. Li, W. Chen, Y. Zheng and J. Qin, *Sci. Bull.*, 2021, **66**, 783–793.
196 M. S. Jeon, Y. Y. Choi, S. J. Mo, J. H. Ha, Y. S. Lee, H. U. Lee, S. D. Park, J.-J. Shim, J.-L. Lee and B. G. Chung, *Nano Convergence*, 2022, **9**, 8.
197 Y. Jang, H. Kim and J. Oh, *Small*, 2024, **20**, 2404842.
198 O. Tricinci, D. De Pasquale, A. Marino, M. Battaglini, C. Pucci and G. Ciofani, *Adv. Mater. Technol.*, 2020, **5**, 2000540.
199 A. Cordiale, D. Stanco, R. Visone, B. Stadlinger, P. Pagella, M. Rasponi and T. A. Mitsiadis, *Adv. Healthcare Mater.*, 2025, e02080.
200 H. Makkar, Y. Zhou, K. S. Tan, C. T. Lim and G. Sriram, *Adv. Healthcare Mater.*, 2023, **12**, e2202376.
201 G. Muniraj, R. H. S. Tan, Y. Dai, R. Wu, M. Alberti and G. Sriram, *Adv. Healthcare Mater.*, 2023, **12**, 2301472.
202 J. Wu, B. Zhang, X. Liu, W. Gu, F. Xu, J. Wang, Q. Liu, R. Wang, Y. Hu, J. Liu, X. Ji, H. Lv, X. Li, L. Peng, X. Li, Y. Zhang and S. Wang, *Adv. Mater.*, 2024, **36**, 2408485.
203 I. Risueño, L. Valencia, J. L. Jorcano and D. Velasco, *APL Bioeng.*, 2021, **5**, 030901.
204 H. M. Jeon, K. Kim, K. C. Choi and G. Y. Sung, *J. Ind. Eng. Chem.*, 2020, **82**, 71–80.
205 K. Hirose, A. Y. Payumo, S. Cutie, A. Hoang, H. Zhang, R. Guyot, D. Lunn, R. B. Bigley, H. Yu, J. Wang, M. Smith, E. Gillett, S. E. Muroy, T. Schmid, E. Wilson, K. A. Field, D. M. Reeder, M. Maden, M. M. Yartsev, M. J. Wolfgang, F. Grützner, T. S. Scanlan, L. I. Szweda, R. Buffenstein, G. Hu, F. Flamant, J. E. Olgin and G. N. Huang, *Science*, 2019, **364**, 184–188.
206 C. A. Lawson, F. Zaccardi, I. Squire, S. Ling, M. J. Davies, C. S. P. Lam, M. A. Mamas, K. Khunti and U. T. Kadam, *Lancet Public Health*, 2019, **4**, e406–e420.
207 A. Grosberg, P. W. Alford, M. L. McCain and K. K. Parker, *Lab Chip*, 2011, **11**, 4165–4173.
208 Y. Chen, H. N. Chan, S. A. Michael, Y. Shen, Y. Chen, Q. Tian, L. Huang and H. Wu, *Lab Chip*, 2017, **17**, 653–662.
209 F. Fu, L. Shang, Z. Chen, Y. Yu and Y. Zhao, *Sci. Robot.*, 2018, **3**, eaar8580.
210 H. Liu, O. A. Bolonduro, N. Hu, J. Ju, A. A. Rao, B. M. Duffy, Z. Huang, L. D. Black and B. P. Timko, *Nano Lett.*, 2020, **20**, 2585–2593.

211 K. Suresh and L. A. Shimoda, *Compr. Physiol.*, 2016, **6**, 897–943.
212 D. Huh, D. C. Leslie, B. D. Matthews, J. P. Fraser, S. Jurek, G. A. Hamilton, K. S. Thorneloe, M. A. McAlexander and D. E. Ingber, *Sci. Transl. Med.*, 2012, **4**, 159ra147.
213 H. J. Kim, D. Huh, G. Hamilton and D. E. Ingber, *Lab Chip*, 2012, **12**, 2165.
214 M. Humayun, C.-W. Chow and E. W. K. Young, *Lab Chip*, 2018, **18**, 1298–1309.
215 K. H. Benam, R. Villenave, C. Lucchesi, A. Varone, C. Hubeau, H.-H. Lee, S. E. Alves, M. Salmon, T. C. Ferrante, J. C. Weaver, A. Bahinski, G. A. Hamilton and D. E. Ingber, *Nat. Methods*, 2015, **13**, 151–157.
216 Z. Yang, X. Liu, E. M. Cribbin, A. M. Kim, J. J. Li and K. T. Yong, *Biomicrofluidics*, 2022, **16**, 061502.
217 S. Mi, X. Yi, Z. Du, Y. Xu and W. Sun, *Biofabrication*, 2018, **10**, 025010.
218 Y. B. Zheng, L. D. Ma, J. L. Wu, Y. M. Wang, X. S. Meng, P. Hu, Q. L. Liang, Y. Y. Xie and G. A. Luo, *Talanta*, 2022, **241**, 123262.
219 K.-J. Jang, M. A. Otieno, J. Ronxhi, H.-K. Lim, L. Ewart, K. R. Kodella, D. B. Petropolis, G. Kulkarni, J. E. Rubins, D. Conegliano, J. Nawroth, D. Simic, W. Lam, M. Singer, E. Barale, B. Singh, M. Sonee, A. J. Streeter, C. Manthey, B. Jones, A. Srivastava, L. C. Andersson, D. Williams, H. Park, R. Barrile, J. Sliz, A. Herland, S. Haney, K. Karalis, D. E. Ingber and G. A. Hamilton, *Sci. Transl. Med.*, 2019, **11**, eaax5516.
220 S. Frojdenfal and A. Zuchowska, *Biosensors*, 2024, **14**, 435.
221 M. S. Balzer, T. Rohacs and K. Susztak, *Annu. Rev. Physiol.*, 2022, **84**, 507–531.
222 M. Gust and N. Ferrell, *Sensors*, 2022, **22**, 6889.
223 K. A. Homan, D. B. Kolesky, M. A. Skylar-Scott, J. Herrmann, H. Obuobi, A. Moisan and J. A. Lewis, *Sci. Rep.*, 2016, **6**, 34845.
224 R. Kim and J. H. Sung, *Adv. Healthcare Mater.*, 2024, **13**, 2302777.
225 A. Valiei, J. Aminian-Dehkordi and M. R. K. Mofrad, *Bioeng.*, 2023, **7**, 011502.
226 S. Taavitsainen, K. Juuti-Uusitalo, K. Kurppa, K. Lindfors, P. Kallio and M. Kellomäki, *Front. Lab Chip Technol.*, 2024, **2**, 1337945.
227 R. Moerkens, J. Mooiweer, A. D. Ramírez-Sánchez, R. Oelen, L. Franke, C. Wijmenga, R. J. Barrett, I. H. Jonkers and S. Withoff, *Cell Rep.*, 2024, **43**, 114247.
228 M. A. Mofazzal Jahromi, A. Abdoli, M. Rahmanian, H. Bardania, M. Bayandori, S. M. Moosavi Basri, A. Kalbasi, A. R. Aref, M. Karimi and M. R. Hamblin, *Mol. Neurobiol.*, 2019, **56**, 8489–8512.
229 B. N. Johnson, K. Z. Lancaster, I. B. Hogue, F. Meng, Y. L. Kong, L. W. Enquist and M. C. McAlpine, *Lab Chip*, 2015, **16**, 1393–1400.
230 S. Amartumur, H. Nguyen, T. Huynh, T. S. Kim, R. S. Woo, E. Oh, K. K. Kim, L. P. Lee and C. Heo, *Nat. Commun.*, 2024, **15**, 2219.
231 J. Park, B. K. Lee, G. S. Jeong, J. K. Hyun, C. J. Lee and S. H. Lee, *Lab Chip*, 2015, **15**, 141–150.
232 N. Vysokov, S. B. McMahon and R. Raouf, *Sci. Rep.*, 2019, **9**, 12915.
233 Y. Shin, S. H. Choi, E. Kim, E. Bylykbashi, J. A. Kim, S. Chung, D. Y. Kim, R. D. Kamm and R. E. Tanzi, *Adv. Sci.*, 2019, **6**, 1900962.
234 T. Baltazar, J. Merola, C. Catarino, C. B. Xie, N. C. Kirkiles-Smith, V. Lee, S. Hotta, G. Dai, X. Xu, F. C. Ferreira, W. M. Saltzman, J. S. Pober and P. Karande, *Tissue Eng., Part A*, 2020, **26**, 227–238.
235 H. J. Song, H. Y. Lim, W. Chun, K. C. Choi, T.-y. Lee, J. H. Sung and G. Y. Sung, *J. Ind. Eng. Chem.*, 2018, **60**, 355–359.
236 B. S. Kim, G. Gao, J. Y. Kim and D. W. Cho, *Adv. Healthcare Mater.*, 2019, **8**, e1801019.
237 M. Wufuer, G. Lee, W. Hur, B. Jeon, B. J. Kim, T. H. Choi and S. Lee, *Sci. Rep.*, 2016, **6**, 37471.
238 J. Zhang, Z. Chen, Y. Zhang, X. Wang, J. Ouyang, J. Zhu, Y. Yan, X. Sun, F. Wang, X. Li, H. Ye, S. Sun, Q. Yu, J. Sun, J. Ge, Q. Li, Q. Han, Y. Pu and Z. Gu, *Lab Chip*, 2021, **21**, 3804–3818.
239 H. Y. Lim, J. Kim, H. J. Song, K. Kim, K. C. Choi, S. Park and G. Y. Sung, *J. Ind. Eng. Chem.*, 2018, **68**, 238–245.
240 S. Rhee, C. Xia, A. Chandra, M. Hamon, G. Lee, C. Yang, Z. Guo and B. Sun, *Bioengineering*, 2024, **11**, 1055.
241 C. M. Franca, G. S. Balbinot, D. Cunha, V. P. A. Saboia, J. Ferracane and L. E. Bertassoni, *Acta Biomater.*, 2022, **150**, 58–66.
242 I. Dasgupta, D. P. Rangineni, H. Abdelsaid, Y. Ma and A. Bhushan, *Bioengineering*, 2024, **11**, 476.
243 H. Zhang, L. Li, S. Wang, X. Sun, C. Luo and B. Hou, *J. Dent.*, 2024, **146**, 105028.
244 M. Jang and H. N. Kim, *Biochip J.*, 2023, **17**, 133–146.
245 N. Picollet-D'hahan, A. Zuchowska, I. Lemeunier and S. Le Gac, *Trends Biotechnol.*, 2021, **39**, 788–810.
246 F. Yin, X. Zhang, L. Wang, Y. Wang, Y. Zhu, Z. Li, T. Tao, W. Chen, H. Yu and J. Qin, *Lab Chip*, 2021, **21**, 571–581.
247 S. Bauer, C. Wennberg Huldt, K. P. Kanebratt, I. Durieux, D. Gunne, S. Andersson, L. Ewart, W. G. Haynes, I. Maschmeyer, A. Winter, C. Ämmälä, U. Marx and T. B. Andersson, *Sci. Rep.*, 2017, **7**, 14620.
248 H. R. Lee and J. H. Sung, *Biotechnol. Bioeng.*, 2022, **119**, 2590–2601.
249 D. Huh, Y.-s. Torisawa, G. A. Hamilton, H. J. Kim and D. E. Ingber, *Lab Chip*, 2012, **12**, 2156.
250 J. Aleman and A. Skardal, *Biotechnol. Bioeng.*, 2018, **116**, 936–944.
251 H. Xu, Z. Li, Y. Yu, S. Sizdahkhani, W. S. Ho, F. Yin, L. Wang, G. Zhu, M. Zhang, L. Jiang, Z. Zhuang and J. Qin, *Sci. Rep.*, 2016, **6**, 36670.
252 H.-r. Moon, A. Ozcelikkale, Y. Yang, B. D. Elzey, S. F. Konieczny and B. Han, *Lab Chip*, 2020, **20**, 3720–3732.
253 J. Picot, P. A. Ndour, S. D. Lefevre, W. El Nemer, H. Tawfik, J. Galimand, L. Da Costa, J. A. Ribeil, M. de Montalembert, V. Brousse, B. Le Pioufle, P. Buffet, C. Le Van Kim and O. Français, *Am. J. Hematol.*, 2015, **90**, 339–345.
254 L. G. Rigat-Brugarolas, A. Elizalde-Torrent, M. Bernabeu, M. De Niz, L. Martin-Jaular, C. Fernandez-Becerra, A. Homs-

Corbera, J. Samitier and H. A. del Portillo, *Lab Chip*, 2014, **14**, 1715–1724.
255 T. Shen, S. Han, W. He, W. Yang, X. Tang, X. Zhao, X. Liu, Z. Shao, L. Cheng, Y. Zhao and J. Fan, *Adv. Sci.*, 2025, **12**, e2406077.
256 D. Bennet, Z. Estlack, T. Reid and J. Kim, *Lab Chip*, 2018, **18**, 1539–1551.
257 Y. Deng, L. Li, J. Xu, Y. Yao, J. Ding, L. Wang, C. Luo, W. Yang and L. Li, *Biomater. Sci.*, 2024, **12**, 5239–5252.
258 L. Businaro, A. De Ninno, G. Schiavoni, V. Lucarini, G. Ciasca, A. Gerardino, F. Belardelli, L. Gabriele and F. Mattei, *Lab Chip*, 2013, **13**, 229–239.
259 Y. Hu, J. Xing, H. Zhang, X. Pang, Y. Zhai, H. Cheng, D. Xu, M. Liao, Y. Qi, D. Wu, B. Zhang, L. Cheng, B. Chu, C. Zhang, Y. Zhao and R. Chai, *Adv. Mater.*, 2024, **36**, 2309002.
260 L. Si, H. Bai, M. Rodas, W. Cao, C. Y. Oh, A. Jiang, R. Moller, D. Hoagland, K. Oishi, S. Horiuchi, S. Uhl, D. Blanco-Melo, R. A. Albrecht, W.-C. Liu, T. Jordan, B. E. Nilsson-Payant, I. Golynker, J. Frere, J. Logue, R. Haupt, M. McGrath, S. Weston, T. Zhang, R. Plebani, M. Soong, A. Nurani, S. M. Kim, D. Y. Zhu, K. H. Benam, G. Goyal, S. E. Gilpin, R. Prantil-Baun, S. P. Gygi, R. K. Powers, K. E. Carlson, M. Frieman, B. R. TenOever and D. E. Ingber, *Nat. Biomed. Eng.*, 2021, **5**, 815–829.
261 R. Prantil-Baun, R. Novak, D. Das, M. R. Somayaji, A. Przekwas and D. E. Ingber, *Annu. Rev. Pharmacol. Toxicol.*, 2018, **58**, 37–64.
262 P. Fathi, G. Holland, D. Pan and M. B. Esch, *ACS Appl. Bio mater.*, 2020, **3**, 6697–6707.
263 G. Lacroix, W. Koch, D. Ritter, A. C. Gutleb, S. T. Larsen, T. Loret, F. Zanetti, S. Constant, S. Chortarea, B. Rothen-Rutishauser, P. S. Hiemstra, E. Frejafon, P. Hubert, L. Gribaldo, P. Kearns, J. M. Aublant, S. Diabate, C. Weiss, A. de Groot and I. Kooter, *Appl. In Vitro Toxicol.*, 2018, **4**, 91–106.
264 J. Zhang, J. Zhou, Y. Wang, Y. Yang, T. Yue and C. Chang, *Med. Nov. Technol. Devices*, 2026, **29**, 100415.
265 K. Fibben, E. K. Williams, J. D. Roback, W. A. Lam and D. N. Alter, *Lab Chip*, 2025, **25**, 2566–2577.
266 L. Zhou, J. Huang, C. Li, Q. Gu, G. Li, Z. A. Li, J. Xu, J. Zhou and R. S. Tuan, *Med*, 2025, **6**, 100667.
267 X. Liu, M. Gao, B. Li, R. Liu, Z. Chong, Z. Gu and K. Zhou, *Adv. Mater.*, 2024, **36**, 2310797.
268 A. S. Morais, M. Mendes, M. A. Cordeiro, J. J. Sousa, A. C. Pais, S. M. Mihaila and C. Vitorino, *Pharmaceutics*, 2024, **16**, 615.
269 X. Liu, H. Gu, H. Ding, X. Du, Z. He, L. Sun, J. Liao, P. Xiao and Z. Gu, *Small*, 2019, **15**, 1902360.
270 X. Liu, H. Gu, M. Wang, X. Du, B. Gao, A. Elbaz, L. Sun, J. Liao, P. Xiao and G. Zhongze, *Adv. Mater.*, 2018, **30**, e1800103.
271 R. Liu, Y. Zhou, M. Gao, W. Shi, Y. Zhang, X. Liu and Z. Gu, *Adv. Funct. Mater.*, 2024, **35**, 2416593.
272 Z. Junning, D. Haibo, L. Xiaojiang, G. Hongcheng, W. Mengxiao, L. Xiaoran, L. Shengnan, L. Sen and D. Xin, *Zhongze, Small*, 2021, **17**, e2101048.
273 C. Han, X. Luo, D. Zou, J. Li, K. Zhang, P. Yang and N. Huang, *Biomater. Sci.*, 2019, **7**, 2686–2701.
274 X. Liu, H. Gu, H. Ding, X. Du, M. Wei, Q. Chen and G. Zhongze, *Adv. Sci.*, 2020, **7**, 2000878.
275 X. Liu, B. Li, Z. Gu and K. Zhou, *Small*, 2023, **19**, 2207640.
276 A. Herland, B. M. Maoz, D. Das, M. R. Somayaji, R. Prantil-Baun, R. Novak, M. Cronce, T. Huffstater, S. S. F. Jeanty, M. Ingram, A. Chalkiadaki, D. Benson Chou, S. Marquez, A. Delahanty, S. Jalili-Firoozinezhad, Y. Milton, A. Sontheimer-Phelps, B. Swenor, O. Levy, K. K. Parker, A. Przekwas and D. E. Ingber, *Nat. Biomed. Eng.*, 2020, **4**, 421–436.
277 S. Hazra, S. Palit, T. Russomano, G. Ghosh and P. Sannigrahi, *Front. Space Technol.*, 2026, **6**, 1725575.
278 S. D. Verma, E. Passerat de la Chapelle, S. Malkani, C. M. Juran, V. Boyko, S. V. Costes and E. Cekanaviciute, *Front. Immunol.*, 2022, **13**, 864923.
279 Y. Fan and O. Pedersen, *Nat. Rev. Endocrinol.*, 2021, **19**, 55–71.
280 B. Cariou, C. D. Byrne, R. Loomba and A. J. Sanyal, *Diabetes Obes. Metab.*, 2021, **23**, 1069–1083.
281 J. Aleman, T. Kilic, L. S. Mille, S. R. Shin and Y. S. Zhang, *Nat. Protoc.*, 2021, **16**, 2564–2593.
282 B. Servais, N. Mahmoudi, V. Gautam, W. Tong, M. R. Ibbotson, D. R. Nisbet and D. Collins, *Nat. Rev. Bioeng.*, 2024, **2**, 691–709.
283 C. M. Didier, A. Kundu and S. Rajaraman, *J. Microelectromech. Syst.*, 2021, **30**, 853–863.
284 O. Y. F. Henry, R. Villenave, M. J. Cronce, W. D. Leineweber, M. A. Benz and D. E. Ingber, *Lab Chip*, 2017, **17**, 2264–2271.
285 Q. Li, Z. Chen, Y. Zhang, S. Ding, H. Ding, L. Wang, Z. Xie, Y. Fu, M. Wei, S. Liu, J. Chen, X. Wang and Z. Gu, *Nat. Commun.*, 2023, **14**, 7369.
286 W. Gao, C. Wang, Q. Li, X. Zhang, J. Yuan, D. Li, Y. Sun, Z. Chen and Z. Gu, *Front. Bioeng. Biotechnol.*, 2022, **10**, 985692.
287 S. Deng, C. Li, J. Cao, Z. Cui, J. Du, Z. Fu, H. Yang and P. Chen, *Theranostics*, 2023, **13**, 4526–4558.